Universitat de Barcelona

HWCVD Technology Development Addressed to the High Rate Deposition of μc-Si:H

Oriol Nos Aguilà

DEPARTAMENT DE FÍSICA APLICADA I ÒPTICA

Av. Diagonal, 645, 08028 Barcelona

HWCVD Technology Development Addressed to the High Rate Deposition of μc-Si:H

Oriol Nos Aguilà

Memòria presentada per optar al grau de Doctor

Barcelona, Setembre de 2012

DEPARTAMENT DE FÍSICA APLICADA I ÒPTICA

Av. Diagonal, 645, 08028 Barcelona

HWCVD Technology Development Addressed to the High Rate Deposition of μc-Si:H

Oriol Nos Aguilà

Directors: Paolo Antonio Frigeri; Joan Bertomeu i Balagueró
Programa de doctorat: Física

Memòria presentada per optar al grau de Doctor

Barcelona, Setembre de 2012

This work has been supported by the Ministerio de Ciencia e Innovación, the Ministerio de Economía y Competitividad and the European Regional Development Fund through the projects CLASICO (ENE2007-67742-C04-03), AMIC (ENE2010-21384-C04-03), MICROSIL08 (PSE-120000-2008-1) and INNDISOL (IPT-420000-2010-6).

Als meus pares,
Jaume i Montserrat

Resum en Català

El primer bloc d'aquesta tesi es centra en l'estudi del procés de degradació dels filaments de tungstè catalítics en el camp del dipòsit de silici amb la tècnica de dipòsit químic en fase vapor assistida per filament calent (HWCVD). També es tractarà el desenvolupament de solucions tecnològiques dirigides a la protecció filaments. El segon bloc tracta sobre l'escalat de la tècnica HWCVD cap a gran àrea i sobre l'existència d'una llei d'escala que permeti el dipòsit de silici microcristal·lí (μc-Si:H) a altes velocitats, tot preservant la qualitat del material. En primer lloc s'exposarà una breu introducció sobre cèl·lules solars micromorfes, les limitacions actuals, relacionades amb el dipòsit de μc-Si:H, per a fer la producció de mòduls micromorfs econòmicament rendible i la potencialitat de la tècnica HWCVD per superar aquestes limitacions. A continuació, es mostra experimentalment que el decaïment del rendiment catalític dels filaments s'inicia després d'una primera etapa de dissolució d'àtoms de Si en el filament i que la durada d'aquesta primera etapa és només d'unes poques hores. Mitjançant l'ús d'un model de difusió, es mostrarà que, en la majoria de les situacions pràctiques, la durada d'aquesta etapa de dissolució d'àtoms de Si és independent del radi de filament triat. S'utilitzarà un model elèctric per a comprovar l'estat del procés de degradació del filaments en temps real, simplement per mitjà del seguiment del pendent de la resistència elèctrica de filaments. Es mostrarà que el final de l'etapa de dissolució de àtoms de Si correspon a un canvi brusc del pendent de la resistència elèctrica de filaments. Presentarem un dispositiu de protecció (anomenat "*cavitat d'auto-neteja*") desenvolupat i fabricat al nostre laboratori, que ofereix una protecció eficaç per als extrems freds dels filaments contra la formació de siliciurs. Mitjançant la implementació d'aquests dispositius de protecció, la formació de siliciurs als extrems freds del filament es redueix a un ritme menor que l'observat a la porció central

del filament. Mostrarem els resultats de les proves de validació d'un mecanisme automàtic de reemplaçament del filaments, desenvolupat per nosaltres, que permet substituir una porció usada d'un filament per una altra porció neta de filament, sense necessitat de trencar el buit. Aquest mecanisme de reemplaçament dels filaments inclou un mecanisme d'ajust de la tensió que permet mantenir tensa, en totes les situacions de funcionament, la porció de filament que vindrà utilitzada per al dipòsit de la pel·lícula. Es mostrarà que aquest mecanisme de reemplaçament del filaments, en combinació amb l'ús de dispositius de protecció "cavitat d'auto-neteja", garanteix la repetibilitat i l'estabilitat d'un procés HWCVD per al dipòsit de materials basats en silici. No tenim constància que mai abans s'hagi notificat la construcció d'un aparell de HWCVD similar. Tot seguit, demostrarem l'existència d'un "*límit de àrea gran*" que permet estudiar, mitjançant una xarxa de filaments catalítics relativament petita, el comportament de qualsevol reactor de mida arbitràriament més gran. Si la configuració de filaments es tria convenientment, veurem que es pot aconseguir una uniformitat de gruix de les pel·lícules dipositades excel·lent ($< \pm 2.5\%$). També s'exposarà un model de difusió de radicals que permet predir amb gran exactitud, els perfils de gruix de les pel·lícules dipositades.

Mostrarem la possible existència d'una llei d'escala que podria permetre l'augment del ritme de dipòsit, r_d, de capes μc-Si: H, utilitzant silà i hidrogen com a gasos precursors, preservant alhora la qualitat del material dipositat. Aquesta llei d'escala només és vàlida si el producte $p \cdot d_{f-s}$ (pressió de procés per la distància del filament al substrat) i la relació entre les pressions parcials d'hidrogen i silà, p_{SiH_4}/p_{H_2} es mantenen constants. Si aquestes dues condicions es compleixen, la relació esperada entre els ritmes de dipòsit obtinguts amb dues configuracions diferents del reactor HWCVD (p, d_{f-s} i p', d'_{f-s}) és $\frac{r'_d}{r_d} = \frac{d_{f-s}}{d'_{f-s}}$. La validació d'aquesta llei d'escala s'ha posat a prova experimentalment duent a terme una sèrie de dipòsits, variant la concentració de silà, de capes de silici amorf (a-Si:H) i microcristal·lí μc-Si:H amb dues configuracions de reactor diferents. Els resultats experimentals mostren que, en el cas del material amorf, el ritme de dipòsit varia d'acord amb la llei d'escala anteriorment esmentada. Pel que fa al material microcristal·lí, observem petites desviacions respecte la llei d'escala que es fan més evidents per a baixes concentracions de silà. Finalment, mostrarem un

treball preliminar pel que fa a l'optimització de material μc-Si:H, dipositat a elevats ritmes de dipòsit r_d=2±0.3 nm/s. En aquests experiments, hem utilitzat una xarxa catalítica formada per 12 filaments paral·lels de 0.175 mm de diàmetre i 20 cm de longitud que estan separats els uns dels altres per una distància d_{f-f}=16 mm. La distància dels filaments al substrat va ser fixada a d_{fs}=18 mm en lloc dels 50-80 mm habitualment utilitzats per al dipòsit de material μc-Si:H d'alta qualitat. La qualitat del material dipositat es va avaluar indirectament mitjançant la supervisió, usant espectroscòpia infraroja per transformada de Fourier (FTIR), de la progressió dels processos d'oxidació post-dipòsit que afecten les mostres. La signatura de l'espectre IR del material μc-Si:H optimitzat de forma preliminar, demostra que quan s'utilitzen d_{fs} tan curtes com en el nostre cas, el millor material μc-Si:H s'obté per a una pressió de treball $p \approx$10 Pa (en lloc de l'habitual $p \approx$1-5 Pa). Aquest règim de treball permet obtenir mostres de material μc-Si:H, dipositades a alta velocitat, amb una oxidació post-dipòsit considerablement reduïda.

Abstract

The first block of this thesis deals with the study of the degradation process of tungsten catalytic filaments in the field of silicon deposition with the Hot Wire Chemical Vapour Deposition (HWCVD) technique. The development of technological solutions addressed to the filaments protection will also be dealt. The second block deals with the scaling up of HWCVD towards large area and the existence of a scaling law that may allow the deposition of microcrystalline silicon (μc-Si:H) at high rate preserving the material quality.

We will firstly expose a brief introduction about micromorph solar cells, the current limitations, related to the deposition of μc-Si:H, for making the production of micromorph modules economically profitable and the potentiality of HWCVD for overcoming such limitations.

Next, it will be experimentally shown that the decay of the catalytic performance of the filaments is initiated after a first stage of Si atoms dissolution in the filament and that the duration of this first stage is only of a few hours. Using a diffusion model, we will show that, in most practical situations, the duration of said Si atoms dissolution stage is independent of the chosen filament radius. An electric model will be used to check the status of the filament degradation process at real time by simply monitoring the slope of the filaments electric resistance. We will show that the end of the Si atoms dissolution stage corresponds to an abrupt change in the slope of the filaments electric resistance.

We will expose an own-developed protection device, *the self cleaning cavity*, that offers an effective protection for the filaments cold ends against silicidation. By implementing such protection devices, the silicides formation at the filament cold ends is reduced to a rate lower than that at the central portion of the filament. We will show the results of the validation tests of an own-developed au-

tomatic filament replacement mechanism, that allows replacing a used portion of a filament by another clean portion of filament, without breaking vacuum. This filament replacement mechanism includes a tension adjustment mechanism that allows keeping tense, in all operating situations, the portion of filament that is going to be used for the deposition of the film. We will show that the developed filament replacement mechanism, in combination with the use of self cleaning cavity protection devices, guarantees the repeatability and stability of a HWCVD deposition process for silicon based materials. As far as we know, it has not ever been reported before the construction of such a HWCVD apparatus.

After that, we will show the existence of a *large area limit* that allows studying, using a relatively small catalytic filament net, the behaviour of any arbitrary larger reactor. If the filaments configuration is conveniently chosen, we will see that excellent ($< \pm 2.5\%$) thickness uniformity of the deposited films can be achieved. We will also expose a radicals diffusion model that allows predicting with great accuracy, the thickness profiles of the deposited films.

We will expose the possible existence of a scaling law that could allow the increase of the deposition rate, r_d, of μc-Si:H layers, using silane and hydrogen as precursor gases, while preserving the quality of the deposited material. Said scaling law only holds if the product $p \cdot d_{f-s}$ (working pressure times the filament to substrate distance) and the ratio between the silane and hydrogen partial pressures, p_{SiH_4}/p_{H_2} are kept constant. If these two conditions are satisfied, the expected ratio between the deposition rates achieved with two different HWCVD configurations (p, d_{f-s} and p', d'_{f-s}) is $\frac{r'_d}{r_d} = \frac{d_{f-s}}{d'_{f-s}}$. The validation of this scaling law has been experimentally tested carrying out a series of depositions of amorphous silicon (a-Si:H) and μc-Si:H layers, varying the silane concentration, with two different reactor configurations. The experimental results show that in the case of a-Si:H material, the deposition rate varies according to the aforementioned scaling law. For μc-Si:H material, we observe small deviations which become more evident for low silane concentrations.

Finally, we will show a preliminary work regarding the optimisation of μc-Si:H material at high deposition rates $r_d = 2 \pm 0.3$ nm/s. In these experiments, we have used a catalytic net formed by 12 parallel filaments of 0.175 mm diameter and 20 cm length which are separated from each other by a distance of d_{f-f}=16 mm.

The filaments to substrate distance was fixed to d_{f-s}=18 mm instead of the usual 50-80 mm used for the deposition of high quality μc-Si:H. The deposited material quality was indirectly evaluated by monitoring, using Fourier Transform InfraRed spectroscopy (FTIR), the progression of the post-deposition oxidation processes affecting the samples. The IR spectrum signature of the preliminary optimised μc-Si:H material shows that when such short d_{f-s} are used, the best μc-Si:H material is obtained for a working pressure p $\approx$10 Pa (instead of the usual p $\approx$1-5 Pa), resulting in samples with a considerably reduced post-deposition oxidation.

Contents

Chapter 1

Introduction

The photovoltaic (PV) industry sector has experienced, in the last decade, annual market growth rates between 40% and 90% with a PV production increase of almost two orders of magnitude [1]. About 83% of the PV production in 2011 used wafer-based crystalline silicon (c-Si) technology while the rest 17% was taken by thin film PV technology [2]. Indeed, thin film PV production has boosted since 2005 due to the irruption of companies offering turn-key production lines for thin film PV modules, combined with a temporary shortage of c-Si feedstock. Over 150 companies (most of them in Asian countries) announced in 2011 an start or increase of thin film PV production and, if all the expansion plans were realised in time, thin film PV production capacity could be around 24% of total in 2015 [2]. However, the present economic context and the large price reduction of c-Si in the last three years is putting a lot of pressure in many newcomer thin film PV factories which risk struggling in the current market scenario. In terms of mid-long term projected thin film PV capacity increases, thin film silicon is expected to be the leading technology, followed by CIGS and CdTe. It is probable that in an eventual future scenario of several hundreds GW of PV energy production, thin film Si will be the only technology that may sustain such a large market growth rate. The main reasons for this are: virtually unlimited raw materials abundance, strong synergy with flat panel display industry and a large road beyond for further increases in modules efficiency. At present, most of the Si based thin film PV companies produce amorphous silicon (a-Si:H) modules while just a few of them use a micromorph structure [3], which basically consists in amorphous and microcrystalline

silicon (μc-Si:H) stacked solar cells, for tandem modules fabrication.

1.1 The micromorph concept: an upgrade for Si thin film PV factories

In order guarantee their future survival, Si film PV factories must find the way of increasing modules efficiency and reducing manufacturing costs which allow offering a competitive price per Watt produced. The micromorph concept constitutes one of the most promising silicon based technologies for the upgrading of Si thin film solar cell factories. Fig. 1.1 depicts schematically the structure of a micromorph solar cell.

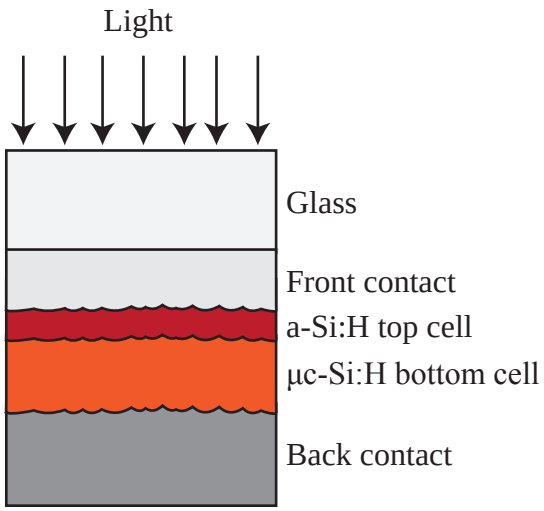

Figure 1.1: Basic structure of a micromorph (a-Si:H/μc-Si:H) solar cell. The different layer thicknesses are not depicted in scale.

The combination of two stacked solar cells using a-Si:H and μc-Si:H active layers, with different bandgap energies of approximately 1.75 eV and 1.1 eV respectively, induces light absorption within a wider range of the solar spectrum. In a micromorph tandem solar cell, the top a-Si:H cell mainly collects photons with energies within the visible range whereas the bottom μc-Si:H solar cell enhances

Table 1.1: Efficiency of a-Si:H/μc-Si:H and a-Si:H commercial modules and record solar cells at laboratory scale [4] (as of June, 2012). Data for a-Si:H/μc-Si:H and a-Si:H modules efficiency have been collected from various manufacturers specification data sheets.

	a-Si:H	a-Si:H/μc-Si:H
Laboratory scale	10.1 %	12.3%
Commercial module	~7-8%	~9-10%

the absorption in the red and near infrared region. This leads to an increase of the photogenerated current in comparison with a single a-Si:H or μc-Si:H solar cell resulting in higher energy conversion efficiencies. In addition, the production of micromorph modules does not entail the usage of any additional precursor gases. Table 1.1 shows the increase in efficiency achieved with the micromorph structure in comparison with single junction a-Si:H solar cells.

Due to the lower optical absorption coefficient of μc-Si:H (compared to that of a-Si:H), in micromorph solar cells, the thickness of the active layer of the μc-Si:H bottom cell must be around five times larger (~1 μm) than that of the top a-Si:H cell (~200 nm). Since the current deposition rate, r_d, of high quality a-Si:H is around 0.2-0.5 nm/s [5], in order to keep a high production throughput in micromorph thin film PV factories, the deposition rate of μc-Si:H layers must be increased up to r_d >1 nm/s. However, achieving such high r_d for high quality μc-Si:H layers is a big challenge, from either a technological and a engineering point of view, that has not yet been overcome at an industrial scale. Nowadays, this latter issue constitutes a major limitation for making economically profitable the industrial production of micromorph modules.

1.2 Current limitations in PECVD μc-Si:H deposition

At present, for μc-Si:H layers deposition, the Plasma Enhanced Chemical Vapour Deposition (PECVD) technique is the most widely used technology and the only one that has reached industrial relevance. Briefly speaking, in PECVD, the precursor gases used for the films deposition are introduced into a vacuum chamber trough a gas inlet. Said vacuum chamber includes two parallel electrodes: one

grounded (holding the substrate) and the other connected to an electrical RF power supply system (used as the precursor gas shower). If a high RF voltage (typically using a frequency of 13.56 MHz) is applied between both electrodes, a glow discharge or "cold plasma" is originated thus activating the dissociation of the precursor gas molecules and initiating the deposition process. The residual gases are evacuated through a pumping system.

High deposition rates up to 10 nm/s [6] can be achieved with the standard PECVD technique by combining the so-called high pressure depletion (HPD) regime [7] with the very high frequency (VHF) approach [8]. In the HPD regime, high deposition pressures in the range of 10^3 Pa are used [9, 10]. In the VHF regime, the used plasma excitation frequency is usually in the range of 40-150 MHz. This combination (HPD-VHF) allows obtaining high quality material at high r_d which results in high conversion efficiencies of μc-Si:H solar cells; η=6.3% for r_d=8 nm/s [11] and η=9.1% for r_d=2.3 nm/s [9] or micromorph solar cells; η=9.6% for r_d=1 nm/s [12]. However, the aforementioned efficiencies correspond to cells with an effective area around 0.25 cm^2 for [9, 11] and 1.25 cm^2 for [12]. We must notice that depositing high performance μc-Si:H i-layers for solar cells over large area using the HPD-VHF regime in PECVD entails a major technological challenge. Indeed, when the wavelength of the plasma excitation becomes comparable to the substrate dimensions, the PECVD technique is affected by plasma standing surface waves effect, which can compromise the uniformity of the film [13, 14]. Thus, using very high excitation frequencies (*i.e.* lower equivalent wavelengths) leads to large inhomogeneities in the thickness of the deposited film. This makes it difficult to achieve high deposition rates (>1 nm/s) using VHF sources and, simultaneously, keeping a reasonable thickness uniformity on the whole substrate [15, 16]. Since the structural uniformity of the intrinsic μc-Si:H layer is crucial to preserve the efficiency of the cells [17, 18], this undesirable effect compromises the performance of large area (>1 m^2) modules when the HPD-VHF approach is used for the intrinsic μc-Si:H layer deposition. For instance, if an excitation frequency of 100 MHz is used and the substrate dimensions are about a quarter of the frequency-equivalent vacuum wavelength ($\sim$0.75 m), the obtained thickness inhomogeneities are around $\pm$25% [19]. Thickness inhomogeneities of μc-Si:H layers deposited at 2.5 nm/s can be further reduced to $\pm$15% by using novel antenna type electrodes [20, 21] and a voltage phase modulation method that requires very complex VHF power supply

systems. Nevertheless, even lower thickness variations around ±13% produce critical variations in the deposited films crystallinity [22]. In any case, the achieved thickness uniformities using the HPD-VHF regime over large area are still far from the standard thickness uniformity (around 5%-10%) achieved with industrial PECVD reactors [5] using 13.56 MHz excitation frequencies. Moreover, if intermediate excitation frequencies are used, the HPD regime becomes susceptible to form powder in the reactor [18, 23]. On the whole, even though many efforts are being focused in developing novel electrode shapes or exploring "non-standard" deposition regimes in PECVD, the objective of depositing high quality μc-Si:H layers over large area (>1 m^2) and at high deposition rate (r_d >1 nm/s) has not yet been accomplished and still complex technological obstacles need to be overcome.

1.3 Deposition of μc-Si:H with HWCVD

The Hot Wire Chemical Vapour Deposition (HWCVD) technique, also known as catalytic CVD (cat-CVD) [24], has arisen in recent years as a promising alternative for the deposition of μc-Si:H. Contrary to PECVD, in HWCVD the energy required for the precursor gases dissociation and the subsequent initiation of the film growth is provided as thermal energy by the action of incandescent filaments (usually tungsten or tantalum filaments heated up to temperatures around 1500-2000°C by Joule effect) in a catalytically activated decomposition process. The substrate is usually located facing the catalytic filament net inside a vacuum chamber fed by the precursor gases through a gas inlet. A pumping system evacuates the residual gases from the deposition chamber. Regarding a-Si:H and μc-Si:H deposition for solar cells applications with HWCVD, the reader may find detailed information in some published extended reviews [25–27]. A summary of the application fields of HWCVD and some clues of its industrial implementation can be found in [28]. Finally, to get a general picture of the research state of the art in the field of HWCVD, the reader may consult reference [29]. Let us just highlight the most relevant facts concerning the scope of this thesis work:

Firstly, HWCVD has the potential to deposit μc-Si:H layers at high deposition rate [30, 31] and low deposition pressure (1-20 Pa). Secondly, high quality μc-Si:H solar cells with the intrinsic layers deposited with HWCVD have already been ob-

tained. The efficiencies of these solar cells are equal to those obtained for μc-Si:H solar cells prepared entirely by PECVD [27]. Furthermore, the lack of ion bombardment allows obtaining sharp p/i interfaces, leading to an enhanced extraction of the photogenerated carriers in HWCVD μc-Si:H solar cells [32]. Thirdly, the kinetics of the radicals, generated at the filaments surface and moving towards the substrate, is governed exclusively by the diffusion of the different chemical species. As no plasma is used to generate the radicals, the homogeneity of the deposited films is not affected by the standing waves effect characteristic of the PECVD technique, thus making much easier the scaling up of HWCVD towards large areas without any loss in the film's homogeneity [33–35].

Such noticeable advantages of HWCVD, have attracted the attention of various industry sectors such as the flat panel displays, thin film PV or hard coating industries. However, the industrial exploitation of HWCVD is up to now strictly limited by certain technological features that impede this technique achieving industrial relevance.

1.4 Current limitations in HWCVD μc-Si:H deposition

Although high r_d up to several nm/s for μc-Si:H layers deposition can be achieved with HWCVD, the obtained material in such high r_d regimes is of poor quality. At present, the standard r_d for high quality μc-Si:H layers is below 0.5 nm/s [27,36,37]. It is then necessary to put investigation efforts in exploring alternative deposition regimes or strategies that may allow increasing the r_d of μc-Si:H layers with HWCVD while preserving the material quality. In any case, one should notice that the r_d achieved in industrial-size PECVD reactors for μc-Si:H layers deposition is as well below 0.5 nm/s [5]. In fact, the most limiting factor to industrially exploit the HWCVD technique is, undoubtedly, the filaments degradation issue, commonly known as "filament ageing". In the particular case of silicon based materials deposition, it is well known that the used filaments (made of either tungsten or tantalum) are severely affected by silicides formation. This leads to a reduction, or even suppression, of the filaments catalytic performance. Furthermore, the formation of silicides entails structural damages which finally cause the catalytic

filament(s) breakage that, in the best cases, takes place after a few hundreds hours of usage. When this occurs, the deposition process must be interrupted to replace the broken filaments by new ones. Of course, this is completely unacceptable for any industrial process, wherein large operating times without maintenance stops are required. Hence, in order to make real the prospects of implementing HWCVD reactors at an industrial scale, it is mandatory developing novel HWCVD systems that allow overcoming the problem of filaments ageing.

1.5 Scope of the thesis

The goal of this thesis work is to explore different strategies and develop technological solutions addressed to overcome the current limitations of the HWCVD technique for its eventual industrial exploitation in the field of Si thin film solar cells. The following chapters are focused on three main subjects: The filaments degradation issue, the scaling up of the HWCVD technique towards large area and the deposition of μc-Si:H at high deposition rate.

In Chapter 2, it will be exposed a systematic study of the silicidation processes affecting tungsten filaments at high filament temperature during a-Si:H and/or μc-Si:H deposition. We will discuss the different stages of the filaments silicidation process and their influence in the filaments electric resistance. Next, we will deal with the issue of filament protection against silicidation. We will focus on the development of an effective protection device against silicidation for the filaments cold ends, wherein breakage usually takes place. This protection device is compatible with an own-developed automatic filament replacement mechanism that allows changing the used filaments by new ones, without breaking vacuum and keeping tense the filaments in all operating situations. The proposed designs of said technological solutions and the experimental results of their corresponding validation tests will be exposed in Chapter 3. In Chapter 4, a discussion about the scalability of the HWCVD technique towards large area will be exposed. We will deal with the issue of film thickness uniformity. We will also discuss about the possible existence of a scaling law in HWCVD that allows increasing the deposition rate of μc-Si:H layers maintaining the material quality. An experimental work, addressed to the confirmation of this possibility, is exposed in Chapter 5.

Chapter 2

Filament Degradation

2.1 Introduction

In essence, any chemical reaction can be understood as breaking atom bonds and creating new ones. A catalyst affects the rate of a certain chemical reaction by lowering the amount of energy that must be surmounted to activate it. When the catalyst is in a different phase than the reactant, like in a HWCVD process, the catalytic process is known as heterogeneous catalysis. The surface chemistry involved in heterogeneous catalysis is extremely complex when studied at an atomic scale in non-equilibrium conditions [38]. However, things turn out easier if we consider the case of steady state conditions and the subject is dealt using statistical mechanics. In a HWCVD process, the activation energy necessary to decompose the precursor gas molecules is provided as thermal energy by a catalytic heated filament which is usually made of a refractory metal. In the case of a-Si:H or μc-Si:H deposition, the most used precursor gas is silane (SiH_4), which is usually diluted with hydrogen, whereas the catalytic filaments are usually made of tungsten (W) or tantalum (Ta).

When SiH_4 molecules enter in contact with the catalytic filament, this last provides the energy necessary to cleave four Si-H bonds, following the reaction

$$SiH_4 \rightarrow Si + 4H \,, \tag{2.1}$$

thus producing Si and H radicals with a dissociation probability that depends on the filament material and its temperature T_{fil}. Of course, there exist many other intermediate reactions [39] which have great influence on the quality of the deposited film.

The measured apparent activation energies of Si radicals production for W and Ta catalysts are, respectively, 50-80 kcal/mol and 140-180 kcal/mol [39–41]. Such results indicate that W filaments are very good candidates to be used as catalysts in HWCVD for depositing silicon based materials. Comparing these values to the energy required to pyrolytically break the four Si-H bonds of silane, 308 kcal/mol [42], it is clear that the decomposition of silane on W or Ta filaments is catalytically activated.

Unfortunately, independently of the chosen material, the lifetime of the catalytic filaments used for a-Si:H or μc-Si:H deposition is very limited. During its usage time, a W (or Ta) filament is affected by the formation of silicides which alter its chemical composition. Accordingly, used filaments also experience changes in their emissivity and electrical resistivity values. The dynamics of the silicidation process of a filament depends on the used precursor gas mixture, the filament material and, of course, the deposition conditions. The resulting degradation process of used catalytic filaments is commonly known as "filament ageing". Furthermore, the density mismatch between the different chemical phases present in an aged filament leads to lattice expansion effects that introduce tensile stresses which may cause crack formation and, eventually, the breakage of the filament. Nevertheless, even if an aged filament does not break during the deposition process, it may not be any longer useful because the filament ageing often entails a reduction of its catalytic properties [43], thus affecting the reproducibility of the deposited films in terms of both material quality and deposition rate [44, 45]. At present, the filaments degradation issue constitutes the major limiting factor to industrially exploit the HWCVD technique for the deposition of Si based thin film materials. Several works dealing with the silicidation process of filaments during a-Si:H or μc-Si:H deposition with HWCVD have been published in the last decade for either tantalum [46–50] or tungsten [43, 45, 47, 50–52] filaments. Although there exist slight differences, the silicidation processes of Ta and W filaments are very similar. We decided to use W filaments in our HWCVD reactor (described in Appendix A) due to the good catalytic performance, low cost and market availability of tung-

sten. Hereinafter, the results presented in this chapter and the ongoing discussion only deal with the degradation of W filaments. The reader can find more information about the particularities of the silicidation process of Ta filaments in the suggested bibliography.

It is well known that when W filaments are used as catalysts in HWCVD for a-Si:H or μc-Si:H deposition, silicide formation is faster at those filament regions close to the corresponding electrical contacts, i.e. the so called *cold ends*. Therefore, the filament breakage usually occurs at its cold ends. It has been observed that silicides formation usually begins at the filament cold ends and then progressively expands towards the middle of the filament [47]. However, the central portion of the filaments, defined as the portion of filament that is located between the silicide fronts expanding from the cold ends, is also affected by silicidation. The formation of silicides at the central portion of the filament reaches its maximum rate at a filament temperature, T_{fil}, of 1650°C [51]. If T_{fil} >1650°C, the silicidation process of the central portion of the filament is considerably slowed down. Furthermore, it has been suggested in previous works [45, 47, 51] that if W filaments are used at T_{fil} >1800°C, silicides formation is almost suppressed. Given that, if the filament cold ends were efficiently protected it would be expected to achieve industrially relevant filament lifetimes for this high T_{fil} >1800°C regime. This scenario could open the door to the industrialisation of HWCVD technique for depositing, for instance, device quality μc-Si:H layers to be used as absorbers in tandem solar cells. However, it is premature to stablish such conclusions. In particular, Honda et. al. [51] studied the silicidation kinetics of 0.5 mm diameter W filaments at filament temperatures T_{fil}=1450°C-1750°C under a-Si:H deposition conditions. Honda et. al. reported in that paper that, for T_{fil}=1450-1650°C, the silicidation of the central portion of the filament starts from the beginning of the deposition process and that the formed silicide layer is exclusively composed of the silicon rich tungsten silicide phase WSi_2. For filament temperatures between 1700°C and 1750°C, the formed silicide layer contains both WSi_2 and W_5Si_3 composites, suggesting that a transition phase from WSi_2 to W_5Si_3 formation takes place at these temperatures. In that paper it is also reported that for T_{fil}=1850°C it takes longer SiH_4 exposure times (180 min) to observe any appreciable (thickness is not specified) silicide layer which is exclusively constituted by W_5Si_3. The authors conclude that the formation of WSi_2 is apparently suppressed in this high T_{fil} regime.

There exist other similar works that deal with the silicidation process of tungsten metal plates at lower temperatures (1000°C-1200°C and 1300°C-1500°C) [53, 54]. However, the reported data dealing with tungsten silicidation at temperatures above 1800°C are, if not absent, very scarce. To our knowledge, it has not been yet published any systematic study of the silicides growth kinetics in W filaments in the high T_{fil} >1800°C regime. Moreover, even if the filament breakage does not occur, it is not clear if its catalytic performance and, in consequence, the reproducibility of the deposited films, would be guaranteed at long term (several hundreds of hours) if W filaments were used at said high T_{fil} regime in HWCVD for the deposition of a-Si:H and/or μc-Si:H films.

In this chapter we report the results obtained from a systematic study of the degradation of W filaments in the high T_{fil} regime (T_{fil} ≈1850°C) used as catalysts in HWCVD under deposition conditions compatible with a-Si:H deposition using pure SiH_4 as precursor gas.

We will show that the central portion of a W filament goes through three different stages during its usage time. There is a first stage of Si atoms dissolution in the W filament wherein there is no silicide formation. The duration of this first stage is what we call the *time delay* t_0. At $t = t_0$, the Si concentration in the W filament reaches its solubility limit and the second stage begins. Then, the W_5Si_3 silicide phase precipitates and a W_5Si_3 outer corona is formed, growing in depth at expense of the pure W bulk. A diffusion model, applied to the stage of Si atoms dissolution in W, will be exposed to discuss the behaviour of t_0. Finally, when the Si atoms concentration exceeds the solubility limit of Si in W_5Si_3, an outer corona of WSi_2 is formed and it progressively grows at expense of the previously formed W_5Si_3 silicide layer. This constitutes the third stage that in essence, is analogous to the second one. We will show that the initiation of the second stage at $t = t_0$ entails the beginning of the decay of the catalytic performance of the filament. We will also show that the time delay t_0 is stabilised if the new W filaments are subject to a pre-deposition annealing treatment. Furthermore, we will also show that if the SiH_4 precursor gas is diluted with pure H_2, the time delay t_0 is considerably increased. In addition, we will expose an electric model that allows obtaining information about the progress of the silicidation process of the filaments at real time by monitoring the filaments electric resistance.

2.2 Silicidation study of a tungsten filament at high temperature

The following study is based on the analysis of the data obtained in a series of depositions (silicidation tests) that were carried out in our HWCVD reactor. The main objective was to study the silicidation processes affecting the central portion of a tungsten filament used as catalyst in HWCVD when pure silane, SiH_4, is used as precursor gas. Such silicidation tests were carried out under a-Si:H deposition conditions, being the accumulated silane exposure time the only variable parameter. Very thin filaments of 0.125 mm diameter (instead of the usual 0.5 mm diameter filaments used in the previously cited works) were used to minimize the deposition time needed to obtain highly silicidated filaments. All silicidation tests were performed using a fixed electrical DC current to heat the filaments by Joule effect. The monitoring of the filaments electric resistance, R_{fil}, gave information about the ongoing degradation process in each silicidation test. For each silicidation test, the total amount of silicides formed in the central portion of the filaments as well as the identification of the present silicide phases were determined by means of Scanning Electron Microscopy (SEM), Energy Dispersive X-ray spectroscopy (EDX) analysis and Raman Spectroscopy. The obtained results were interpreted with the help of a diffusion model and an electric model.

2.2.1 Experimental details

All silicidation tests have been carried out in our single chamber HWCVD reactor described in Appendix A. A single W filament of 0.125 mm diameter was used in each test. The filaments were heated at a temperature T_{fil} ≈1850°C by Joule effect and exposed to a pure SiH_4 atmosphere at a pressure of $p = p_{SiH_4}$=2 Pa using a SiH_4 flow rate Φ_{SiH_4}=12 sccm. Such conditions are typical for a-Si:H deposition and are similar to those used in previous works [46, 47, 51]. The details concerning the measurement of T_{fil} are given in Appendix A. The base pressure of the deposition chamber was always lower than 10^{-4} Pa. The electric current flowing through the filament, I, was fixed at 1.63 A using a DC power supply. By fixing the electric current instead of the applied voltage, it is assured that the local

dissipation of power (per unit length) $P_J = I^2 R'_x$ only depends on the silicidation state at that particular point x; R'_x is the electric resistance per unit length at x. In that way, we can assure that at any point of the central portion of the filament, the local temperature is kept at 1850°C as long as silicides formation is not yet initiated there. The filament electric resistance time evolution $R_{fil}(t)$ was monitored in all the silicidation tests that were carried out. Once each deposition was completed, little portions of the aged filaments were collected as samples. Those samples were taken from the central portion of the filament, located between the two advancing silicide fronts originated at the filament cold ends. The filaments length was chosen long enough (L_{fil}=30 cm) in order to avoid any contribution of the silicide fronts advancing from the filament cold ends. The accumulated SiH_4 exposure times t varied from 3 min to 190 min (L_{fil} was 40 cm for the 190 min silicidation test). The collected samples were embedded into a corresponding conductive resin matrix which was subsequently sliced and mirror-like polished in order to obtain clearly visible cross sections of the filament as much perpendicular to the filament axis as possible. Morphological studies and chemical analysis of the samples were performed by means of SEM (Jeol JSM-840 and Quanta 200 FEI) equipped with an X-ray microanalysis system (INCA Energy 250, Oxford Instruments). In addition, micro-metric mappings of the samples were performed using Raman spectroscopy (Micro Raman T64000 Jobin Yvon, $\lambda_{laser} = 532nm$, $\mathcal{P}_{laser}$=4.3 mW) in order to obtain the distribution map of W, W_5Si_3 and WSi_2 for each of the collected samples.

2.2.2 Results

The first interesting result comes out from direct observation of the deposition process. Indeed, one can easily notice an abrupt change in the brightness of the filament at the position of the silicide fronts advancing from the cold ends. From EDX measurements, we know that the portions of filament located between the cold ends and the corresponding silicide fronts are constituted by WSi_2. With the help of an aluminum plate riddled with holes every 5 mm acting as a ruler (see Fig. 2.1), we could measure the propagation velocity of such WSi_2 front which turned out to be approximately constant after 15-20 min since the beginning of the deposition process with a value v=(4.0±0.3)·10^{-4} m/min.

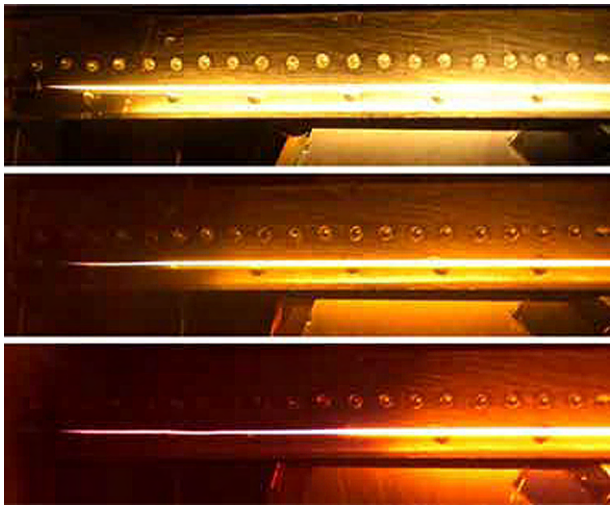

Figure 2.1: Advancing WSi_2 front from a filament cold end during a silicidation test. The holes in the aluminium plate were performed every 5 mm. The photographs, from top to bottom, were taken at times t=0, 35 and 105 min respectively.

The monitoring of $R_{fil}(t)$ permits to observe any change in the total electric resistance of the filament R_{fil} during the deposition process. Fig. 2.2 shows the $R_{fil}(t)$ curves corresponding to the silicidation tests that resulted in samples (cross sections from the central portion of the filaments) wherein it was latter identified the presence of silicides (WSi_2 and/or W_5Si_3) by means of SEM, EDX and Raman spectroscopy analysis. On the other hand, Fig. 2.3 shows the $R_{fil}(t)$ curves corresponding to those silicidation tests wherein the central portion of the filaments did not reveal any presence of silicides formation. In the following figures of this section, we will maintain the notation of symbols used in Figs. 2.2 and 2.3 to refer to each particular sample.

The first thing we must notice when looking at Figs. 2.2 and 2.3 is that the curves $R_{fil}(t)$ do not look like the same for all the silicidation tests. In particular, the initial tendency of $R_{fil}(t)$ is quite different for each test. However, it is remarkable that, after a first transient period, many $R_{fil}(t)$ curves follow a linear tendency with almost identical slopes (see Fig. 2.2). This linear regime of $R_{fil}(t)$ is only observed for those silicidation tests that resulted in samples with presence of silicides formation. For those silicidation tests with a total SiH_4 exposure time higher than 60 min, the observed linear tendency is maintained beyond. The only

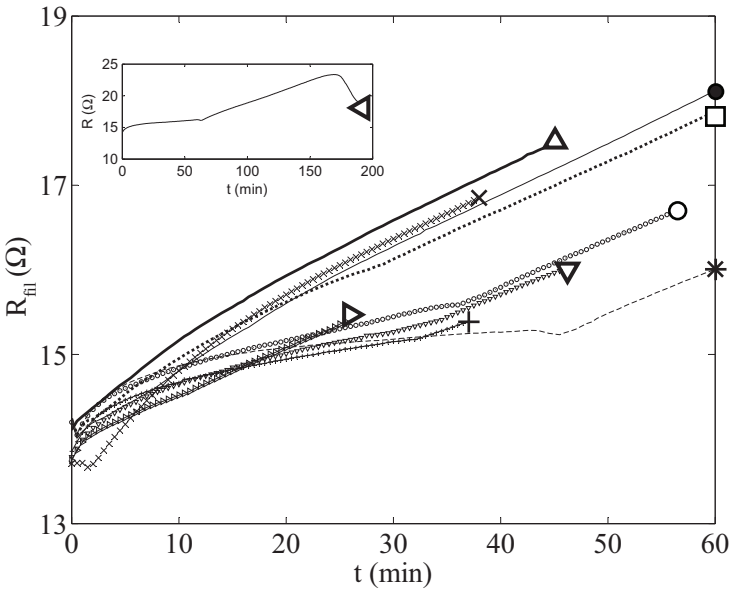

Figure 2.2: $R_{fil}(t)$ curve of the silicidation tests performed with 0.125 mm diameter W filaments (T_{fil} ≈1850°C, I=1.63 A, p_{SiH_4}= 2 Pa, Φ_{SiH_4}= 12 sccm) wherein silicide formation is present at the corresponding samples. In particular, the samples •, □, ∗ and ◁ (see inset) correspond to silicidation tests with a total silane exposure time of 90 min, 75 min, 140 min and 190 min respectively.

exemptions are the silicidation tests that lasted 140 and 190 min. In these two cases, the $R_{fil}(t)$ curves abandon such linear tendency at larger exposure times and a dramatic decrease of the electric resistance holds afterwards. Such trend change in $R_{fil}(t)$ is probably linked to the beginning of WSi_2 formation as those silicidation tests were the only ones that resulted in samples with the presence of a WSi_2 outer corona.

We will now deal with the identification and quantification of any eventual silicide WSi_x presence in the collected samples. Figs. 2.4 and 2.5 show SEM images of cross section samples taken from the central portion of the tested filaments and their corresponding Raman signal mappings, wherein green, red and blue colours indicate the presence of pure W, W_5Si_3 and WSi_2 respectively. Colour saturation gives information about the intensity of the characteristic Raman peaks of W_5Si_3 (red) and WSi_2 (blue) but not in the case of pure W (green) as metals do not exhibit any Raman signature. It must be noticed that the interfaces between the different

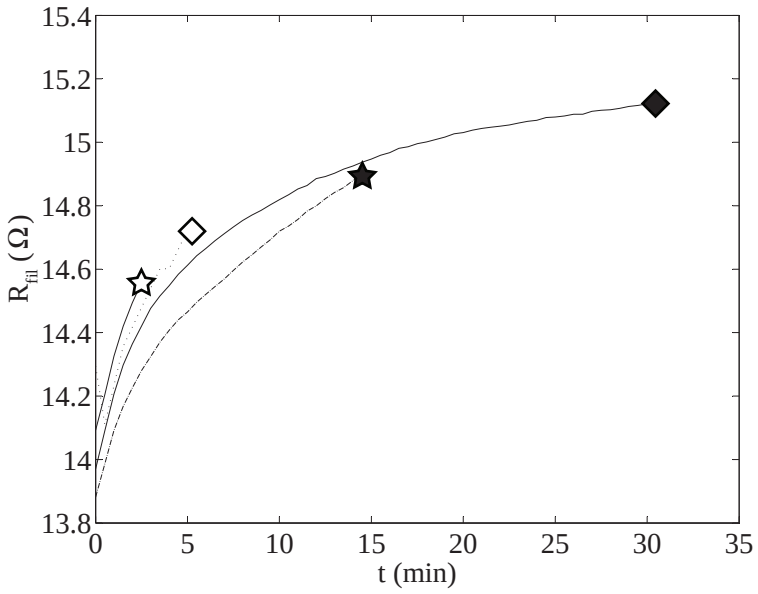

Figure 2.3: $R_{fil}(t)$ curve of the silicidation tests performed with 0.125 mm diameter W filaments (T_{fil} ≈1850°C, I=1.63 A, p_{SiH_4}= 2 Pa, Φ_{SiH_4}= 12 sccm) wherein silicide formation is absent at the corresponding samples.

WSi_x phases are recognizable in the SEM images because the different electric resistivity of each material produces an appreciable contrast in brightness. The increase of the cross section area observed in silicidated filaments is proportional to the volumetric ratio between the corresponding silicide phase and pure W. This volumetric ratio comes from the difference between the molar density of W_5Si_3 (or WSi_2) and that of pure W.

The characteristic Raman signatures of the different WSi_x phases permit the identification of the areas occupied by W_5Si_3 or WSi_2. Fig. 2.6 depicts the measured Raman spectra of such regions showing the characteristic peaks of W_5Si_3 at 117, 170 and 270 cm^{-1} [55] and WSi_2 at 335 and 456 cm^{-1} [55–57]. The Raman signature identification of both W_5Si_3 and WSi_2 phases was confirmed by EDX measurements resulting in Si concentrations of 34-37 at.% and 66-67 at.% respectively.

Once the composition of the different regions observed in the filaments cross section SEM images has been identified as either W, W_5Si_3 or WSi_2, the fraction of W atoms that have reacted and formed either W_5Si_3 ($FR_{W_5Si_3}$) or WSi_2

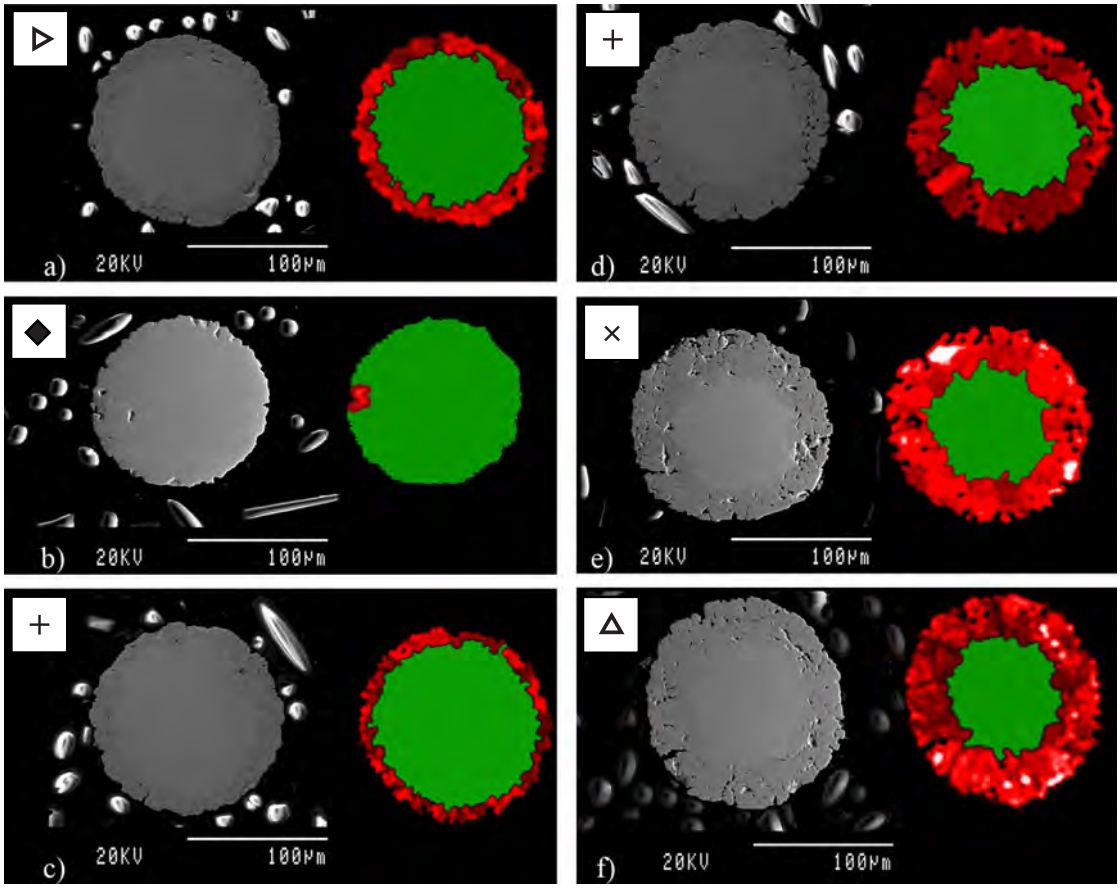

Figure 2.4: Cross sectional SEM images (left) and the corresponding Raman signal mappings (right) of aged 0.125 mm diameter W filaments at T_{fil} ≈1850∘C and exposed to a SiH_4 atmosphere during 26 min (a), 30 min (b), 37 min (c,d), 38 min (e) and 45 min (f). Green and red colours in the Raman signal mappings indicate the presence of pure W and W_5Si_3 respectively. All symbols correspond to those represented in Figs. 2.2 and 2.3.

(FR_{WSi_2}) can be calculated by evaluating the areas covered by each material. For those samples where there is no evidence of neither W_5Si_3 nor WSi_2 presence, one automatically obtains FR_{WSi_x}=0. In the case of samples which show a pure W core surrounded by a W_5Si_3 outer corona, without any WSi_2 presence, the corresponding $FR_{W_5Si_3}$ can be evaluated by two ways:

On one hand, $FR_{W_5Si_3} = A_{W_5Si_3}/(\gamma_{W_5Si_3}A_{fil})$, where $A_{W_5Si_3}$ is the area occupied by W_5Si_3, A_{fil} is the initial cross section area of the filament and $\gamma_{W_5Si_3}$ is the volumetric ratio between W_5Si_3 and pure W. On the other hand, the frac-

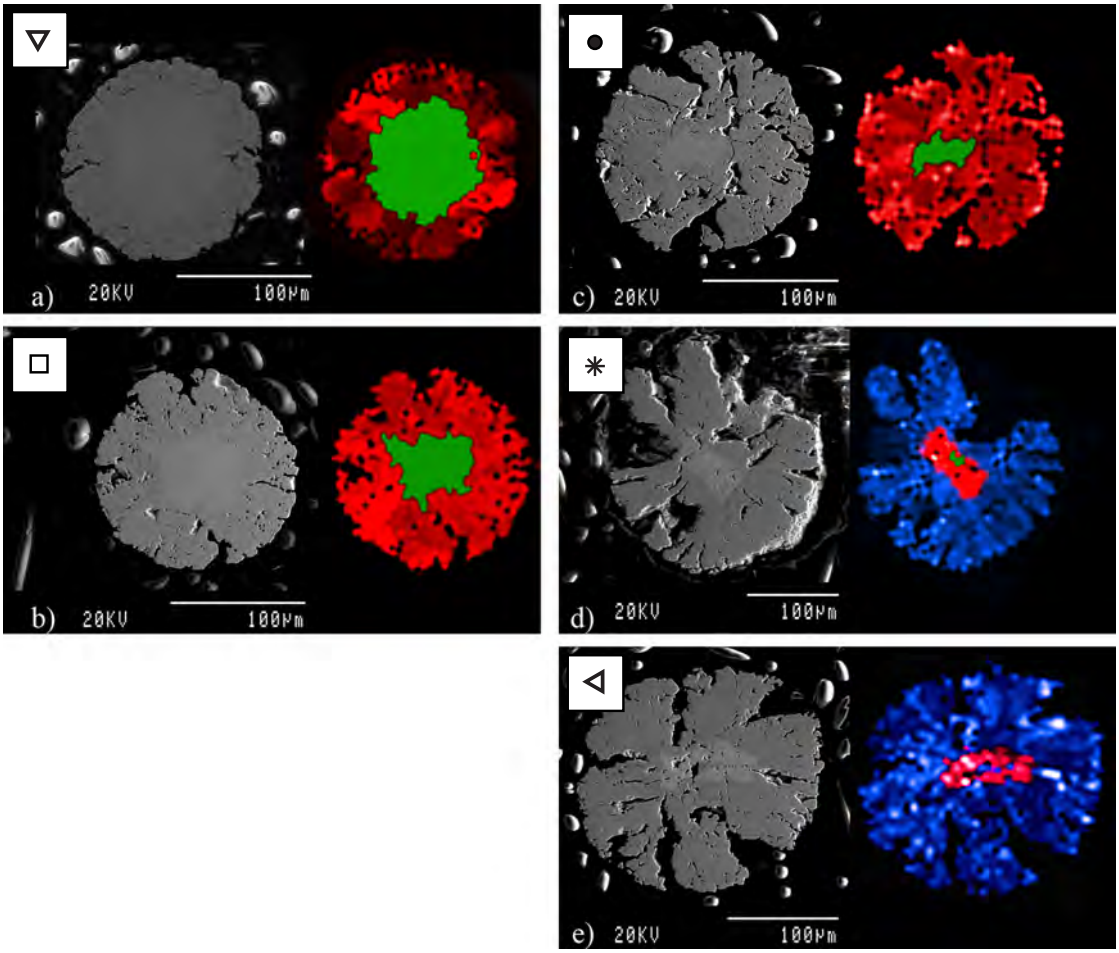

Figure 2.5: Cross sectional SEM images (left) and the corresponding Raman signal mappings (right) of aged 0.125 mm diameter W filaments at T_{fil} ≈1850∘C and exposed to a SiH_4 atmosphere during 46 min (a), 75 min (b), 90 min (c), 140 min (d) and 190 min (e). Green, red and blue colours in the Raman signal mappings indicate the presence of pure W, W_5Si_3 and WSi_2 respectively. All symbols correspond to those represented in Fig. 2.2.

tion of W atoms that have not reacted equals A_W/A_{fil}, being A_W the area occupied by pure tungsten. Then, $FR_{W_5Si_3}$ can also be evaluated as $1-(A_W/A_{fil})$. These two preceding procedures lead, respectively, to a lower and an upper limit value of $FR_{W_5Si_3}$. The calculated lower and upper limit values of $FR_{W_5Si_3}$ for these samples have been plotted in Fig. 2.7 using black and grey symbols respectively. Finally, for those samples which show a presence of both silicide phases, $FR_{WSi_2} = 1 - A_W/A_{fil} - FR_{W_5Si_3}$ where $FR_{W_5Si_3}$ can now only be evaluated as

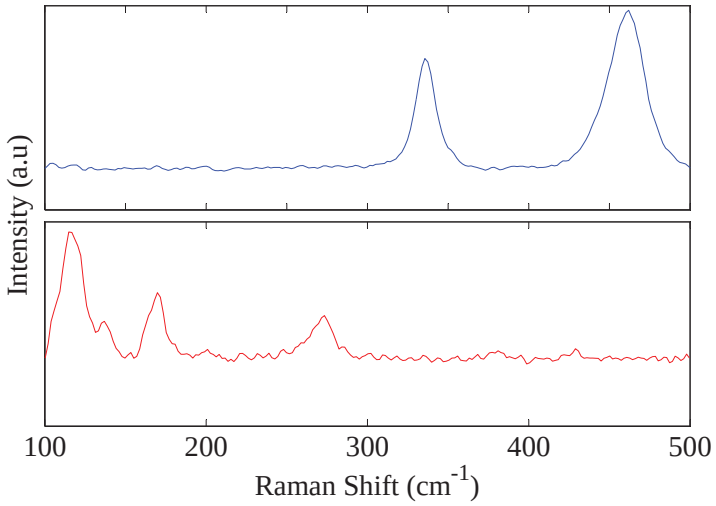

Figure 2.6: Measured Raman signature of the W_5Si_3 (bottom) and WSi_2 (top) regions of aged 0.125 mm diameter W filaments at T_{fil} ≈1850°C and exposed to a SiH_4 atmosphere during 75 min and 140 min respectively.

$A_{W_5Si_3}/(\gamma_{W_5Si_3}A_{fil})$.

Fig. 2.7 shows the calculated values of the fraction of W atoms that have reacted into W_5Si_3 or WSi_2 for each sample as a function of the accumulated SiH_4 exposure time, t. The data points that are vertically aligned correspond to different samples taken from the same tested filament. It can be observed that there is only silicide formation for t >26 min and that the initial formed silicide layer is exclusively composed of W_5Si_3. The necessary SiH_4 exposure time to obtain $FR_{W_5Si_3}$ values close to unity is of the order of 100 min.

Although the increasing trend of $FR_{W_5Si_3}$ with SiH_4 exposure time is recognizable, if we look carefully at the data shown in Fig. 2.7, we can observe some contradictions. For instance, regarding the sample corresponding to t=30 min an almost zero $FR_{W_5Si_3}$ <0.01 was determined. Even though, there is a sample with a lower accumulated SiH_4 exposure time (t=26 min) with higher $FR_{W_5Si_3}$ ≈ 0.2-0.3. For slightly higher exposure times (37-45 min) the data is widely scattered, ranging from a fraction reacted of 0.16 to 0.60. The data plotted in Fig. 2.7 turns out to be a messy aggregation of points as similar SiH_4 exposure times lead to very different values of $FR_{W_5Si_3}$ while higher exposure times do not necessarily correspond to higher values of $FR_{W_5Si_3}$. It is hard to believe that a formed silicide layer

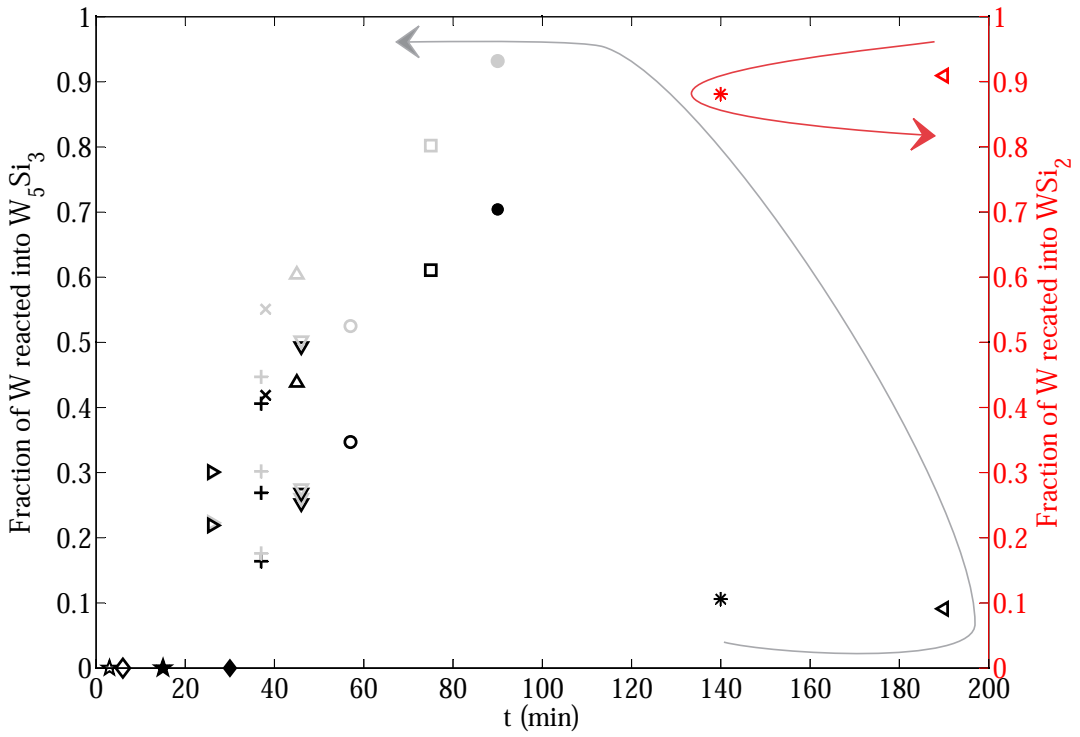

Figure 2.7: Fractional distribution of tungsten in the different silicide phases as a function of exposure time during the silicidation tests of 0.125 mm diameter W filaments at T_{fil} ≈1850°C exposed to a SiH_4 atmosphere (p_{SiH_4}= 2 Pa, Φ_{SiH_4}= 12 sccm). All symbols correspond to those represented in Figs. 2.2 and 2.3. Grey and black symbols indicate, respectively, the higher and lower limit values of $FR_{W_5Si_3}$. Red symbols indicate the FR_{WSi_2} of those samples with presence of WSi_2 precipitates.

can eventually stop growing, decrease for a certain amount of time and afterwards grow again. If we decline such idea, it is not possible to give a satisfactory explanation for the silicides growth process unless the time origin of the experimental data is redefined. Certainly, it is clear that there exists an initial period of time $0 < t < t_0$ wherein no silicide formation is observed. According to the data shown in Fig. 2.7, t_0 takes different values for each of the performed silicidation tests, ranging from 0 minutes to 30 min or even larger values. Given that the deposition parameters were always kept the same for all the silicidation tests, the uncertainty in t_0 must come from differences or particularities in the superficial state of the

used filament in each test.

2.2.3 Discussion of the experimental results

Let us go back to the $R_{fil}(t)$ curves shown in Fig. 2.2. As it has been aforementioned, for all the samples that show any presence of W_5Si_3 formation, the corresponding $R_{fil}(t)$ curves reach a linear regime with approximately the same slope. Hence, it seems reasonable to think that reaching this linear regime of $R_{fil}(t)$ is directly linked to W_5Si_3 formation in the filament. Most of the $R_{fil}(t)$ curves shown in Fig. 2.2 reveal a "critical point" just before entering into the linear regime, where the slope of $R_{fil}(t)$ changes drastically. Before reaching said critical point, the initial trend of these curves resembles to those shown in Fig. 2.3 which correspond to samples without any presence of silicides. Thus, it is a straightforward conclusion that the formation of W_5Si_3 begins at said critical point. We may then try out to set the "silicidation time origin" at this specific moment for each sample, that is to say, introduce a corresponding time delay t_0 in each case. To determine t_0 and its error for each particular silicidation test, it is useful to plot the derivative of $R_{fil}(t)$ curves (see Fig. 2.8). We can easily identify the aforementioned critical points as they entail an abrupt change in dR_{fil}/dt with an S-shaped form. The position and width of this S-shaped curve determine, respectively, the value and the error of t_0 for each sample.

However, if we look again at Fig. 2.2 we can recognize four $R_{fil}(t)$ curves (the upper ones) for which it is not possible to identify any critical point. In these cases, $R_{fil}(t)$ increases monotonically at a higher rate and enters softly into the aforementioned linear regime. A reasonable assumption is that, in these four cases, the formation of W_5Si_3 may have started at any time between the beginning of the deposition process and the moment whenever the linear regime of $R_{fil}(t)$ is approximately reached. Therefore, the determination of the corresponding time delay t_0 includes a larger error.

In total, 14 silicidation tests were performed. As it can be seen in Fig. 2.9, the corresponding values of t_0 are widely scattered within 0-60 min. Thus, when a W filament is used as catalyst in a HWCVD process under the present deposition conditions, it seems to be unpredictable when will the W_5Si_3 outer corona formation begin. For sure, the value of the time delay t_0 will strongly depend on the

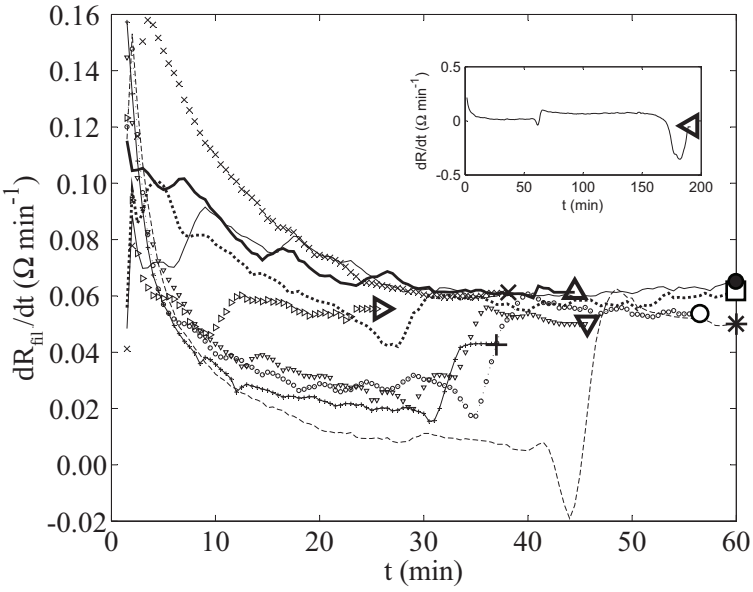

Figure 2.8: Calculated derivative of the $R_{fil}(t)$ curves of the silicidation tests performed with 0.125 mm diameter W filaments (T_{fil} ≈1850°C, I=1.63 A, p_{SiH_4}= 2 Pa, Φ_{SiH_4}= 12 sccm) wherein silicide formation is present at the corresponding samples. The inset shows the derivative of the V(t) curve of a silicidation test with a total silane exposure time of 190 min. All symbols correspond to those represented in Fig. 2.2.

initial superficial status of the tested filament. Certain structural defects at the filaments surface may act as nucleation sites which favour the formation of silicides at that particular point. If that occurs, W_5Si_3 formation will be initiated at those nucleation points and afterwards extend over the filament surface. Indeed, there is no certainty in that the superficial state of a W filament as manufactured is homogeneous all over the filament surface. For instance, if one looks at Fig. 2.4-b it is possible to check how W_5Si_3 formation begins at a particular point of the filament surface instead of being homogeneously initiated. Nevertheless, we will show in section 2.3 that if the W filaments are subject to a pre-deposition treatment, the silicidation process of the filaments turns out to be much more repeatable giving similar values of $t_0 \approx 60$ min.

We can now re-plot the data shown in Fig. 2.7 introducing the corresponding time delay t_0 for each sample, that is to say, plotting $FR_{WSi_x}(t-t_0)$ (see Fig. 2.10) where $t - t_0$ is what we will call from now on, the *effective silicidation time*. The

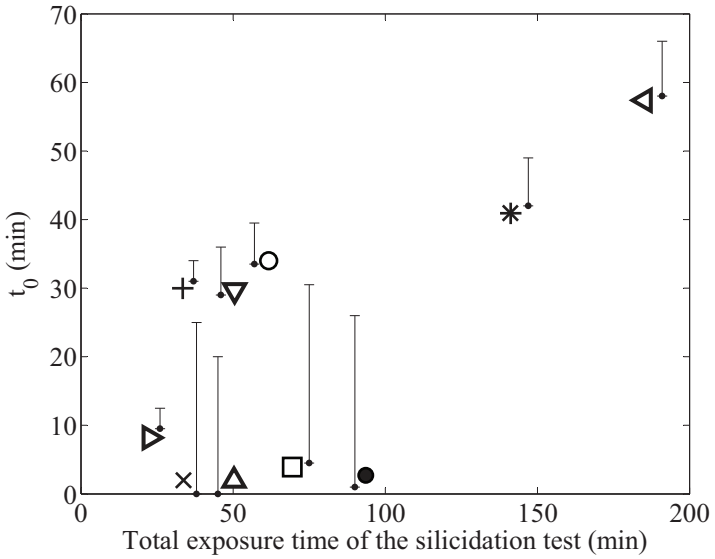

Figure 2.9: Values of the time delay t_0, when W_5Si_3 formation begins, plotted against the total SiH_4 exposure time t, for the silicidation tests performed with 0.125 mm diameter W filaments (T_{fil} ≈1850°C, I=1.63 A, p_{SiH_4}= 2 Pa, Φ_{SiH_4}= 12 sccm) wherein silicide formation is present at the corresponding samples. All symbols correspond to those represented in Fig. 2.2.

data is then rearranged in such a way that the inconsistencies disappear. Despite this, we still have a considerable vertical scattering of the $FR_{W_5Si_3}$ values obtained for low effective silicidation times suggesting that, initially, the formation of W_5Si_3 is very inhomogeneous along the length of the central portion of the filament.

2.2.4 Modelling of the silicidation process of a W filament at high temperature

In this section we will describe in detail the degradation process of a W filament subject to a silicidation test like those described in section 2.2.1.

We will firstly show that, during the deposition process, the central portion of the filament goes through three different stages: (1) Si atoms dissolution in W, (2) W_5Si_3 precipitation and (3) WSi_2 precipitation. To do so, we will use the Si-W phase diagram, assuming that the overall process occurs under quasi-static thermodynamic equilibrium. Secondly, we will use a diffusion model to evaluate

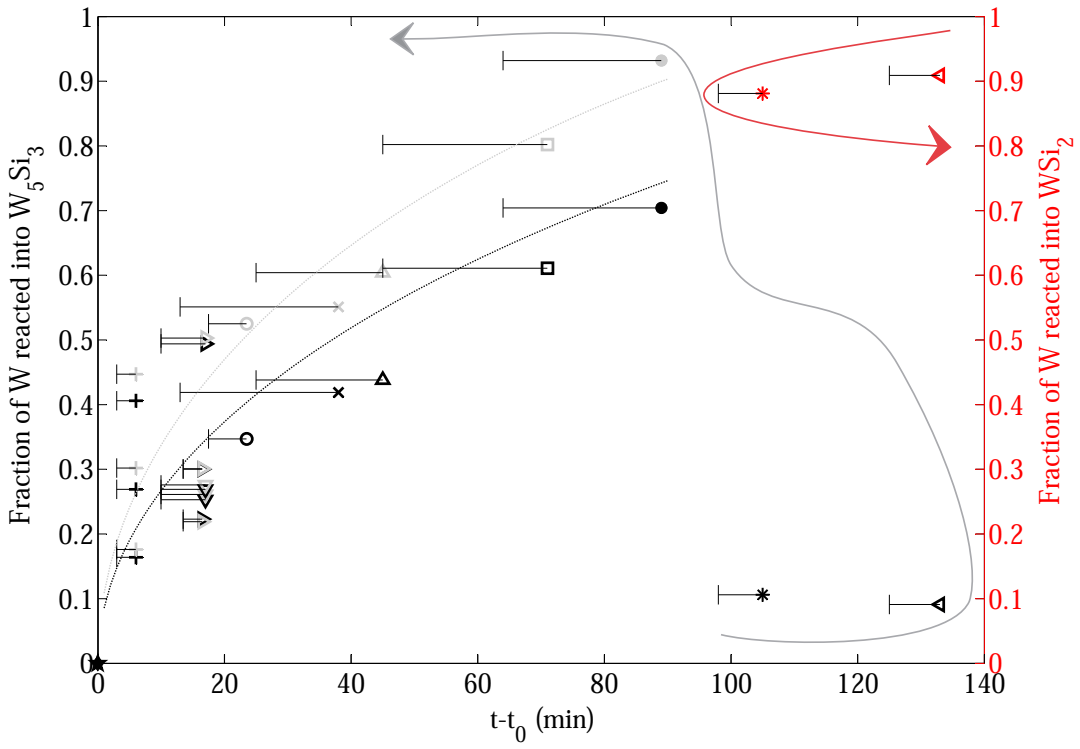

Figure 2.10: Fractional distribution of tungsten in the different silicide phases as a function of the accumulated exposure time $t - t_0$ since W_5Si_3 formation is initiated for the silicidation tests of 0.125 mm diameter W filaments at T_{fil} ≈1850∘C exposed to a SiH_4 atmosphere (p_{SiH_4}= 2 Pa, Φ_{SiH_4}= 12 sccm). All symbols correspond to those represented in Figs. 2.2 and 2.3. Grey and black symbols indicate, respectively, the higher and lower limit values of $FR_{W_5Si_3}$. Red symbols indicate the FR_{WSi_2} of those samples with presence of WSi_2 precipitates. The dotted lines are just guides to the eye.

the duration of the Si atoms dissolution stage (i.e. the time delay t_0). We will also show that for relatively large filament radius r_0, t_0 becomes independent of r_0. Finally, we will expose an electric model that relates the filament electric resistance time evolution $R_{fil}(t)$ with the degradation status of the filament.

The Si-W solid solution phase diagram.

It is known that, regarding the silicidation process of the filaments, the domi-

nant diffusing species are silicon atoms [43]. The driving force of Si diffusion is the presence of a gradient in its chemical potential. Given that the time scale of the whole process is much larger than that of a precipitation step, the formed solid solution of Si and W is assumed to be always in quasi-static thermodynamic equilibrium. Hence, the W-Si binary phase diagram [58, 59] can be used to elucidate which stages will the central portion of the filament go through, when said filament is subject to a silicidation test like those described in section 2.2.1. Fig. 2.11 shows such W-Si phase diagram wherein continuous red lines indicate the path followed by a certain point located at the central portion of the filament where (initially) T=1850°C; red dots indicate the Si at.% values at which the different phases may precipitate and the red semi-continuous lines indicate the shift in Si at.% when a silicide phase precipitates.

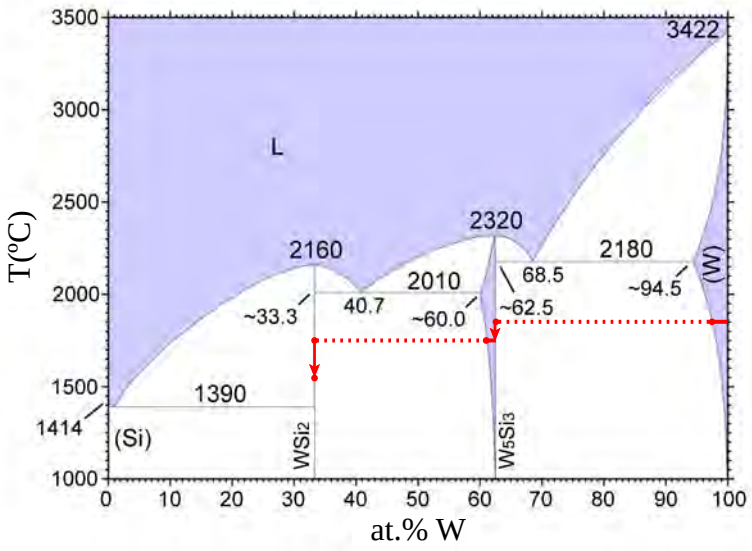

Figure 2.11: Si-W Binary phase diagram [58, 59]

We can see in Fig. 2.11 that during a silicidation test, a local region of the central portion of the filament goes through three different stages:

At the beginning of the deposition process, the concentration of Si atoms in the filament, $c(r,t)$, is zero (r refers to the radial coordinate). Once the deposition process starts, Si atoms begin to diffuse into the pure W bulk forming a Si-W solid solution. For any given temperature, there exists a solubility limit of Si atoms in pure W, c_{lim}, determined by the solvus lines of the W-Si phase diagram. In the

temperature range of our interest ($T \approx T_{fil}$), c_{lim} takes a value of few atomic % (around 10^{21} at/cm^3) and it decreases if T is lowered. As long as the solubility limit is not reached, no silicide phases will precipitate. The first stage is characterised by the dissolution of Si atoms in the W bulk without any silicide phase precipitation.

The solubility limit of Si in W will be firstly reached at the filament surface. At $t = t_0$, the surface Si concentration will be $c(r_0, t_0) = c_{lim}$. From this moment on, the local precipitation of the tungsten rich W_5Si_3 silicide phase takes place and the second stage of the filament central portion silicidation process begins. As long as the deposition process is not interrupted, the precipitation of W_5Si_3 takes place at deeper regions of the filament bulk. Hence, during this second stage it is formed an outer corona of W_5Si_3 and the local temperature decays, for instance, from 1850°C to approximately 1750°C due to the higher emissivity of W_5Si_3 in comparison to that of pure W.

For even longer silicidation tests, the filaments may enter into the third stage which stands for the precipitation of the silicon rich silicide phase WSi_2 in a W_5Si_3 matrix. This stage is analogous to the second one but now, we have to take into account the solubility limit of Si atoms in the W_5Si_3 silicide phase which is even lower than that in pure W. Once this solubility limit is reached, the local precipitation of WSi_2 begins and once more, it progressively advances towards the filament core. For the considered T_{fil} range, the emissivity of WSi_2 is always larger than the emissivity of W_5Si_3, so the filament temperature drops again, for instance, from 1750°C to approximately 1550°C. Finally, if $c(r_0, t)$ becomes larger than 66.7%, pure silicon films may grow on the filament surface. We suggest those readers who would like to know more about precipitation and nucleation processes in solid solutions, to check references [60, 61]

Diffusion model for the stage of Si atoms dissolution in the W filament

The SiH_4 and Si fluxes involved in the first stage of Si dissolution in a W filament are shown in Fig. 2.12.

$J^{in}_{SiH_4}$ is the number of SiH_4 molecules striking the W filament surface per unit area and time. If ξ_{SiH_4} is the catalytic dissociation probability of the SiH_4 molecules that strike the filament, the production rate of Si atoms is given by

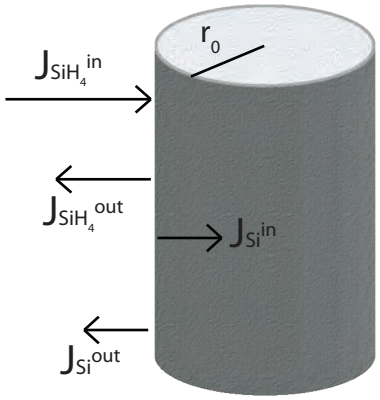

Figure 2.12: Schematic view of the fluxes involved in the dissolution stage of Si atoms in a W filament

$\xi_{SiH_4} J^{in}_{SiH_4}$. Hence, the flux[1] of SiH_4 molecules desorbing from the filament surface will be $J^{out}_{SiH_4} = (1 - \xi_{SiH_4}) J^{in}_{SiH_4}$. J^{out}_{Si} is the flux of produced Si atoms desorbing from the filament surface. On the other hand, the flux of Si atoms diffusing into the W bulk at the filament surface is J^{in}_{Si} and can be written as

$$J^{in}_{Si} = \xi_{SiH_4} J^{in}_{SiH_4} - J^{out}_{Si} = \alpha(c_0 - c(r_0, t)) \,, \tag{2.2}$$

where c_0 is the concentration of Si atoms at the filament surface for which the chemical equilibrium would be reached if there was not any precipitation of silicides, $c(r_0, t)$ is the Si concentration at the filament surface and α is a constant of proportionality. If we consider the Si-W system to be an ideal solid solution, Raoult's law states that in the chemical equilibrium, the Si vapour pressure of the solution must equal the Si gas pressure of the environment $p_{Si} = \xi_{SiH_4} p_{SiH_4}$. Then,

$$\xi_{SiH_4} p_{SiH_4} = p^*_{Si} c_0 \,, \tag{2.3}$$

[1] Please be aware that no vectorial notation of the flux $\vec{J}$ is used. For writing commodity reasons, the more simple notation, J, stands for the norm of the vector $\vec{J}$

where p_{SiH_4} is the silane gas partial pressure (2 Pa in our experiments) and p^*_{Si} is the vapour pressure of Si at $T = T_{fil}$. At temperatures in the range of T_{fil} ≈1850°C, p^*_{Si} ≈1 Pa [62] and ξ_{SiH_4} takes a value around 0.2 according to [63] or 0.4 [64]. Introducing these values in Eq. 2.3 one finds that, in any case, $c_0 \gg c_{lim}$. Clearly, we can not assure that the Si-W system behaves like an ideal solid solution but, even if applying Raoult's law constitutes a rough approximation, for a relatively large Si pressure in the environment, the equilibrium concentration c_0 should be much larger than c_{lim}. Hence, the limit $c_0 \gg c_{lim}$ would still hold. Given that, Eq. 2.2 can be written as

$$J^{in}_{Si} \approx \alpha c_0 \,, \tag{2.4}$$

thus meaning that the flux of Si atoms diffusing into the W filament can be considered constant. In this steady state approximation, the solution of the diffusion equation

$$\frac{\partial c(r,t)}{\partial t} - D\nabla^2 c(r,t) = 0 \,, \tag{2.5}$$

applied to the case of a cylinder of radius r_0, under the boundary condition of Eq. 2.4 and with the initial condition $c(r, t = 0) = 0 \ \forall r$, can be found in [65] (chapter 5.3.5). In our case, D is the diffusion coefficient of Si in W. Imposing that $c(r_0, t_0) = c_{lim}$ and applying the limits $r_0^2 \gg Dt$ and $r_0 \gg \lambda_1$ (where $\lambda_1 = \pi D c_{lim}/\alpha c_0$ is a characteristic length scale of the problem), one obtains the following expression for the time delay t_0

$$t_0 = \frac{c^2_{lim} D\pi}{\alpha^2 c_0^2} \,, \tag{2.6}$$

where t_0 does not depend on the filament radius. If we now define ξ_{des} as the desorption probability of a Si atom located at the filament surface, the flux of Si atoms diffusing into the W filament can be written as

$$J_{Si}^{in} = (1 - \xi_{des})\xi_{SiH_4} J_{SiH_4}^{in} \approx \alpha c_0 \, . \tag{2.7}$$

Mixing Eqs. 2.7 and 2.6 one gets

$$t_0 = \frac{c_{lim}^2 D\pi}{\left((1 - \xi_{des})\xi_{SiH_4} J_{SiH_4}^{in}\right)^2} \, . \tag{2.8}$$

More details of the calculations concerning this model are given in Appendix B.

Electric resistance model for the silicidation process of a finite W wire at high T_{fil}

We have already identified the two independent processes that contribute to the silicidation of W filaments during a-Si:H and/or μc-Si:H deposition in HWCVD at high T_{fil}.

On one hand, two WSi_2 fronts are rapidly formed at both filament cold ends. After a first transient period (15 min-20 min in our experiments), the WSi_2 fronts start expanding towards the middle of the filament with an almost constant propagation velocity v.

We have seen in section 2.2.2 that the electric resistance of a filament, R_{fil}, varies during its usage time. In order to interpret the obtained $R_{fil}(t)$ curves in our experiments (see Figs. 2.2 and 2.3), we propose a model wherein the aged filament is discretised into three different zones (I, II and III in Fig. 2.13) with different contributions to R_{fil}.

Zone I refers to the portion of filament that is covered by the advancing WSi_2 fronts from the filament cold ends. Zone III corresponds to the central portion of the filament and, finally, zone II covers the two transition gaps between zones I and III.

Regarding zone I, we must consider the case of two filament portions that have been fully transformed into WSi_2 with an extension that increases as the WSi_2 fronts advance towards the middle of the filament. The transition zone II is assumed to introduce a small and practically constant contribution to R_{fil}. With respect to Zone III, we will only discuss the case regarding the first two

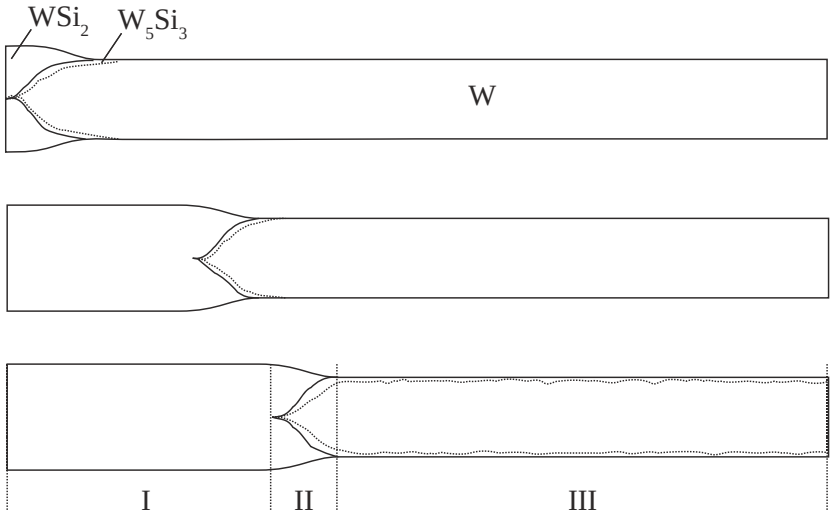

Figure 2.13: Schematic view of the different resistances considered in a W filament during its degradation process at $t \approx 0$ (top), $t \leq t_0$ (middle) and $t > t_0$ (bottom).

stages of the filament central portion silicidation process (Si atoms dissolution in W and W_5Si_3 precipitation). Then, the contribution of zone III to R_{fil} will be given by the parallel association of the remaining pure W filament core and the formed W_5Si_3 outer corona. The fraction of W atoms reacted into W_5Si_3 is zero for $t < t_0$ ($FR_{W_5Si_3}(t < t_0) = 0$). For simplicity, we will consider that, at a certain time $t \geq t_0$, $FR_{W_5Si_3}(t > t_0)$ takes a mean value between 0 and 1 for the whole extension of zone III. Taking all this into consideration, the time dependence of the filament electric resistance $R_{fil}(t)$ can be written as

$$R_{fil}(t) = 2C + 2R'_I vt + R'_{III}\left(L_{fil} - 2vt\right) , \tag{2.9}$$

where the first term $2C$ is a constant introduced by the contribution of the two transition zones II and the electric contact resistances, L_{fil} is the total filament length and v is the expansion velocity of the WSi_2 fronts. R'_I and R'_{III} are, respectively, the electric resistance per unit length of zone I and zone III. The details of the calculations concerning this model are given in Appendix C.

Given that in our experiments the electric current I is fixed, the local dissipa-

tion of power only depends on the local status of the silicidation process. Hence, we are able to evaluate the local temperature T as a function of FR_{WSi_x} for any point located in zone I or in zone III. We just have to find the solution of the equality between the local power (per unit length) dissipated by Joule effect and the local radiated power (per unit length).

The calculated temperatures of a 0.125 mm diameter tungsten filament which is gradually converted into W_5Si_3 (red line) or WSi_2 (black line) are plotted in Fig. 2.14 as a function of FR_{WSi_x}. The blue line in Fig. 2.14 gives the calculated temperature of a W_5Si_3 filament which is progressively transformed into WSi_2.

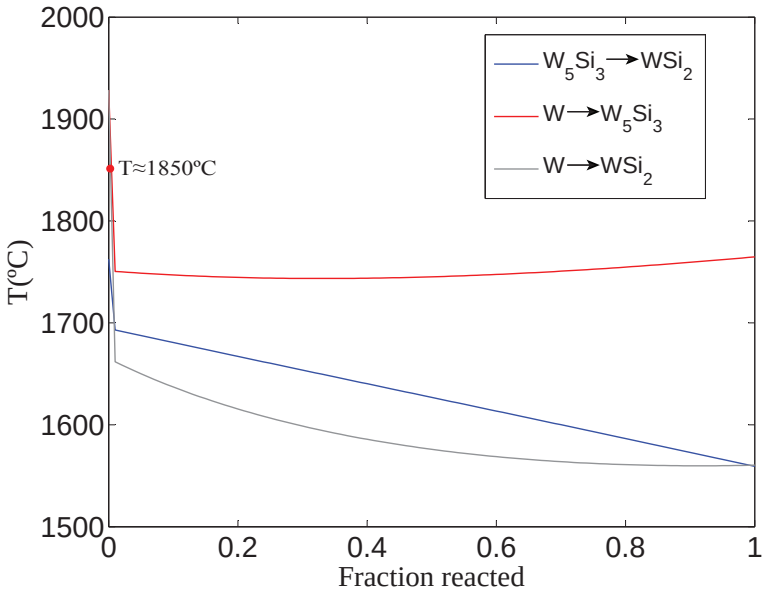

Figure 2.14: Temperature as a function of the fraction of W reacted for a 0.125 mm diameter W filament which is progressively converted into W_5Si_3 (red line) or WSi_2 (black line). The case of a filament that is converted from W_5Si_3 to WSi_2 is also represented (blue line). The electric current value is fixed to 1.63 A.

Once the temperature of a silicidated portion of filament has been calculated as a function of FR_{WSi_x}, the corresponding evaluation of its electric resistance per unit length R'_x is straightforward. The obtained results are plotted in Fig. 2.15.

According to our model, R'_I takes a constant value $R'_I = R'_{WSi_2}$ as zone I is considered a region wherein FR_{WSi_2}=1 is fixed. Regarding the portion of filament comprised in zone III, R'_{III} takes a constant value $R'_{III} = R'_W$ for $t < t_0$ as

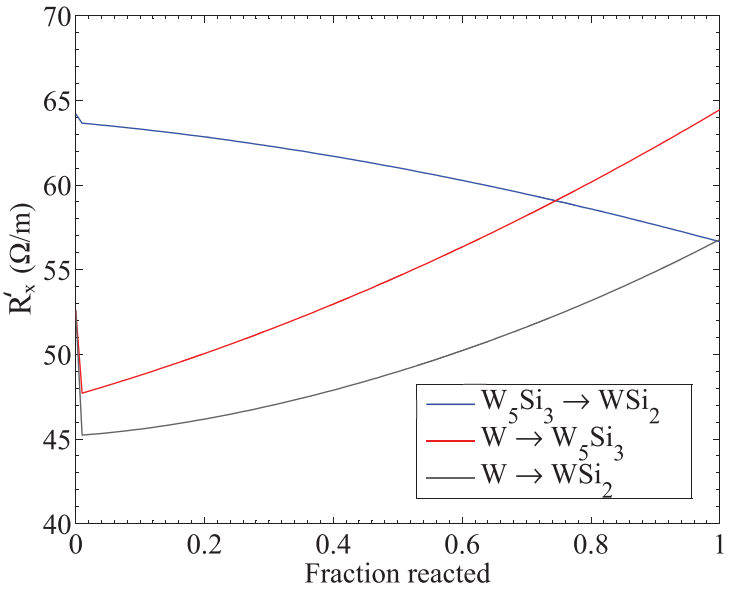

Figure 2.15: Electric resistance per unit length as a function of the fraction of W reacted for a 0.125 mm diameter W filament which is progressively converted into W_5Si_3 (red line) or WSi_2 (black line). The case of a filament that is converted from W_5Si_3 to WSi_2 is also represented (blue line).

$FR_{W_5Si_3}(t < t_0)$=0. However, for $t > t_0$, the precipitation of W_5Si_3 takes place and $FR_{W_5Si_3}$ progressively increases with time. Hence, $FR_{W_5Si_3}(t > t_0)$ becomes a time dependant parameter. This means that R'_{III} will also vary with time for $t > t_0$. To obtain the time dependence of $R'_{III}(t > t_0)$, we need to introduce the time dependence of $FR_{W_5Si_3}(t > t_0)$ which can be evaluated from the experimental data collected in the present study (see Fig. 2.10). As a first approximation, we will consider a linear dependence of $R'_{III}(t > t_0)$ with time (the quadratic term is only relevant for large times, that is to say for values of $FR_{W_5Si_3}$ pretty close to unity) like

$$R'_{III(t>t_0)} = A + B \cdot t \,. \tag{2.10}$$

Finally, we can now write the time derivative of $R_{fil}(t)$ for $t < t_0$ which reads

$$\frac{dR_{fil}}{dt}(t < t_0) = 2v(R'_{WSi_2} - R'_W) \,, \tag{2.11}$$

and for $t < t_0$ which reads

$$\frac{dR_{fil}}{dt}(t > t_0) = 2R'_{WSi_2}v - 2Av + BL_{fil}\,, \tag{2.12}$$

where R'_{WSi_2}=57± 3 Ω/m, R'_W=52±3 Ω/m, v=(4.0±0.3)·10^{-4} m/min, A=45±2 Ω/m, B=0.19±0.05 Ω/m·min and L_{fil}=0.3 m.

According to the proposed model, a linear regime should be observed in $R_{fil}(t)$ for $t < t_0$ with a slope within the range 0.005±0.005 Ω/min. Still, for $t > t_0$, $R_{fil}(t)$ also follows a linear regime but in this case, the corresponding slope is considerably higher, around 0.065±0.020 Ω/min.

2.2.5 Analysis of the results

In polycrystalline metals, diffusion of species may occur along the metal surface, the grain boundaries or through the crystal grains volume. Given that there is more open space for atoms motion at the metal surface or the grain boundaries, the mobility (and in consequence the diffusion coefficient) of Si atoms diffusing along these interfaces is much larger than those of Si atoms diffusing through the crystal volume [61]. Hence, the in-diffusion of Si atoms towards the filament core basically occurs through the W crystal grain boundaries. Let us imagine a W filament that is immersed in the initial Si atoms dissolution stage when the deposition process ends. The filament is then cooled down to room temperature and therefore, the solubility limit of Si in W becomes practically zero. Then, the solute Si atoms must precipitate, preferably at the grain boundaries of the W filament bulk. During the cooling of the filament, such grain-boundary precipitates may grow large in size and deplete the solute Si atoms from the areas adjacent to the crystals interfaces [60]. Fig. 2.16 shows a non-polished cross section of an aged W filament wherein such grain boundaries are clearly visible. The individual tungsten grains are much larger close to the filament surface and they tend to decrease in size towards the filament core giving an approximate idea of how deep have Si atoms diffused into the filament core.

The dissolution of Si atoms lasts until $t = t_0$ when the W rich W_5Si_3 silicide phase begins to precipitate. The expression of t_0, given by Eq. 2.8, states that

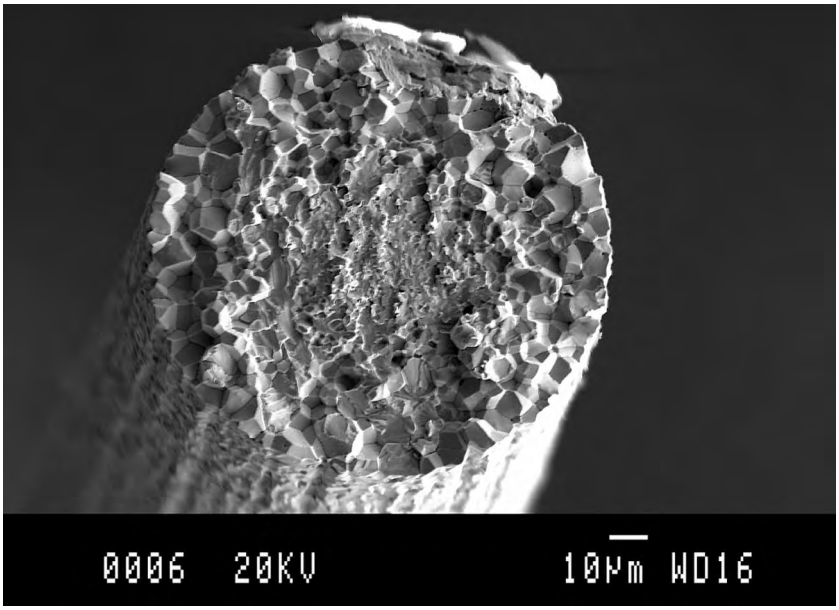

Figure 2.16: Cross sectional SEM image of and aged 0.125 mm diameter W filament at T_{fil} ≈1850°C and exposed to a SiH_4 atmosphere during 30 min

it is independent of the filament radius r_0. Eq. 2.8 only holds if $r_0 \gg \lambda_1$. The characteristic length scale λ_1 has been estimated to be in the range of few microns (see details in Appendix B) while W filaments used as catalysts in HWCVD usually have radius of several tenths or hundreds of microns (in our case, r_0=62.5 μm). Hence, in most practical situations, it is a reasonable approximation to apply the limit $r_0 \gg \lambda_1$. This means that in practice, increasing the filament radius does not have a considerably impact in the time delay t_0. On the other hand, the temperature dependence of t_0 is introduced in c_{lim}, D, ξ_{des} and ξ_{SiH_4}. D, ξ_{des} and ξ_{SiH_4} which are thermally activated parameters, proportional to $exp(\frac{-E_a^i}{kT})$ where k is the Boltzmann's constant and E_a^i is their corresponding activation energy (index i refers to the parameter i). According to Eq. 2.8, when either p_{SiH_4} is decreased and/or T_{fil} is increased, the time delay t_0 becomes larger. The evaluation of the time delay t_0 and its respective dependences is a crucial issue because, as we will see in section 2.3, it determines the initiation of the filament catalytic performance decay.

It should be noticed that in some HWCVD processes, like for instance in μc-Si:H deposition, the SiH_4 precursor gas is usually diluted with pure H_2. We realized

some preliminary tests in order to check which is the influence of hydrogen dilution in t_0. We found that if relatively high hydrogen dilutions are used, t_0 is considerably increased, thus meaning that the W_5Si_3 precipitation at the central portion of the filament retarded. Fig. 2.17 shows the $R_{fil}(t)$ curve of a silicidation test performed under deposition conditions compatible with μc-Si:H deposition. The chosen deposition parameters were exactly the same as those used in the tests performed under a pure SiH_4 atmosphere (see section 2.2.1). The only difference is that in this case, an additional H_2 flow of 128 sccm was introduced in the deposition chamber (H_2 dilution of 91.5 %), thus giving a total working pressure p=10 Pa.

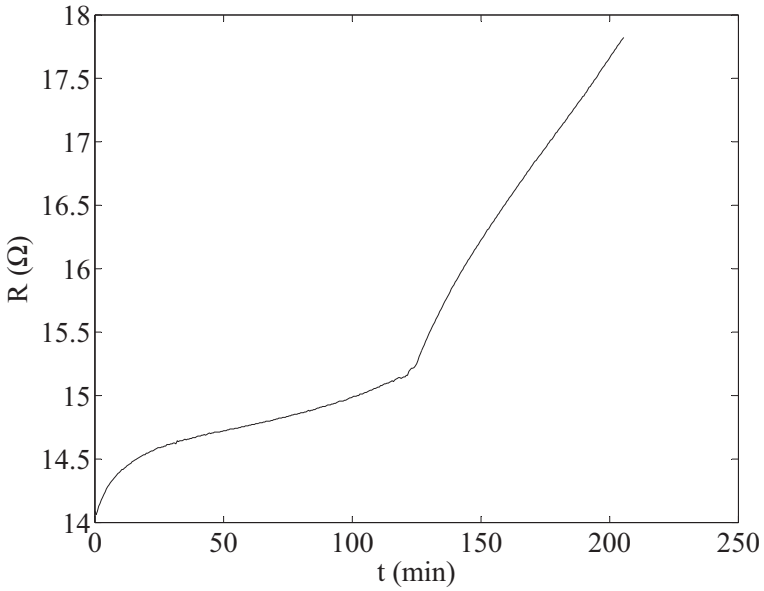

Figure 2.17: $R_{fil}(t)$ curve of a silicidation test performed with a 0.125 mm diameter W filament using a SiH_4 and H_2 mixture as precursor gas (T_{fil} ≈1850°C, I=1.63 A, p_{SiH_4}= 2 Pa, Φ_{SiH_4}= 12 sccm, Φ_{H_2}= 128 sccm).

For such deposition conditions, we found that t_0 ≈120 min, which is a twofold increase with respect to the maximum value of t_0 found in those tests wherein pure SiH_4 was the only precursor gas used. The explanation of such effect comes from the fact that when H_2 is added to the precursor gas mixture, a large amount of atomic hydrogen is created at the filament surface by catalytic dissociation of hydrogen molecules. The Si etching properties of atomic hydrogen [66] favour the

desorption of Si atoms from the filament surface. Then, the term $(1 - \xi_{des})$ in Eq. 2.8 becomes even smaller, thus leading to larger values of t_0. However, the slopes of $R_{fil}(t)$ for $t < t_0$ and $t > t_0$ (around 0.01 Ω/min and 0.06 Ω/min respectively) are similar to those obtained from the tests without any H_2 dilution. This suggests that hydrogen dilution has a remarkable influence on the nucleation process of silicides but not on the growth rate of the corresponding precipitates.

The precipitation of stable phases in a solid solution always entails a decrease in the free energy of the system. However, the nucleation process of such phases can be inhibited by additional energy contributions coming from surface tension effects and the strain introduced in the lattice. The additional surface and stress energy contributions are considerably lowered at lattice discontinuities such as dislocations or grain boundaries. This is the reason why the nucleation of precipitates, in a solid solution, often occurs at grain boundaries or dislocation clusters in the solid solvent (the W filament in our case). This type of nucleation process is known as heterogeneous nucleation. When the local nucleation of W_5Si_3 takes place, the area of the filament covered by the W_5Si_3 precipitate is subsequently expanded and the local temperature drops significantly as the result of an increase of the local filament emissivity. As a result, the local value of c_{lim} decays dramatically, thus promoting further precipitation of the W_5Si_3 phase in that region of the filament. This explains the large scattering of $FR_{W_5Si_3}$ values observed in aged filaments subject to silicidation tests with low effective silicidation times (see Fig. 2.10). However, such large differences in $FR_{W_5Si_3}$ along the filament length are less severe for those silicidation tests with larger accumulated SiH_4 exposure times because the surface diffusion of Si atoms is much faster than the in-diffusion of Si atoms in the filament volume and in consequence, the nucleation of the W_5Si_3 phase is rapidly expanded all over the entire filament surface.

Regarding the relation between the progress of the silicidation process of a filament with the monitoring of $R_{fil}(t)$ it has been exposed that R_{fil} follows, after a first transient period, a linear regime (see Figs. 2.2 and 2.8). According to the proposed electric model, for silane exposure times $t < t_0$, the slope, dR_{fil}/dt, of such linear regime is calculated to be about 0.005±0.005 Ω/min whereas for $t > t_0$ the predicted slope is 0.065±0.020 Ω/min. An abrupt change of dR_{fil}/dt should then be observed at $t \approx t_0$. On one hand, the experimental data of dR_{fil}/dt for $t > t_0$ shows good agreement with the values predicted by the proposed electric

model. On the other hand, it can not be stated that the linear trend of $R_{fil}(t)$ for $t < t_0$ predicted by the model holds in all cases. Certainly, the experimental data of $R_{fil}(t)$ for $t < t_0$ show several diverse trends. We assumed in our model that silicides formation was homogeneous all over the central region of the filament but, in fact, as it has been aforementioned, this process might not be neither stable nor homogeneous. Indeed, it can be seen in Fig. 2.9 that the experimental values of the time delay t_0 are widely spread and in some cases, t_0 might even be close to zero. Nevertheless, as we will show in section 2.3, if the tested filaments are subject to a pre-deposition annealing treatment, the time delay t_0 is stabilised and the evolution of $R_{fil}(t)$ is much more repeatable. In these latter experiments, the $R_{fil}(t)$ curves follow practically identical linear trends. The slope of such linear regime changes abruptly at $t = t_0$ from dR_{fil}/dt $\approx$0.01Ω/min to dR_{fil}/dt $\approx$0.08Ω/min, which is in good agreement with the prediction of the proposed model.

It is important to notice that the slope change observed at $t = t_0$ will be less intense if higher filament radius r_0 are used. Given that the filament cross section area is proportional to r_0^2, the time needed to reach a certain value of $FR_{W_5Si_3}$ at the central portion of the filament will also be proportionally increased. Then, if for instance 0.5 mm diameter filaments were used (instead of 0.125 mm diameter filaments as in our case), the parameter B in Eq. 2.12 would be 16 fold lower and the jump in dR_{fil}/dt at $t = t_0$ would be expected to be much less perceptible.

In the proposed electrical model, it was assumed that, after a first transient period, the transitions between the WSi_2 silicide fronts expanding from the cold ends and the central portion of the filament reach a stationary state covering an extension of few mm. In order to verify such assumption, we decided to directly check it in a real sample. A 0.125 mm W filament was aged by performing a silicidation test like those described in section 2.2.1. A portion of the tested filament was embedded into a resin matrix and afterwards it was mirror like polished. In this case, the sample was specially prepared to obtain a longitudinal cross section of the filament to observe the extension of such transition regions.

Fig. 2.18 shows an optical microscope image (proportions are not maintained) of this sample and a Raman spectroscopy signal mapping that allows identifying the WSi_2 and W_5Si_3 silicide phases, marked with blue and red colour respectively (the procedure is explained in section 2.2.2). The dark spots correspond to regions of pure W or alternatively, to regions wherein a large fluorescent signal from the

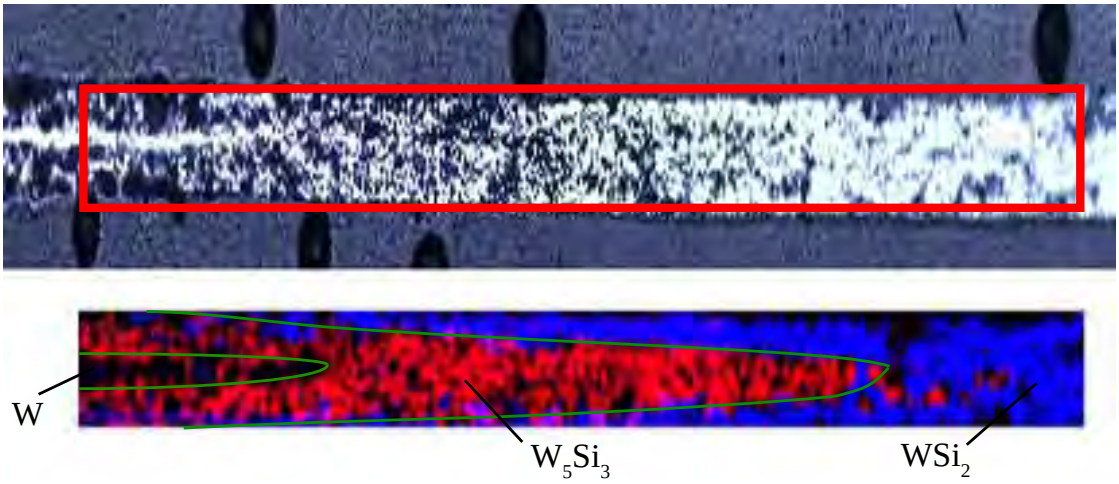

Figure 2.18: Longitudinal cross section optical image (top) and the corresponding Raman signal mappings (bottom) of an aged 0.125 mm diameter W filaments. Red and blue colours in the Raman signal mapping indicate the presence of W_5Si_3 and WSi_2 respectively. The red square corresponds to an area of 5 mm x 160 μm (not in real scale). The green lines correspond to the estimated W/W_5Si_3 and WSi_2/W_5Si_3 interfaces.

resin matrix was detected. The red square corresponds to the area scanned by means of Raman spectroscopy (5 mm x 160 μm). The green lines delimit the estimated W/W_5Si_3 and WSi_2/W_5Si_3 interfaces. By looking at Fig. 2.18 we can certify the assumption that the length of the transition zone II is only of the order of few mm, independently of the accumulated SiH_4 exposure time.

2.3 The tungsten silicidation process influence on the deposition rate

It is known that filament ageing entails a decrease in its catalytic performance and consequently, in the deposition rate r_d of the films [43–45]. However, it still has not been elucidated which is the relation between the progress of the silicidation process of the filaments and their catalytic performance. As long as the deposition conditions are kept the same during the HWCVD process, the changes in the current deposition rate of the film are a direct consequence of the filament catalytic performance decay. We will show how r_d evolves during the deposition

process of a-Si:H when a W filament is used at T_{fil} ≈1850°C. Afterwards, we will relate the decay of r_d with the initiation of the W_5Si_3 precipitation at the central portion of the filament. To do so, we will use the $R_{fil}(t)$ curves obtained during each silicidation test. The experimental set-up must guarantee that any contribution to r_d coming from the filament cold ends and from the WSi_2 expanding fronts is avoided. Furthermore, we have implemented a pre-deposition annealing treatment to the W filaments used in our experiments. With this procedure, the time evolution of R_{fil} becomes much more repeatable.

2.3.1 Experimental details

The silicidation tests performed for this study have been carried out under deposition conditions typical for a-Si:H deposition. Two 0.125 mm diameter W filaments were used in each test. For all the performed silicidation tests, the deposition parameters are the same as those described in section 2.2.1, i.e T_{fil} ≈1850°C, p_{SiH_4}=2 Pa, I=1.63 A, L_{fil}=30 cm. The only difference is that the silane flow is now doubled to SiH_4= 24 sccm, as in this case two filaments are being used instead of one. For our purposes, we need to keep as stable as possible other deposition parameters such as the substrate temperature and filament to substrate distance. Hence, the filament must be kept straight during the deposition process by means of a spring or a weight system. Doing so with only one filament as thin as 0.125 mm diameter turns out to be a complex matter as it easily breaks prematurely due to the imposed tensional force. An easier way to do this is using two filaments, instead of one, and connecting them in series by means of a copper microtube whose weight acts as the tensional force needed to keep the filaments straight.

Fig. 2.19 depicts schematically the experimental set-up mounted inside the HWCVD reactor for these experiments. There is an aluminium (Al) wheel with eight open windows that allow the deposition of the film on the substrate attached to the back of the Al wheel. Said wheel is able to rotate (the motion is transferred by means of a rotatory feed-through). Only one of the two used filaments (left one in Fig. 2.19) contributes to the deposition of the film on the substrate. The other filament is enclosed in a glass box. An Al plate is placed in front of the "contributing" filament. A hole practised in such Al plate permits the depositing on the substrate through a single open window once at a time. Furthermore, only a part

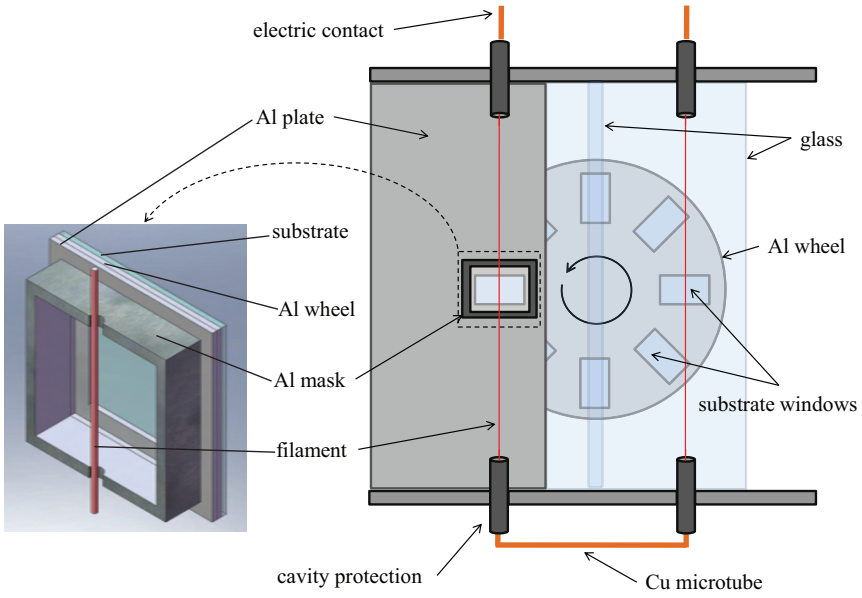

Figure 2.19: Experimental set-up mounted inside the HWCVD reactor for the study about the silicidation process influence on the deposition rate.

of the central portion of the filament does indeed contribute to the film deposition through the current substrate window because an Al mask shadows any contribution coming from the portions of filament close to the cold ends. The filaments cold ends have been covered with conventional cavity protection devices that considerably slow down the silicidation process at these locations (more details about such devices are given in Chapter 3). It is then avoided any contribution coming from the WSi_2 fronts formed at the filament cold ends to the film growth. During a single test, the current open window is periodically changed (up to eight times) by rotating the Al wheel. Then, it is possible to check how r_d evolves with time just by measuring the accumulated thickness of the film deposited through each open window during a certain period of time (the current open window through which the deposition of the film takes place, was changed every 15 min or 25 min, depending on the performed silicidation test). An halogen lamp, acting as a heater, was placed at the back of the Al wheel to assure that the substrate temperature

was kept constant during the whole deposition process. In this way, we can assure that the deposition rate evolution along a single test is only consequence of the progress of the silicidation process at the central portion of the filament. The filament to substrate distance was approximately d_{f-s} ≈1.5 cm. Thickness measurements were performed with an interferometric optical microscope (Sensofar, PLμ 2300). Prior to the beginning of each test, the filaments were pre-annealed in vacuum during 30 min at T_{fil} ≈1850°C. The filament electric resistance time evolution $R_{fil}(t)$ was monitored in all the silicidation tests that were carried out.

2.3.2 Results

Fig. 2.20 shows the $R_{fil}(t)$ curves of three performed silicidation tests and their corresponding $r_d(t)$ data points. The electric resistance data, R_{fil}, plotted in Fig. 2.20 corresponds to one of the two used filaments.

The three $R_{fil}(t)$ curves show a clear repeatability. All $R_{fil}(t)$ curves enter a linear regime and in all cases, an abrupt change of the slope takes place at t_0 ≈60 min. From what we have discussed in previous sections, we can determine that for all the performed silicidation tests the central portion of the filaments has entered, but not surpassed, the W_5Si_3 precipitation stage. Regarding the $r_d(t)$ curves, it can be seen that the initial deposition rate is maintained during the first minutes of deposition. However, for SiH_4 accumulated exposure times close to t_0, r_d drops significantly and is stabilised at about 65% of its initial value. Afterwards, r_d tends to increase for larger SiH_4 exposure times.

2.3.3 Discussion and analysis of the experimental results

The plot of the derivative of the obtained $R_{fil}(t)$ curves is shown in Fig. 2.21. Following the same procedure as in section 2.2.3 we can obtain the values of the time delay t_0 and the slopes of the two observed linear regimes. The obtained values of t_0 are within the range 60 ± 0.5 min. On the other hand, the slope of the first linear regime, related with the Si atoms dissolution stage, is around 0.01 Ω/min, whereas the slope of the second linear regime, related with the W_5Si_3 precipitation stage tends to a value around 0.08 Ω/min. Both values are in good agreement with the values expected from the electric model exposed in section

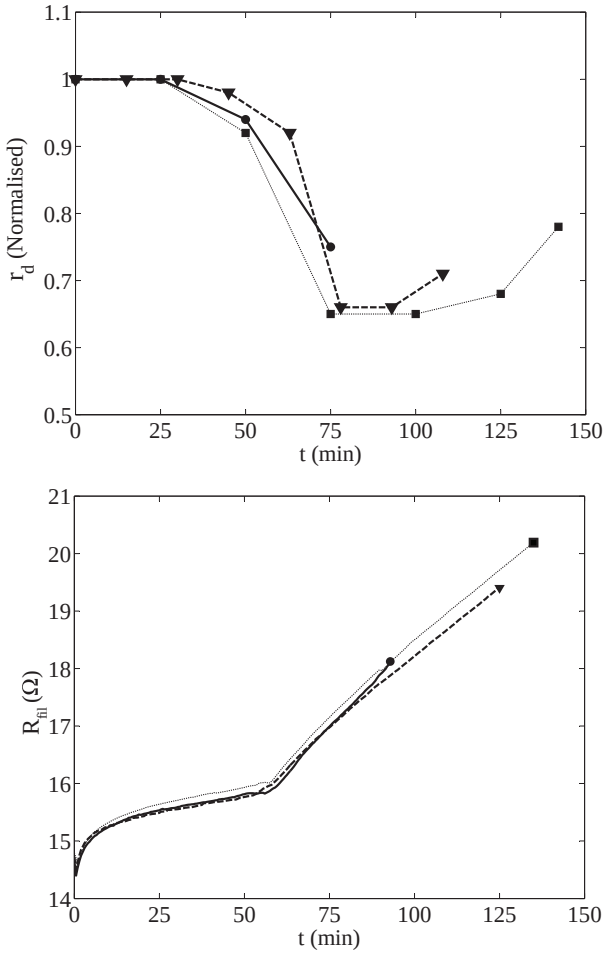

Figure 2.20: $R_{fil}(t)$ curves (bottom) of three silicidation tests and their corresponding $r_d(t)$ data points (top). The dotted, semi-continuous and continuous lines in $r_d(t)$ are just a guide to the eye. The accumulated deposition time of the corresponding $r_d(t)$ data points are 25 min (■, ●) and 15 min (▼).

2.2.4.

The repeatability of the $R_{fil}(t)$ curves, as well as the stabilised value of t_0 indicate that the nucleation of the W_5Si_3 silicide phase is much more homogeneous along the length of the central portion of the filament. Indeed, a pre-deposition annealing treatment at such high temperatures diminishes the density of structural defects at the filament surface, like grain boundaries and dislocations. It is known

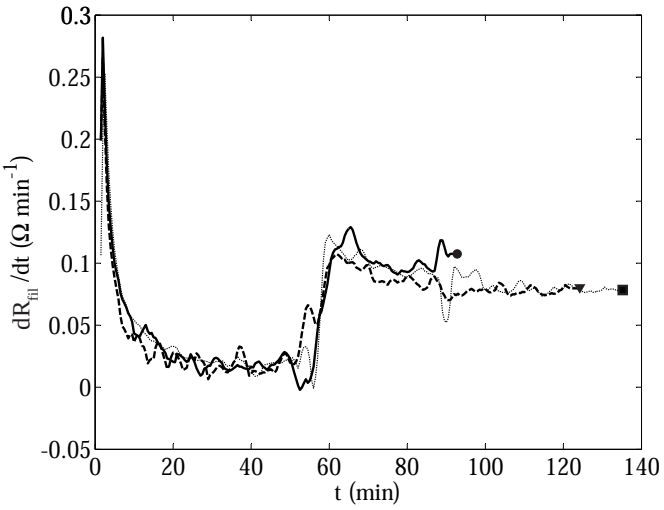

Figure 2.21: Calculated derivative of the $R_{fil}(t)$ curves of the three performed silicidation tests. All symbols correspond to those represented in Fig. 2.20

that if metals are subject to high temperature annealing treatments, the metal crystal grains tend to increase in size and aggregate, resulting in a lower density of such structural defects [61]. Even micro-fractures caused during the extrusion of the filament in its manufacturing process can be reduced by the self-diffusion of W atoms over the filament surface [43]. The consequence is that the process of heterogeneous nucleation becomes less probable and, statistically, the nucleation of W_5Si_3 is much more homogeneous. As a result, in the high T_{fil} regime, the silicidation process of pre-annealed W catalytic filaments becomes reasonably predictable and its progress can still be evaluated at real time by monitoring the evolution of the used filaments electric resistance.

Regarding the observed decay of the deposition rate r_d at accumulated SiH_4 exposure times close to t_0, it seems a reasonable assumption that it is a consequence of the precipitation of the W_5Si_3 silicide phase at the filament surface. The explanation of such effect is manifold. On one hand, as the filament surface is covered by W_5Si_3, there is less space left for W atoms that are responsible of the catalytic decomposition of the SiH_4 precursor gas molecules. On the other hand, the initial filament temperature is considerably reduced, for instance from T_{fil} ≈1850°C to T_{fil} ≈1750°C, thus reducing further the catalytic performance of the filament. It is also observed an increasing trend of r_d for larger SiH_4 exposure

times. We have already pointed out in previous sections that the filament radius is increased when silicide phases precipitate due to the difference between the molar density of W_5Si_3 (or WSi_2) and that of pure W. Hence, the observed increase of r_d is probably just a consequence of an increment of the catalytic filament surface.

2.4 Conclusions

In this chapter we have discussed the degradation of W filaments at high temperature used as catalysts in HWCVD for depositing silicon based materials such as a-Si:H using SiH_4 as gas precursor, or μc-Si:H (using mixtures of SiH_4 and H_2 as gas precursor). We have shown that the silicidation of W filaments consists of two independent processes. On one hand, the filament cold ends are rapidly silicidated and transformed into WSi_2. After a first transient period, these WSi_2 fronts advance towards the middle of the filament with an approximately constant velocity. On the other hand, the central portion of the filament is simultaneously affected by silicidation and three different stages have been identified: the initial Si atoms dissolution in W stage; the W_5Si_3 precipitation stage wherein a W_5Si_3 outer corona is formed and, finally, the WSi_2 precipitation stage wherein the previously formed W_5Si_3 outer corona is progressively transformed into WSi_2.

We have also shown that when the initial Si atoms dissolution stage ends, the catalytic performance decay of the filaments is initiated, resulting in a decrease of the deposition rate of about 35%. The duration of the Si atoms dissolution stage is what we call the time delay t_0. If it is desired to control and keep the deposition conditions constant during a HWCVD process, the *effective filaments lifetime* will be determined by t_0, and thus, the Si atoms dissolution becomes the only relevant stage. For a-Si:H deposition conditions, using 0.125 mm diameter W filaments as catalysts at $T_{fil} \approx$1850°C, the experimental results showed that t_0 may range from nearly zero min to 1h. Such scatter in the t_0 values is attributed to an heterogeneous nucleation of W_5Si_3. However, a pre-deposition annealing treatment of the filaments stabilises t_0 at 60 $\pm$ 0.5 min, thus meaning that the silicidation process becomes much more repeatable and, in consequence, predictable.

We have proposed an electric model that allows identifying which is the current stage of the silicidation process of a at real time by simply monitoring the slope of the filaments electric resistance. As a consequence of the initiation of W_5Si_3

precipitation at the central portion of the filament, an abrupt change in the electric resistance slope is observed at $t = t_0$. Such effect can be less evident if larger filament diameters are used.

A diffusion model for the evaluation of the time delay t_0 has also been exposed. The results show that, for filament diameters of several tens or hundreds of microns, t_0 is independent of the filament radius. Hence, in most practical situations, increasing the filament radius does not have a considerable impact on the effective filament lifetime. Eq. 2.8 shows that t_0 can only be considerably increased if the SiH_4 partial pressure is decreased and/or if the filament temperature is increased. However, such strategies for increasing t_0 may result in deposition conditions which are not any more suitable for device quality a-Si:H or μc-Si:H material deposition. Regarding μc-Si:H deposition, the hydrogen dilution of the SiH_4 precursor gas results in higher values of t_0, due to the Si etching properties of atomic hydrogen. Usual hydrogen dilutions of SiH_4 used for μc-Si:H deposition ($\Phi_{H_2}/(\Phi_{H_2} + \Phi_{SiH_4}) \approx 90\%$), result in a twofold increase of t_0. Even though, in this latter case, the effective filament lifetime would only take a modest value of approximately 2 h.

Taking all this into account, it is clear that regarding the HWCVD deposition of Si based materials, using W filaments as catalysts in the high T_{fil} >=1800°C regime and protecting the filament cold ends against silicidation, are not at all sufficient conditions to guarantee industrially relevant filament lifetimes. Even if the formation of the advancing WSi_2 fronts is avoided by implementing an efficient protection device at the filaments cold ends, the degradation of the central portion of the filaments seems to be inevitable for $t > t_0$.

Our conclusion is that in order to guarantee large operating times without maintenance interruptions of an eventual industrial HWCVD reactor for depositing Si based materials, an automatic filament replacement system should be developed and implemented in the deposition chamber. In addition, as we will see in Chapter 3, the current protection devices against silicidation for the filaments cold ends, have several limitations. In the following chapter, we will deal with the filaments protection issue and expose some technological solutions addressed to the development of an efficient protection device for the filaments cold ends and an automatic filament replacement mechanism.

Chapter 3

Filament Protection

3.1 Introduction

As it has been pointed out in Chapter 2, a tungsten filament used as catalyst in a HWCVD process for depositing either a-Si:H or μc-Si:H is affected by two different silicidation processes that limit its usage time: On one hand, two silicide fronts are rapidly formed at the filament cold ends and they progressively advances towards the middle of the filament. The portion of filament that is covered by these advancing silicide fronts is rapidly silicidated and is practically constituted of pure WSi_2 with the exception of two little transition regions that may be formed by both WSi_2 and W_5Si_3 silicide phases. This first process can be practically suppressed if the filament cold ends are effectively protected against silicidation. On the other hand, the central portion of filament, located between the two advancing silicide fronts, is also affected by silicidation. After a first stage, characterised by the Si atoms dissolution in the tungsten filament, the precipitation of the W_5Si_3 silicide phase takes place in the first place, followed by the precipitation of WSi_2. At said central portion of the filament, the core of the tungsten filament is progressively substituted by a W_5Si_3 outer layer which grows in depth and that is later transformed into WSi_2. For low filament temperatures (T_{fil} <1700°C), the precipitation of WSi_2 is almost immediate since the deposition process begins. In the high T_{fil} (>1800°C) regime, the solubility limit of Si in W is increased up to a few % and the desorption of Si atoms at the filament surface is enhanced. Then, using such high T_{fil} regime delays the formation of silicides in the central portion

of filament for a period of time (that we have called *the time delay* t_0). As we have shown in the previous chapter, t_0 is, in the best cases, of the order of few hours and it determines the *effective filament lifetime* as it corresponds to the initiation of the decay of the catalytic performance of the filament. Despite this, the term "filament lifetime" is usually referred to the accumulated usage time of a filament until its breakage occurs. However, this definition is, in our opinion, extremely inadequate as it ignores a crucial issue: the stability of the deposition conditions during the usage time of a filament. Up to now, most of the proposed solutions for the filament silicidation issue have been focused on preventing (delaying) the breakage of the used filaments. Some of these precedent works report filament lifetimes up to several hundreds of hours, ignoring the fact that, if the deposition conditions are desired to be kept stable, the *effective filament lifetime* may indeed be much minor:

A frequent approach to extend the filament lifetime is based on using high filament temperatures to delay as much as possible the degradation of the central region of the filament. In addition, a protection device must be developed to protect the filament cold ends from silicidation as the filament breakage usually occurs in these regions.

H. Matsumura and K. Ishibashi [67, 68] alternatively developed a protection mechanism which consists in introducing the filament cold ends into cavities with two open ends for the filament pass-through. A purge gas (N_2, H_2, Ar...) flow is then introduced into the cavities to avoid SiH_4 molecules reaching the filament cold ends. Professor H. Matsumura drafted a patent application of his invention (patent document WO/2007/148457). His group predicted that theoretical filament lifetimes of 680 hours could be achieved by implementing this solution for 0.5 mm diameter tungsten wires at T_{fil}=1850°C under a-Si:H thin film deposition conditions [51]. A particular limitation of this kind of protection device relies in the fact that the proposed purges are not as effective as expected (see details in section 3.3). Our group reported the protective limits of a simple cavity device without using any gas purge in [69].

Another protection mechanism to avoid the filament cold ends silicidation was developed by the group of professor B. Schroeder [47]. In the manuscript, a lifetime of 139 hours was reported for a 0.5 mm diameter tungsten filament at T_{fil}=2000°C under a-Si:H deposition conditions. In this paper, the protection mechanism was

not disclosed and, to our knowledge, the authors have not drafted any patent application related to the invention.

There exist many other attempts to solve the problem of filament silicidation. For instance, carburization of tungsten filaments has been tested as a possible protective method showing that filament silicidation is relatively slowed down [70]. However, the catalytic performance of carburized filaments is considerably lower than in the case of using pure metal filaments. The same idea holds for the solution reported by Martin et al wherein the catalytic filament is replaced by a tantalum carbide (TaC) rod [71]. In this case, the reported experimental results are limited to deposition times of only 2 hours. Regarding these latter solutions, the higher emissivity of carburized filaments results in larger radiated power which may become unsustainable. Moreover, the problem of film contamination by carbon impurities is not dealt and the deposited material quality is not reported. A different solution proposed to avoid the filament silicidation process is based on the use of radio-frequency alternate current (RF, 13.5 MHz) instead of direct current (DC) to heat the filament [48]. In this case, the underlying idea is that the skin effect of RF current reduces silicon deposition and in-diffusion at the filament surface. By using this method, the filament lifetime extension is reported to be increased by less than twofold.

As a remark, it is interesting to point out that for tantalum filaments used as catalysers (instead of tungsten filaments), certain filament treatments may extend their lifetime. Examples of such filaments treatments are those suggested by the groups of professors D. Knoesen and R.E.I. Schropp which consist in pre- and post-deposition filament thermal annealings in H_2 atmosphere and vacuum respectively. The work published by Knoesen et al [49] reports a lifetime of 322 hours for 0.5 mm diameter tantalum filaments at T_{fil}=1600°C. The filament was annealed before and after each deposition run during 5 minutes minimum. The deposition conditions were not specified. On the other hand, the study made by C.H.M van der Werf et al [46] does not report any value of filament lifetime. However, it is demonstrated that for a 0.5 mm diameter tantalum wire at T_{fil}=1750°C under μcSi:H deposition conditions that has accumulated a total deposition time of 8 hours, the silicidation process related to the central region of the filament is reversible (but not the one related to the cold ends). The filament treatment consists in a 30 min vacuum annealing at T_{fil}=2050°C after each deposition run and a final vacuum annealing

of 4 hours at T_{fil}=2100-2200°C when the aged filament has already been working for a total deposition time of 8 hours. It seems that there are no references in the literature that report such results for these filament treatment methods when applied to tungsten filament catalysers.

To summarize, for a-Si:H or μcSi:H deposition processes, the filament breakage occurs, in the best cases, after a few hundreds of hours if certain protection devices [47, 67, 68] or filament treatments are implemented [49]. However, the reported protective mechanisms usually limit the hot wire configuration or alter the process deposition conditions while the filaments pre- and post-deposition treatments are highly time consuming. Moreover, these solutions do not guarantee that, during the respective reported filament lifetimes, the deposited material quality and the filament catalytic performance remain unaltered. This last aspect is crucial in the field of solar cells. Hence, a more suitable definition for the filament lifetime should be "*the total operating time whenever the catalytic performance of the filament assures the reproducibility of the required film quality levels*".

Developing an effective protection device for the filament cold ends is mandatory but it is not the unique requisite that must be fulfilled in order to find a definitive solution for the problem of the filament ageing in HWCVD. As we have exposed in Chapter 2, the silicidation of the central region of the filament is inevitable. Thus, a mechanism to replace this portion of filament, once its catalytic performance is unsatisfactory, must also be developed. We decided to focus our research in developing a technologically feasible filament replacement system that allows implementing effective protection devices that prevent the silicidation of the filament cold ends.

This chapter deals with the work carried out during this thesis to design, build and test our own developed cold ends protection device and filament replacement mechanism. For the design of the filament cold ends protection device, two different strategies have been explored: the first one consists in increasing the temperature of the coldest portions of filament which are exposed to SiH_4. This can be achieved by decoupling the electric and thermal contacts of the filament as explained in section 3.2. The second strategy explores the possibility of decreasing the SiH_4 partial pressure at the regions wherein the filament cold ends are located. This can be achieved by introducing the filament cold ends into a cavity as explained in sections 3.3 and 3.4. Furthermore, the proposed protection devices were designed

in such a way to be compatible with an automatic filament replacement mechanism that has been developed in our laboratory, the details of which are given in section 3.5. As far as we know, up to now it has not been reported the construction of any HWCVD reactor implementing any kind of automatic filament replacement mechanism or similar. There exist however, a few patent application documents wherein there are proposed certain technological solutions for constructing such a HWCVD apparatus. Among them, the most relevant are patent applications JP7254566-A, JP2008140945-A and US2008/0095937-A1.

The first patent application JP7254566-A discloses a HWCVD apparatus wherein a catalytic filament is supported between a sending object and a coiling object. The filament electric contacts are located between these two objects. In the filament replacement process, a portion of catalytic filament can be sent from the sending object and wound around the coiling object. The sending and the coiling objects can be, for instance, two reels. The motion is transferred to the mechanism by the action of an electrical motor coupled to the axis of one of both reels. However, it must be taken into account that during the heating of the catalytic filament, this last is subject to thermal expansion. To avoid the bending of the filament due to its lengthening, it is necessary to implement a mechanism which keeps tense the catalytic filament during all operating situations. This point is particularly important to guarantee a good film homogeneity and the repeatability of the HWCVD process. This would be a critical issue for all large area deposition systems implementing a continuous or semi-continuous replacement of the catalytic filaments. A solution to this problem is based on the utilisation of an additional electrical motor for controlling the torque exerted over the two reels wherein the filament is wound. However, this solution can not be applied to large systems with a catalytic filament net composed of tens or hundreds of filaments, because it would be necessary to use tens or hundreds of electrical motors, with their corresponding vacuum rotational feed-troughs to transmit the motion to the reels, what is impracticable. In the patent application document JP2008140945-A, it is disclosed a HWCVD apparatus and a catalytic filament replacement method, which tries to overcome this problem by creating the catalytic filament net using a single filament covering a zigzag path around rollers placed along two distanced parallel lines. Still, this solution is also impracticable for other different reasons. Firstly, because the catalytic filament becomes brittle during its degradation pro-

cess and the zigzag path can not be adequately dense without risking its rupture. Secondly, the usage of many rolls along a single filament introduces accumulative frictions which alter the tension exerted on the filament. Thirdly, the replacement velocity of the catalytic filament may become unsustainably high due to the fact that the filament portions, which compose the catalytic filament net, are changed sequentially, one after the other.

Therefore, there is a need to provide a HWCVD apparatus able to change the different catalytic filaments in parallel using a minimal number of motors, but keeping each catalytic filament tense during all operating situations. Technological solutions for the construction of such a HWCVD apparatus will be exposed in section 3.5. The experimental results obtained using a first prototype of our own developed filament replacement mechanism will also be presented.

3.2 Cold ends protection using a ceramic cover device

The idea underlying this strategy is that the electrical contact, which is usually at a temperature of a few hundred degrees, is decoupled from the thermal contact, that is to say, a thermal contact body is introduced just after the electric contact surrounding the filament cold ends. In this way, it is possible to cover the filament portion wherein the local temperature $T(x)$ is lower than the local filament temperature at the extreme ($x = L_c$) of the thermal contact body ($T(x) < T(L_c)$). The thermal contact body should be designed in order to achieve the highest possible value of $T(L_c)$. If $T(L_c) \approx$1750°C or larger, the portion of filament wherein silicidation is most aggressive (where the local temperature is around 1650°C [51]) is covered by the thermal contact body meaning that this critical region would not be exposed to SiH_4 gas molecules, thus being protected from silicidation. The thermal contact body was designed like a ceramic thin tube. To facilitate the manipulation of this protection device, it was necessary to enlarge the diameter of the ceramic tube along the first millimetres. This first section of the ceramic tube constitutes a large thermal mass with high radiation losses due to its larger diameter. Thus, the point where both thicker and thinner ceramic tubes are joined can be considered as the effective thermal contact of the system, located at $x = 0$ with

a temperature $T(0)$. The thin ceramic tube section, which extends from $x = 0$ to $x = L_c$ is enclosed by a hollow body that creates a furnace effect, what minimizes the radiation energy losses thus raising further the temperature $T(L_c)$. The whole assembly is schematically depicted in Fig. 3.1. The material chosen to build the thermal contact body and the furnace was alumina, Al_2O_3, because of its high chemical stability, high working temperature compatibility, high electric resistivity and market availability (Al23 alumina from FRIATEC-DEGUSSIT company).

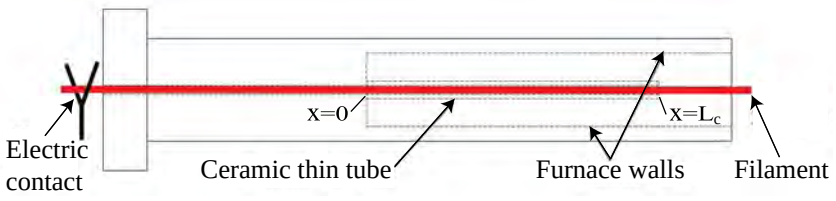

Figure 3.1: Schematic view of the ceramic cover device surrounding a filament cold end.

3.2.1 Calculation of the cold end temperature

To calculate the local temperature profile $T(x)$ at the filament cold ends, we need to solve the diffusion equation that is derived from applying Fourier's law. The gradient of the local heat flow equals the difference between the local power (per unit length) dissipated by Joule effect and the local power (per unit length) irradiated following Stefan-Boltzmann's law. One gets the following diffusion equation (the details on the following calculations are given in Appendix D)

$$\frac{d^2T}{d^2x} = c_1\,T(x)^4 - c_2\,T(x)^2 - c_3\,T(x) - c_4\,, \tag{3.1}$$

where the coefficients c_1, c_2, c_3, c_4 take different expressions for $0 \leq x \leq L_c$ and $x \geq L_c$ as the thin ceramic tube only covers the filament portion between $x = 0$ and $x = L_c$. Eq. 3.1 must be solved imposing the corresponding continuity conditions for the temperature and the heat flow at $x = L_c$. The boundary conditions are given by the thermal contact temperature $T(x = 0) = T(0)$ and the asymptotic filament temperature $T(x \gg L_c) = T_{fil}$.

Let us now consider the effect of enclosing the thin ceramic tube in a hollow body acting as a furnace. A percentage of the power radiated by the ceramic thin tube will be reflected back from the inner furnace walls and partially reabsorbed by the thin ceramic tube. It can be seen that the furnace effect is equivalent to renormalise the emissivity of the ceramic thin tube, e_c, as follows

$$e'_c = e_c \frac{(1-\mathcal{R})}{1-\mathcal{R}(1-e_c)} \,, \tag{3.2}$$

what in fact corresponds to a renormalisation of the power irradiated by the ceramic thin tube, being $\mathcal{R}$ the reflectance of the inner furnace walls. If the furnace is fabricated with the same material as the ceramic thin tube, then $\mathcal{R} = 1 - e_c$. The material chosen for fabricating the device was alumina Al23 from FRIATEC-DEGUSSIT. In the data sheet given by the company, the emissivity of Al23 is only given for 1000°C (e_{Al23}(1000°C=0.21). Using this emissivity value as a first approximation, one finds that the renormalised emissivity of the ceramic thin tube inside a furnace would be $e'_c \approx$0.12. The pictures shown in Fig. 3.2 were taken during a preliminary test of the protection device and show how the furnace effect helps to increase the temperature $T(L_c)$ at the end of the thin ceramic tube. The calculated $T(x)$ profile for different tungsten filaments, with their cold ends covered with a Al23 thin tube and enclosed in a Al23 furnace, are shown in Fig. 3.3. The temperature at the end of the ceramic thin tube is in all cases $T(L_c) \approx$1500-1600°C except for the 0.5 mm diameter filament where it reaches $T(L_c) \approx$1830°C.

3.2.2 Experimental test of the ceramic cover protection

In our HWCVD reactor, we usually use thin tungsten filaments with diameters in the range of 0.1 to 0.2 mm for depositing either a-Si:H or μc-Si:H. Hence, we decided to make some preliminary tests using 0.2 mm filaments in order to check the real performance of the protection device and also to detect any unexpected drawback. The tests were performed under regular μc-Si:H deposition conditions used in our HWCVD reactor ($T_{fil} \approx$ 1850°C, p=10 Pa, Φ_{tot}=300 sccm and a silane concentration $SC = \Phi_{SiH_4}/(\Phi_{SiH_4}+\Phi_{H_2})$= 8.5 %). Fig. 3.4 shows two pictures of two filament assemblies taken during a single experiment in which two filaments of 0.2 mm diameter and 20 cm length were used. A spring system keeps the filaments

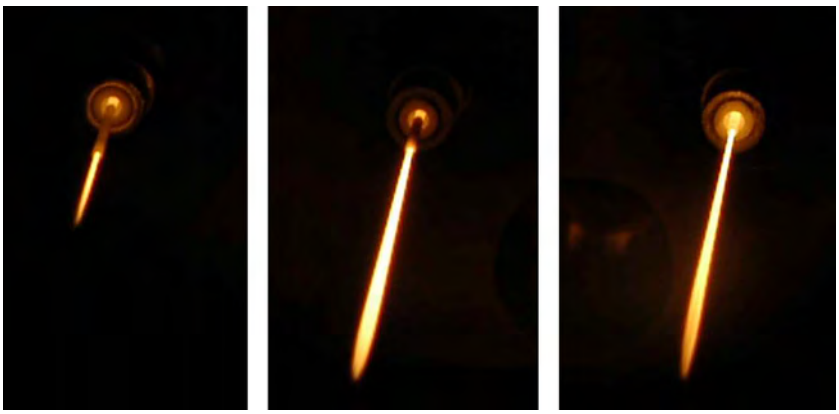

Figure 3.2: Three pictures of 0.2 mm diameter filaments, heated at a temperature of 1850°C, with the cold ends covered by a thin ceramic tube. The temperature differences at the end of the thin ceramic tube when it is either enclosed in a furnace (right picture) or not (left and middle pictures) are clearly identifiable.

straight despite of thermal expansion by applying a constant tension of about 1 N. One of the filaments was assembled with a ceramic cover device (see Fig. 3.1) protecting one of its cold ends. The other filament had no protection at all. The test lasted for 2h and 30 min.

3.2.3 Results and discussion

The cold ends of either an unprotected and a protected filament after one single test (see Fig. 3.4) were observed by means of SEM. Chemical analysis of the different regions observed was performed by means of EDX. Fig. 3.5 shows the SEM cross section images of both filament cold ends as well as the chemical composition of the different regions observed. It can be seen that the benefits of the tested protection device are quite poor. The filament cold end that was covered by the protection device seems to be slightly less affected by silicidation but it still presents a large amount of cracks. Si-rich silicide WSi_2 formation is evident at both cold ends. This poor protective performance of the tested device was already expected as the simulation of $T(x)$ showed that the temperature at the end of the thin ceramic tube would be around $T(L_c)$=1580°C. In addition, during the test we could observe an unpredicted effect that is clearly detrimental for the device performance. We are referring to the silicon deposition that takes place on the

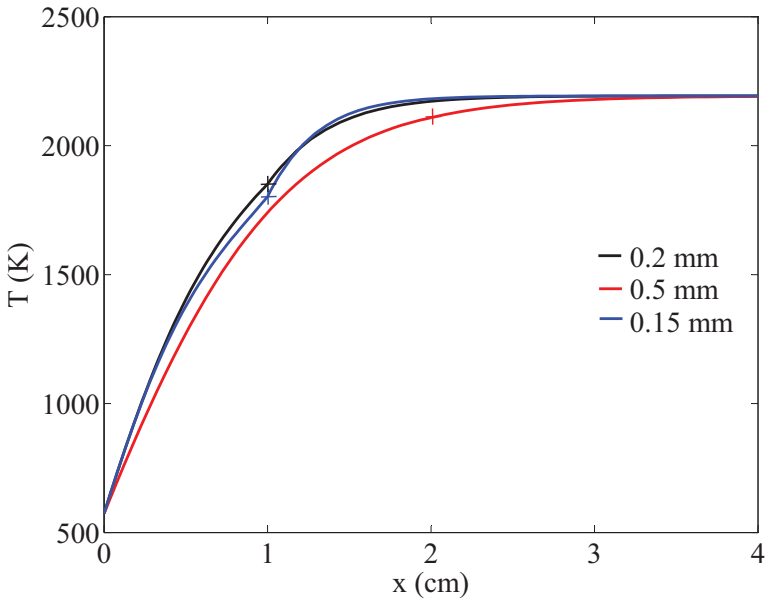

Figure 3.3: Temperature profile for three wires of different diameter covered with a Al23 ceramic thin tube which is located inside an optical furnace. The renormalised thin tube emissivity is set to e'_c =0.12. The thermal contact temperature and the asymptotic filament temperature are respectively set to $T(0)$=300°C and T_{fil}=1850°C. The ceramic thin tube dimensions are r_{out}=0.25 mm (external radius), r_{in}=0.1 mm (inner radius) and L_c=10 mm (length) for the 0.15 mm diameter filament, r_{out}=0.3 mm, r_{in}=0.15 mm and L_c=10 mm for the 0.2 mm diameter filament and r_{out}=0.5 mm, r_{in}=0.3 mm and L_c=20 mm for the 0.5 mm diameter filament. The crosses indicate the point $x = L_c$ in each case.

furnace inner walls (see Fig. 3.4) and, as it was latter observed by SEM analysis, on the surface of the thin ceramic tube. This silicon layer growth is evident just after a few minutes from the beginning of the deposition process and its immediate effect consists in increasing the radiating emissivity from $e_{Al23} \approx 0.21$ to $e_{Si} \approx 0.6$, so the temperature $T(L_c)$ drops dramatically. Hence, we can conclude that even if the initial value of $T(L_c)$ was greater than 1750°C, this situation would only last for a few minutes until the emissivity of the radiating body becomes that of the deposited silicon film. Furthermore, it has been noticed that the silicon layer deposited at end of the thin ceramic tube can grow thick enough to bond the thin ceramic tube with the tungsten filament. This eventual bonding entails that the filament is not able to move freely through the ceramic thin tube any more, what

Figure 3.4: Close up of the two tested filaments cold ends (left filament: unprotected, right filament: protected). The image to the left was taken at the beginning of the test. The right image was taken after a few minutes of initiating the test and it can be observed that a thick silicon film has already been deposited at the furnace walls.

constitutes an insurmountable obstacle for assembling this protection device to an automatic filament replacement mechanism.

3.2.4 Conclusions

It has been seen that for filament diameters lower than 0.5 mm, the maximum temperature reachable at the end of the thin ceramic tube is still much lower than 1750°C. In addition even in the case of using a 0.5 mm (or even larger) diameter filament, the deposition of Si over the ceramic surface would rapidly decrease the temperature far below 1750°C. This means that the protection against silicidation becomes absent or marginal. To avoid this undesired Si deposition, a completely different device should be developed. Finally, the eventual bonding between the thin ceramic tube and the tungsten filament disallows the possibility of the simultaneous implementation of an automatic filament replacement mechanism.

Taking all these considerations into account, it was decided to discard this strategy for the protection of the cold ends of the filaments and focus our efforts in developing a different protection device based on decreasing the silane partial pressure at the regions wherein the filament cold ends are located.

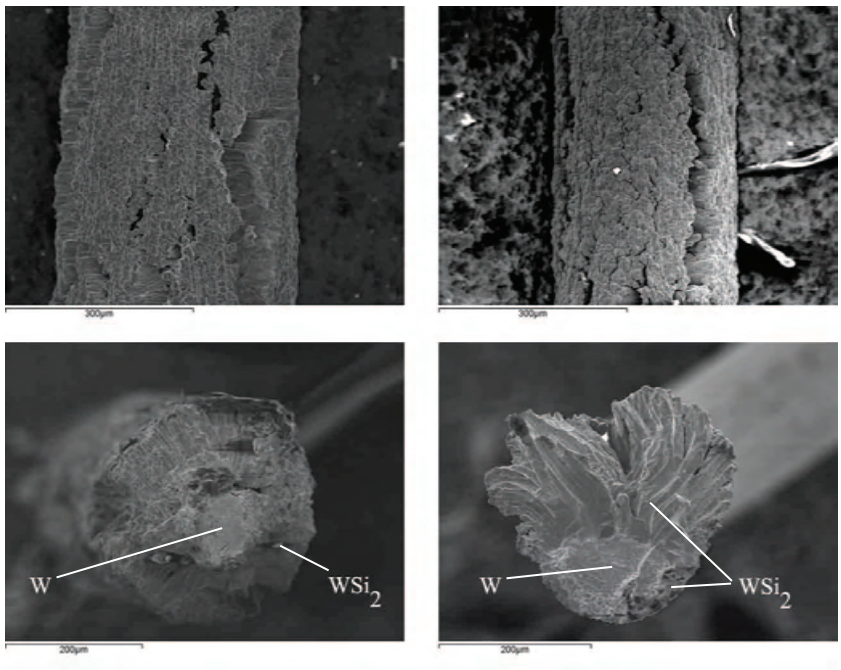

Figure 3.5: SEM images of an unprotected filament cold end (top left) and a protected filament cold end (top right) and their respective cross sections (bottom left and bottom right). Chemical compositions were obtained by EDX analysis. The test deposition conditions were $T_{fil} \approx 1850$°C, p=10 Pa, Φ_{tot}=300 sccm and $SC = \Phi_{SiH_4}/(\Phi_{SiH_4}+\Phi_{H_2})$= 8.5 %. The test lasted for 2 h and 30 min.

3.3 Cold ends protection using a simple cavity

This kind of protection mechanism is very simple and can be easily implemented in a HWCVD reactor. It was alternatively proposed in year 2001 by H. Matsumura [67] and K. Ishibashi [68]. The idea consists in introducing the filament cold ends into a cavity with an open end for the filament pass through and, at the same time, filling the cavity with a purge of H_2, N_2 or an inert gas like for instance Ar. During a deposition process, the purge gas flow exits the cavity through the same hole through which the filament is passing. The underlying assumption is that a large amount of collisions between the purge gas molecules and the precursor gas (SiH_4) molecules will take place, thus preventing silane from entering into the cavity where the filament cold ends are located. From the kinetic gas theory [72], it can be seen that the molecular mean free path λ_f is given by

$$\lambda_f = \frac{kT}{\sqrt{2}\pi d_{mol}^2 p}\,, \tag{3.3}$$

where k is the Boltzmann constant, d_{mol} is the molecule diameter and p is the gas pressure. For a gas temperature T of few hundred degrees (i.e the temperature of the cavity inner walls) and typical working pressures of 1 to 10 Pa used in HWCVD processes for a-Si:H or μc-Si:H deposition, the mean free path is of the order of few millimetres. This means that a silane molecule entering the cavity has a great probability of suffering one collision with a purge gas molecule within the first millimetres of the cavity length. Of course, this does not suppress the diffusion of silane molecules into the cavity. For a cavity length of few cm, high flows, around 50 sccm [51], of an inert purge gas like N_2 must be used to achieve a substantial reduction of the silane partial pressure at the filament cold ends. However, this strategy has the inconvenient of promoting heat conduction losses from the filament to the gas phase [73, 74], specially at the cavity entrance. In consequence, the local temperature of the filament portion near the cavity entrance drops considerably and another undesired cold region of the filament is created in this location. The problem is then shifted from the filament cold end towards the portion of filament close to the cavity entrance. Despite this, even if no purge gas is used, a simple cavity device still produces a protective effect for the filament cold ends [33]: Although silane molecules may enter into the cavity, they are as well dissociated by the catalytic filament. This leads to a decrease of SiH_4 concentration along the cavity axis which is the most relevant reason why the filament cold ends are partially prevented from silicidation when such protection devices are used. In this section, it will be discussed the performance and limits of a simple cavity device, without any kind of purge, for protecting the filament cold ends.

3.3.1 Model of a simple cavity

The working mechanism of a simple cavity like the one depicted in Fig. 3.6 can be explained in terms of the linear SiH_4 concentration $n_{SiH_4}(x)$ along the cavity axis. Silane molecules that enter into the cavity are catalytically dissociated by the tungsten filament at a rate κ_{dis}. If the cavity length L is much bigger than its inner radius ($L \gg r_{cav}$), the problem can be treated as a one dimensional diffusion

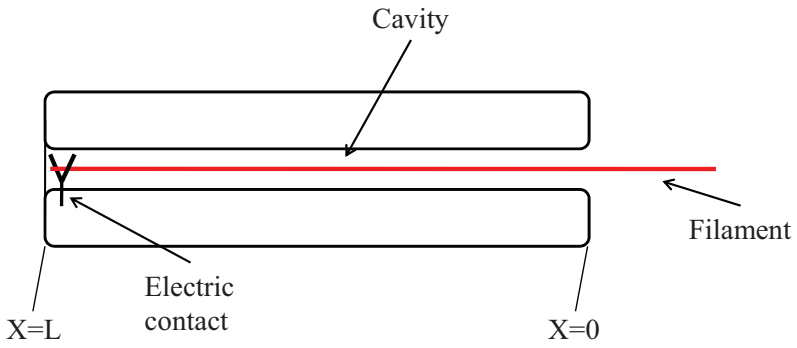

Figure 3.6: Schematic view of a simple cavity for one filament cold end protection.

process. The one dimensional diffusion equation reads

$$D\frac{d^2 n_{SiH_4}(x)}{dx^2} - \kappa_{dis} \cdot n_{SiH_4}(x) = 0\,, \tag{3.4}$$

where D is the diffusion coefficient of SiH_4 inside the cavity. The boundary conditions are: $n_{SiH_4}(0)$=$n^{out}_{SiH_4}$, being $n^{out}_{SiH_4}$ the silane concentration outside the cavity, (i.e the cavity has an open end at $x = 0$) and $dn(L)/dx$=0 (i.e the cavity is closed at $x = L$). The solution of $n_{SiH_4}(x)$ takes the form of a hyperbolic cosine curve as follows

$$\frac{n_{SiH_4}(x)}{n^{out}_{SiH_4}} = \frac{cosh\left(\frac{x-L}{\lambda_2}\right)}{cosh\left(\frac{L}{\lambda_2}\right)}\,, \tag{3.5}$$

with

$$\lambda_2 = \sqrt{\frac{D}{\kappa_{dis}}}\,. \tag{3.6}$$

Let us now consider the thickness profile $d(x)$ of the silicon layer deposited on the inner cavity walls during a certain deposition time t. It is a reasonable approximation to suppose that the thickness profile $d(x)$ is directly proportional to the amount of silane dissociated by the filament at the same position $t \cdot \kappa_{dis} \cdot n(x)$. Then, $d(x)/d_0$ does also take the form of Eq. 3.5.

3.3.2 Experimental tests of a simple cavity protection device

All the experiments were carried out in our single chamber HWCVD reactor using a single filament hot wire assembly. A spring system allows keeping a tungsten filament of 0.2 mm of diameter straight despite of thermal expansion by exerting a constant tension of about 1 N.

A first group of experiments were prepared for the validation of the model of a simple cavity protection device exposed in the previous section: Two stainless steel cylindrical cavities with an internal radius r_{cav}=2 mm and a length L_{cav}=90 mm were assembled at both cold ends of the tested 0.2 mm diameter filament. In order to measure the thickness profiles of the Si film deposited on the cavity inner walls, one of the wire holders was modified in such a way to be able to fix in there a glass substrate. The thickness profiles along the axis of the cavity were measured with a profilometer. Filaments of 0.2 mm diameter with the same length as the cavity (L_{fil}=90 mm) were used for these tests. However, preliminary tests using longer filaments did not show any substantial difference in the thickness profiles of the deposited Si layers. Two different deposition conditions were chosen: Normal pressure deposition (Φ_{SiH_4}=10 sccm, Φ_{H_2}=90 sccm, p=5 Pa, $p_{SiH_4} \approx p \cdot \Phi_{SiH_4}/(\Phi_{H_2}+\Phi_{SiH_4})$=0.5 Pa) and low pressure deposition (Φ_{SiH_4}=2 sccm, Φ_{H_2}=0 sccm, p=p_{SiH_4}=2$\cdot$ 10^{-2} Pa). In both cases the filament temperature was set to approximately 1900°C.

A second group of experiments were prepared in order to evaluate the performance of the simple cavity protection device and its limitations: We studied the formation of silicides at the cold ends and the central region of three different 0.2 mm diameter filaments (L_{fil}=34 cm) for a certain accumulated deposition time. Two of the tested filaments had its corresponding cold ends protected by a simple cavity device while the other was completely unprotected. The accumulated deposition times ranged from approximately 1h to 13h. In these experiments, the following deposition conditions were used: Φ_{SiH_4}=10 sccm, Φ_{H_2}=90 sccm, p=5 Pa, $p_{SiH_4} \approx p \cdot \Phi_{SiH_4}$ / $(\Phi_{H_2}+\Phi_{SiH_4})$=0.5 Pa. Morphological studies and chemical analysis of the tested filaments were carried out by means of SEM and EDX. The filaments temperature was set to approximately 1900°C.

3.3.3 Results and discussion

Fig. 3.7 shows the normalized thickness profiles of the Si layers deposited on the internal walls of the cavity along its axis. Two tests have been carried out at two different silane partial pressures, p_{SiH_4}=0.5 Pa, and p_{SiH_4}=2·10^{-2} Pa. In both cases, the results have been fitted with Eq. 3.5.

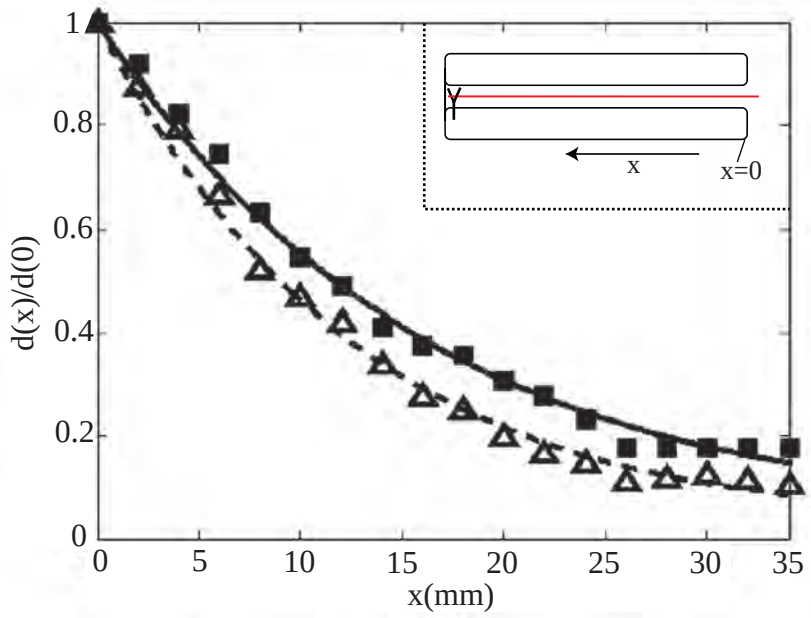

Figure 3.7: Normalized thickness profile of the Si layers deposited on the inner walls of the cavity along its axis. The squares and the triangles show the data obtained for p_{SiH_4}=0.5 Pa, and p_{SiH_4}=2·10^{-2} Pa respectively. The continuous and the dotted lines have been obtained fitting the data with Eq. 3.5.

The diameter of SiH_4 molecules is d_{SiH_4}=0.232 nm [75] and the gas temperature is estimated to be around T=600 K, which is a mean value between the wire temperature and the temperature that reaches the inner cavity wall due to filament radiation. Introducing these parameter values and the pressures previously mentioned in Eq. 3.3, the mean free path of silane molecules comes out to be of the order of few mm. Since λ_f is of the order of the cavity inner diameter, the system is subject to an intermediate flow regime close to a Knudsen type flow. Assuming the approximation of considering a Knudsen flow, the diffusion constant for a pipe is given by [72]

$$D = 2r_{cav} \cdot \bar{\nu}_{SiH_4}/3 \,, \tag{3.7}$$

where $\bar{\nu}_{SiH_4}$ is the mean thermal speed of the SiH_4 molecules. The number of molecules striking the filament per unit length and unit time is given by

$$\kappa_{dis} \cdot n(x) = \xi_{SiH_4} \frac{\bar{\nu}_{SiH_4}}{2r_{cav}^2} r_0 \cdot n(x) \,, \tag{3.8}$$

where ξ_{SiH_4} is the probability of SiH_4 dissociation.

From Eq. 3.5 it follows that the thickness $d(x)$ of the silicon layer deposited on the inner cavity walls decays exponentially with a characteristic length scale λ_2:

$$\lambda_2 = \sqrt{\frac{4r_{cav}^3}{3\xi_{SiH_4} r_0}} \,. \tag{3.9}$$

The theoretical estimation of λ_2 taking a filament radius r_0=0.1 mm, r_{cav}=2 mm and ξ_{SiH_4} ≈0.4 for T_{fil} ≈2000°C [64], gives λ_2 ≈16 mm.

The characteristic length scale λ_2 resulting from the fittings of the experimental data (see Fig. 3.7) is about 16 mm for p_{SiH_4}=0.5 Pa and 12 mm for p_{SiH_4}=2·10^{-2} Pa. Both values show a good agreement with the theoretical estimation of λ_2. The decay factor is fully determined by the two radius (r_0 and r_{cav}) of the system and by the dissociation probability of the catalyzer.

Regarding the tests using long filaments of 34 cm length, the unprotected filament broke in about 1 h, while the protected filament did not break after more than 13 h of uninterrupted deposition. Nevertheless, the cavity does not avoid silicidation at the cold ends, but it drastically slows down the process, thus reducing the effects on the mechanical stability of the wire. Even though the protected filament lasted for more than 13 hours, at that moment the whole filament had already been converted into WSi_2 and furthermore, a pure Si layer grew at its surface. This means that its catalytic activity was practically suppressed. Fig. 3.8 shows the aspect of the cold ends and the central region of the tested filaments: an unprotected filament after 77 minutes of deposition time and two different filaments protected with a simple cavity device (with 77 min and 13 h of accumulated

deposition time). The Si concentrations found at the cold ends and the central region of each filament are summarised in Table 3.1.

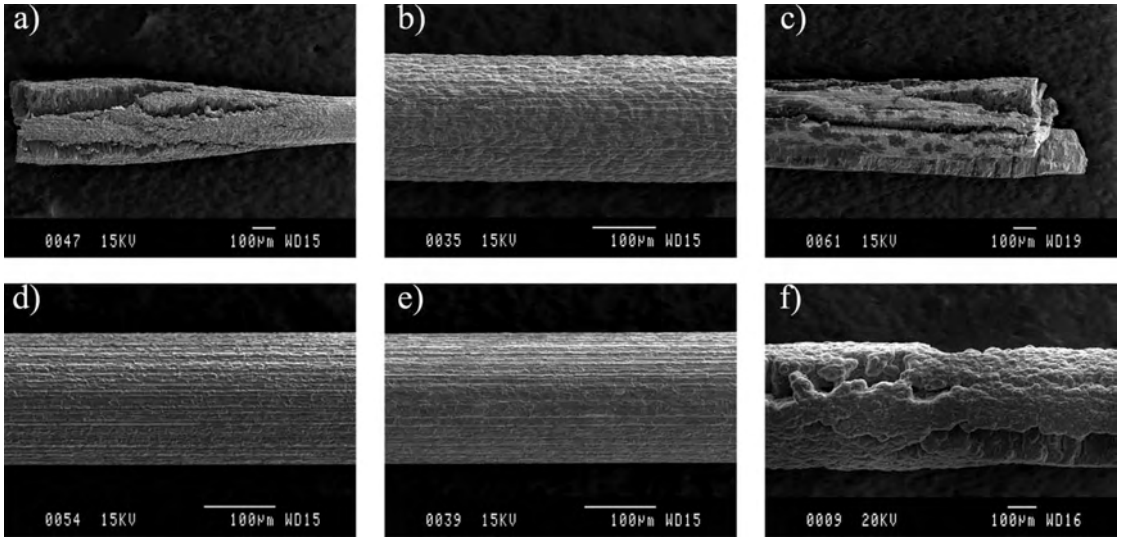

Figure 3.8: SEM images of a cold end and the central region of: an unprotected filament after 77 minutes of deposition time (a) and (d) respectively, a filament protected with a simple cavity device after 77 min (b) and (e) respectively, and a filament protected with a simple cavity device after 13 h of deposition time (c) and (f) respectively.

The benefits of using a simple cavity device are evident when one compares the aspect and Si concentration of the protected and unprotected filament cold ends: The latter are strongly silicidated and present huge fractures after 77 min of deposition time whereas the former have been only superficially silicidated and present much smaller cracks. On the other hand, as one would expect, there are no significant differences in the aspect and chemical composition of the central region of both filaments. In the case of the protected filament after 13 h of deposition time, there is no longer any difference between the cold ends and the central region, neither in morphology nor in chemical composition: Both present large cracks, a rich WSi_2 filament core and a pure Si superficial layer. As a result, the catalytic performance of the filament becomes practically null.

Table 3.1: Si:W ratio concentration, measured by EDX analysis, at the cold ends and the central region of either a protected filament and an unprotected filament after 77 minutes of deposition time and of a protected filament after 13 h of deposition time.

	Unprotected (77 min)	Protected (77 min)	Protected (13 h)
Cold end (surface)	66.2:33.8	45.9:54.1	94.3:5.7
Cold end (core)	63.3:36.7	0.0:100.0	65.4:34.6
Central region (surface)	3.7:96.3	3.7:96.3	99.8:0.2
Central region (core)	0.0:100.0	0.0:100.0	68.4:31.6

3.3.4 Conclusions

A simple cavity offers the opportunity of protecting the filament cold ends by reducing exponentially the silane concentration along its axis if its length is $L_{cav} \gg \lambda_2$. However, the use of simple cavity protection devices does not solve definitively the problem of filament ageing. Moreover, there is still a major drawback regarding the simple cavity protection device: Once the deposition process starts, the silicon layer deposited on the inner cavity walls may grow so thick that it eventually starts to peel off, thus filling the cavity with Si waste. If that occurs, the cavity protective mechanism is no longer effective and the deposition process must be interrupted to remove the Si waste and clean the cavity inner walls.

3.4 Cold ends protection using a self cleaning cavity

In the previous section, the limitations of a simple cavity protection device have been pointed out. We will now discuss the possibility of developing a self cleaning cavity to achieve a higher protection of the filament cold ends against silicidation and, at the same time, overcome the problem of Si waste peeling off from the cavity inner walls. This novel protection device must also be compatible with an eventual automatic filament replacement mechanism. This means that the self cleaning cavity must have its both ends open to allow the filament movement through it.

To assure cleanness inside the self cleaning cavity device, we can take advantage of the Si etching properties of atomic hydrogen [66, 76]. If one manages to locate the filament cold ends into a cavity wherein the partial pressure of silane p_{SiH_4} is kept low and highly diluted with hydrogen and, at the same time, the H_2 molecules are decomposed into atomic H, it is expected that Si deposition over the walls will be suppressed and that the cold ends silicidation will be minimised. Fig. 3.9 shows an schematic view of the proposed design for a self cleaning cavity device.

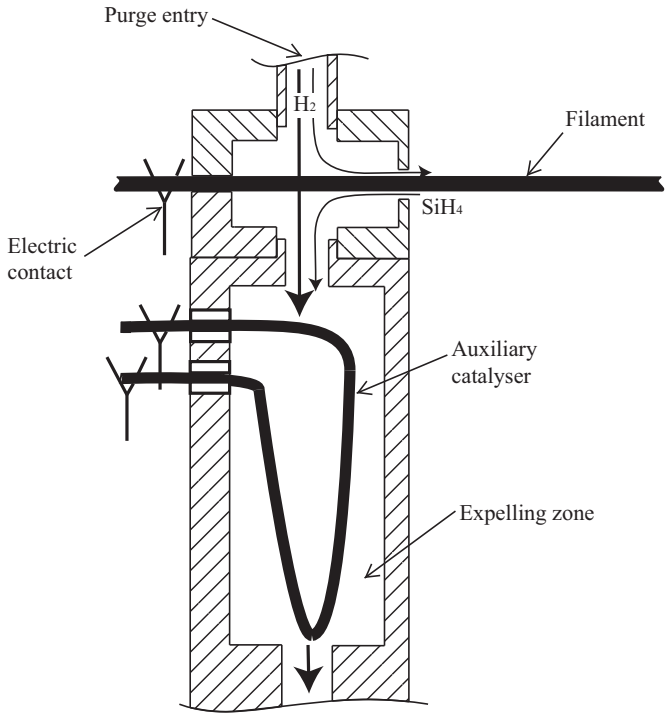

Figure 3.9: Schematic view of the proposed self cleaning cavity device.

The scheme shown in Fig. 3.9 includes a cavity through which the filament is passing. A purge gas (H_2) flow inlet is directly connected to this cavity. Contrary to prior solutions [67, 68], wherein the purge gas is expelled from the cavity through the same open end through which the catalytic filament is passing, in the proposed self cleaning cavity device, the majority of the purge gas flow leaves the cavity through an alternative exit hole towards an auxiliary expelling zone. Only a small fraction of the purge gas flow exits from the cavity open end through which the filament is passing. This means that the cooling of the filament por-

tion near the cavity exit is negligible if moderate (≈20 sccm) H_2 purge flows are used. In addition, an auxiliary catalyser is located inside the expelling zone. This auxiliary catalyser is heated to high temperature (>1900°C) by Joule effect during the HWCVD process to dissociate the H_2 gas molecules and activate its etching properties. The auxiliary catalyser also decomposes the SiH_4 molecules that reach the expelling zone and assures that p_{SiH_4} inside the expelling zone is much lower than in the deposition area. The deposition area is the space region wherein the portion(s) of the catalytic filament(s) that contribute(s) to the film growth on the substrate (i.e the portion of filament between the electric contacts, discounting the filament parts surrounded by the cold ends protection devices) is (are) located. In this way, the SiH_4 molecules that inevitably effuse into the cavity through its open end, are forced to flow towards the expelling zone where p_{SiH_4} is much minor. Hence, the region wherein the filament cold ends are located is always kept in a highly hydrogen diluted atmosphere with low p_{SiH_4} and a large presence of atomic hydrogen that keeps the area clean. The expelling zone can be connected to an alternative pumping system or, as in our tests, evacuated directly through the reactor vacuum chamber. The geometry of the device and the purge H_2 flow must be dimensioned in order to get proper values of the conductances involved as well as an appropriate H_2 and SiH_4 flow distribution. A self cleaning cavity device like that depicted in Fig. 3.9, was built in our workshop in aluminium in two parts. A water serpentine was used for the cooling of the device.

3.4.1 Experimental tests of a self cleaning cavity protection device

The experimental tests for proving the feasibility of the self cleaning cavity device were carried out in our single vacuum chamber HWCVD reactor. A single tungsten filament of 0.2 mm diameter was used. Next to one of the electric contacts it was implemented the developed self cleaning cavity device while the other filament cold end was protected by a simple cavity device as that described in section 3.3 with the only difference that, in this case, the two cavity ends were open and the cavity length was 30 mm. The whole assembly permitted the filament displacement across both protection devices and the corresponding electric contacts. Hence, the tests could be performed using an own developed automatic filament

replacement mechanism. The technological details and working principle of this filament replacement mechanism will be described in the following section 3.5. By now, it is only necessary to state that a portion of filament is able to be unwound from a storage reel and move across the deposition area towards a reception reel where it is wound by means of the action of a step by step motor. Four meters of tungsten filament were loaded on the storage reel. The portion of filament located between both electric contacts was kept straight during all operating situations by means of a spring mechanism. From now on, we will only refer to the issues concerning the self cleaning cavity device.

The experimental tests conceived for evaluating the protective performance of the self cleaning cavity consisted in several series of deposition runs of 20 min each. After each deposition run, the used portion of filament, located between the two electric contacts, was wound on the reception reel, thus being fully replaced by a new clean portion of the same filament unwound from the storage reel. Each deposition run took place under the following conditions: T_{fil} ≈1850°C, Φ_{SiH_4}=5 sccm, Φ_{H_2}=20 sccm, p=10 Pa. All the H_2 flow was introduced in the reactor chamber through the entry hole of the self cleaning cavity device as a purge gas. The effects of silicidation on the different regions of the portion of filament used in a single run have been studied by means of SEM images and EDX analysis.

However, many other preliminary tests were carried out using the same experimental set-up. Summarising, the self cleaning cavity device has been operating for an accumulated deposition time of more than 10 h.

3.4.2 Results and discussion

Fig. 3.10 shows SEM images taken from three different regions of a portion of filament that was used during a single deposition run as those previously described. Pictures (a) and (d) correspond to the cold end that has been protected with the self cleaning cavity. It can be observed that the filament is in almost perfect conditions. There is no sign of cracking and only a little corona (≈10 μm depth) is observable when one looks at the cross section image. This outer corona may correspond to a region wherein Si is diluted within the W bulk with a very low atomic percentage (beyond the limit resolution of the EDX analysis system) or it could also be an effect of W recrystallisation due to the filament annealing

process. In fact, the cold end protected by the self cleaning cavity seems to be in better conditions than the central region of the filament, see pictures (b) and (e), where the outer corona is much thicker (≈30 μm depth). In this central region, EDX analysis showed that the outer corona presents atomic Si contents between 0% (at 30 μm depth) and 36% (at 1-3 μm depth), suggesting that W_5Si_3 silicide formation has already started close to the filament surface. In particular, picture (e) evidences this contrast of the filament conditions as it shows a region of the filament that is partially inside (left side) and outside (right side) the self cleaning cavity. On the other hand, the cold end protected by the simple cavity device (pictures (c) and (f)) presents a large density of cracks and an outer corona of about 40-50 μm depth which is composed of rich silicon WSi_2 silicide phase. Table 3.2 shows the Si:W atomic ratio measurements performed at different regions of this used portion of filament.

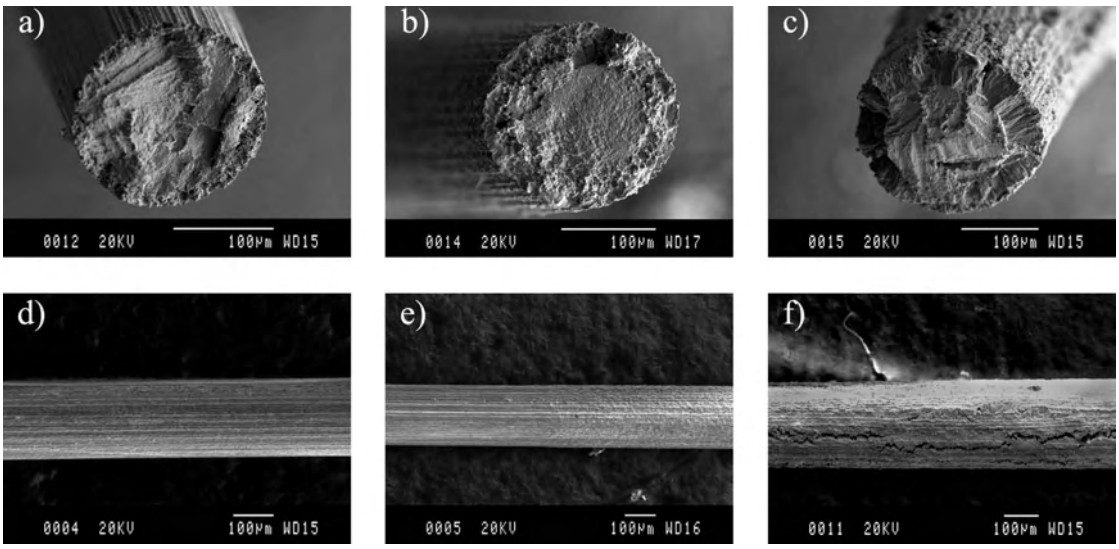

Figure 3.10: SEM images of a used portion of filament during a single deposition run: (a), (b) and (c) are cross section images of the cold end protected by the self cleaning cavity, the central region of the filament located in the deposition area and the cold end protected by the simple cavity respectively; (d), (e) and (f) are zoom out images of the cold end protected by the self cleaning cavity, the portion of filament located near the exit hole of the self cleaning cavity and the cold end protected by the simple cavity respectively.

The aspect of the inner walls of either the simple cavity and the self cleaning cavity has been photographed after a certain amount of accumulated deposition

Table 3.2: Si:W ratio concentration, measured by EDX analysis, at the inner core and the outer corona present at different regions of the used portion of filament during a single deposition run.

	Outer corona	Inner core
Cold end (self cleaning cavity)	0.0:100.0	0.0:100.0
Cold end (simple cavity)	66.5:33.5	2:98
Central region (deposition area)	(0.0-36.8):(100.0-63.2)	0.0:100.0

time for each device (less than 3 h for the simple cavity and more than 10 h for the self cleaning cavity). If one compares the pictures shown in Fig. 3.11 it is clear that the self cleaning cavity mechanism accomplishes the objective of maintaining the inner walls clean from Si deposition. On the other hand, the simple cavity needs to be cleaned very often as it is rapidly filled with Si material that peeled off from its inner walls.

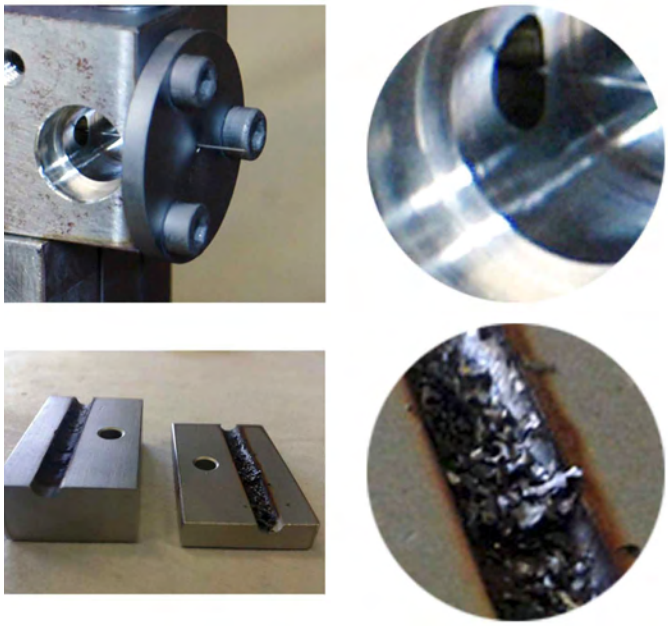

Figure 3.11: Pictures of the self cleaning cavity (top) and the simple cavity (bottom) after a total operating time of 10 h and 3 h respectively. A zoom from the interior of both devices is also showed. The simple cavity was made in two slices to allow photographing its interior.

3.4.3 Conclusions

A self cleaning cavity device has been developed to protect the filament cold ends. This new device slows down the silicidation at the cold ends to a rate even lower than that at the central region of the filament. By using an auxiliary catalyser, which is able to create a large amount of atomic hydrogen by catalytically activating the H_2 purge gas, any silicon deposition at the interior of the device can be prevented. The developed self cleaning cavity is compatible with an automatic filament replacement mechanism (described in the following section 3.5).

3.5 Automatic filament replacement mechanism

As it has been pointed out in the introduction of this chapter, the mere protection of the filament cold ends, though being necessary, is not sufficient to guarantee large uninterrupted operating times of an eventual industrial HWCVD reactor because the silicidation of the central region of the filament is inevitable. To overcome this problem, a filament replacement mechanism must be developed and it must be able to implement an effective protection device for the filament cold ends. Already in 1994, Takaoki (patent application JP7254566-A) proposed a first apparatus to replace the used filament making use of a storage reel for feeding clean filament into the deposition area and a storage reel to receive the compromised portion of the filament. It has already been pointed out in the introduction of this chapter that all the apparatus of this kind proposed in the past, but probably never constructed; JP7254566-A, JP2008140945, and US2008/0095937-A1, are not adequate for deposition systems composed of several filaments. For this reason, we developed a new apparatus based on the usage of tension adjustment mechanism modulus which act independently over each filament. The utilisation of this tension adjustment mechanism makes it possible to replace the different catalytic filaments in parallel using only one or, maximum, two motors. Figs. 3.12 and 3.13, show two possible configurations for such apparatus.

As it can be seen in Fig. 3.12 there is an independent tension adjustment mechanism for each filament. Said tension adjustment mechanisms work the following way: A constant force spring is attached by its ends to both a storage drum and a torque output drum. Said drums are adapted to turn in opposite directions. The

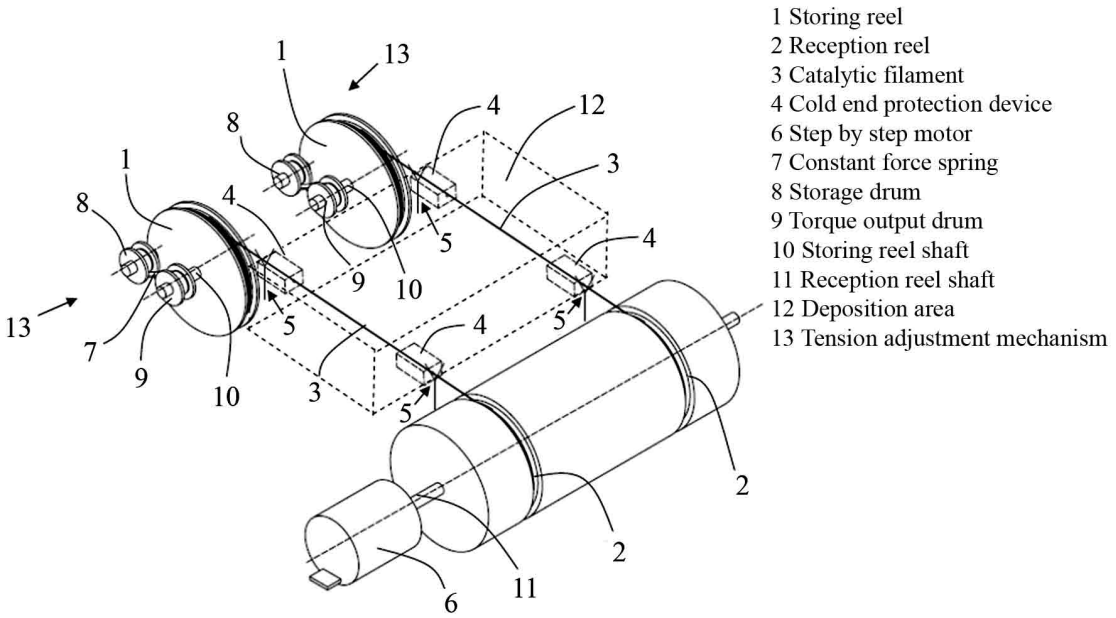

Figure 3.12: Schematic view of a particular embodiment of the filament replacement mechanism, including the corresponding tension adjustment mechanisms and the protection devices for the cold ends of the filaments. A HWCVD system with two catalytic filaments is represented.

torque output drum is coupled to the storage reel by means of a shaft. When the step by step motor turns, the storage and the reception reels rotate in the same direction. Let us assume that the motor rotates clockwise. Then, the reception reel, the storage reel and the torque output drum do also rotate clockwise while the storage drum rotates counterclockwise. In this case, the constant force spring is unwound from the storage drum and wound around the torque output drum. This operating condition entails that the used portion of filament is being replaced by a new portion of filament coming from the storage reel and, simultaneously, that the constant force spring gets charged. If the motor rotates counterclockwise, the whole situation is reversed and the constant force spring is discharged. No matter how much the constant force spring has been charged, the torque output drum applies a constant torque on the storage reel which is, at last, traduced into a pulling constant force exerted on the corresponding filament. However, it may happen that the limited length of the constant force spring does not allow to make use of the whole filament that was initially wound on the storage reel. Then,

one may think of implementing a supplementary mechanism that allows charging and/or discharging the constant force spring when necessary without transferring any motion to the corresponding catalytic filament. Fig. 3.13 shows a particular embodiment of the filament replacement mechanism applied to the case of two catalytic filaments where a charging/discharging mechanism is implemented for each tension adjustment mechanism.

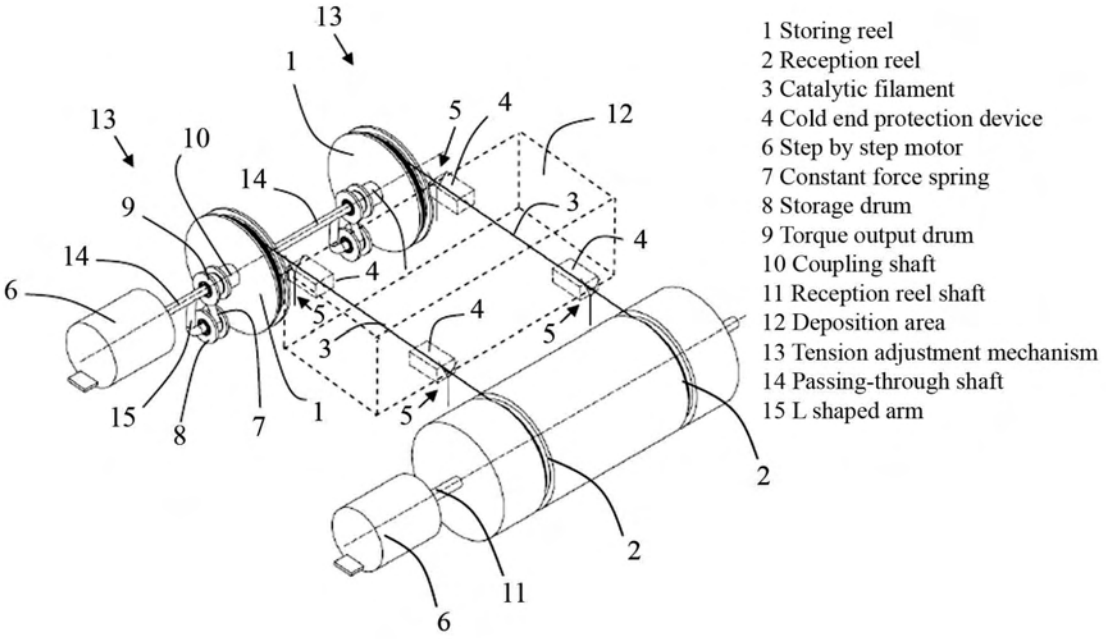

Figure 3.13: Schematic view of a particular embodiment of the filament replacement mechanism, including the corresponding tension adjustment mechanisms with a charging/discharging mechanism for the constant force spring and the protection devices for the cold ends of the filaments. A HWCVD system with two catalytic filaments is represented.

In the arrangement shown in Fig. 3.13 a second step by step motor is used for transferring motion to all the implemented charging/discharging mechanisms. The shaft of this second motor passes through the torque output drum and the storage reel of each tension adjustment mechanism by means of a bearing. Each storage drum is coupled to the second motor shaft by means of a bearing arranged with a l-shaped arm in such a way that the storage drum is able to rotate around its own axis. When the second motor rotates, the storage drum of each tension adjustment mechanism traces a circular path around its corresponding torque output drum

thus charging or discharging the constant force spring depending on if the rotation direction is counterclockwise or clockwise.

3.5.1 Experimental tests of the developed automatic filament replacement mechanism

The automatic filament replacement mechanism tested in our laboratory was built like the assembly sketched in Fig. 3.12 for the case of using a single 0.2 mm diameter tungsten filament. Both reels radii and the tension adjustment mechanism were accordingly dimensioned. The assembly was introduced in our single chamber HWCVD reactor. A position controlled step by step motor was located outside the vacuum chamber to transfer motion to the reception reel by means of a rotatory pass-through. Two different aspects were considered for the validation tests of the developed filament replacement mechanism: Firstly, the capability of the developed mechanism in replacing automatically a portion of used catalytic filament without breaking the vacuum has been evaluated. The main point was to test the effectiveness of the tension adjustment mechanism in keeping the filament straight during all operating situations. Secondly, it was also necessary to verify that the replacement of a portion of used catalytic filament leads the HWCVD apparatus back to the same initial conditions observed before the deposition took place.

The validation tests consist in a series of deposition cycles. The depositions were carried out under conditions compatible with a-Si:H growth. Each deposition cycle consisted in:
- heating up the tungsten filament to about 1850°C by Joule effect using a constant voltage supply;
- introducing a silane and hydrogen gas mixture (Φ_{SiH_4}=5 sccm, Φ_{H_2}=20 sccm) in the vacuum chamber at a pressure of about p=10 Pa;
- carrying out a deposition for a deposition period time of 20 minutes under the described conditions;
- stopping the deposition (Φ_{SiH_4}=0 sccm, Φ_{H_2}=0 sccm);
- reducing the tungsten filament to a temperature below 1000°C; and
- automatically changing the used portion of tungsten filament, comprised between the two electric contacts, which is then replaced by another clean portion of cat-

alytic filament.

The voltage supply used to heat the catalytic filament by Joule effect was switched off once every two deposition cycles. The catalytic filament was observed during the whole process to be sure that it was not subjected to any bending originated from the lengthening caused by thermal expansion. To check the stability and repeatability of the process, the electric current flowing through the catalytic filament was monitored. The reported results are taken from tests wherein a self cleaning cavity has been implemented for the protection of one cold end, whereas the other cold end is being protected by a simple cavity as in the experimental tests described in section 3.4.

3.5.2 Results and discussion

It was observed that the filament was kept straight during the whole test (no bending from thermal expansion was observed) indicating that the conceived tension adjustment mechanism was working correctly. It was also verified that during the replacement of a used portion of filament, this last is successfully wound on the reception reel without any risk of filament breakage.

Fig. 3.14 shows the electric current flowing through the tungsten catalytic filament monitored during a deposition sequence which consists of six deposition cycles. When the electric current is around $I \approx 3.4$ A, the approximate temperature of the filament is 1850°C. During these time periods, the precursor gas mixture enters into the vacuum chamber and the deposition process takes place. The period times when $I \approx 1.4$ A correspond to the replacement of the used portion of catalytic filament by another clean portion of catalytic filament. During each deposition period time ($I \approx 3.4$ A), the measured electric current slowly decreases with time. This indicates an increase of the electric resistance of the used portion of filament that may be due to its degradation during the deposition period time (20 minutes). Nevertheless, the electric current fluctuations are less than $\pm 1\%$ and are attributed to silicides formation at the filament cold end that is being protected by the less effective simple cavity device. The replacement of the used portion of catalytic filament takes back the electric current to its initial value observed at the beginning of each deposition cycle.

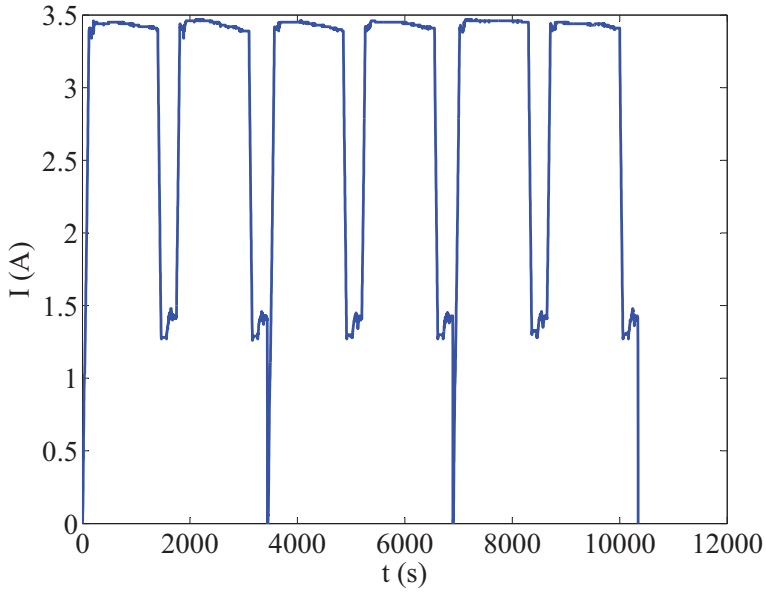

Figure 3.14: Electric current as a function of time during the validation test of the filament replacement mechanism which consisted in 6 consecutive deposition cycles. Once every two deposition cycles, the electric power which feeds the filament was switched off.

3.5.3 Conclusions

We have developed an automatic filament replacement mechanism that allows replacing a used portion of filament by another clean portion of filament, without breaking vacuum. The apparatus is conceived in a modular way, based on the usage of tension adjustment mechanism moduli which act independently over each filament. The utilisation of said tension adjustment mechanism makes it possible to replace the used portions of the different filaments in parallel, keeping them tense in all operating situations and using only one or, maximum, two motors. The system is easily scalable to large deposition areas as it can be arranged for any arbitrary number of filaments without increasing the number of motors involved. The results obtained from the validation tests prove that the developed filament replacement mechanism, in combination with the use of effective cold end protection devices, such as the self cleaning cavity, guarantees the repeatability and stability of a HWCVD deposition process for silicon based materials.

Chapter 4

The scaling-up of the HWCVD technique

4.1 Introduction

At present, lots of efforts are focused in developing deposition systems which allow depositing μc-Si:H over large area substrates (>1 m^2) with very low inhomogeneity (< $\pm$5 %) and at high deposition rate (r_d >1 nm/s). Such requirements are necessary to make the production of micromorph [3] modules economically profitable what would allow the upgrade of the current amorphous silicon (a-Si:H) thin film solar cell factories. As we have pointed out in the introduction of this thesis, HWCVD has arisen as a promising technique for the deposition of μc-Si:H. On one hand, some pilot scale HWCVD reactors have been developed in the last years for the deposition of a-Si:H and/or μc-Si:H over large area [22, 33, 77, 78]. However, the inhomogeneities of the films deposited with these systems, for either a-Si:H or μc-Si:H, are considerably larger than $\pm$5%. In the case of μc-Si:H, the crystallinity of the deposited layers shows substantial variations [22] what compromises the quality of the material at some regions of the substrate. Still, this problem can be solved as the uniformity of the films can be improved by using a convenient filament net design [35]. On the other hand, it has already been demonstrated that HWCVD has the potential to deposit μc-Si:H layers at r_d $\geq$3 nm/s [30, 31] although the quality of the obtained material is very poor. In-

deed, high quality μc-Si:H layers are only obtained for deposition rates lower than r_d <0.5 nm/s [27,36,37]. The usual deposition conditions for device grade μc-Si:H are: deposition pressure p=1-5 Pa, filament to substrate distance d_{f-s}=50-80 mm, substrate temperature T_s=180-250°C and filament temperature T_{fil} <1800°C for either W or Ta filaments [19,27,37,79]. Thick 0.5 mm diameter filaments are normally used to avoid a premature breakage of the filaments. An increment of r_d can be achieved by using higher filament temperatures, higher pressures or increasing the filament catalytic surface [80]. However, these strategies lead to a decrease of the quality of the deposited material [81]. In particular, the increment of r_d is strongly limited by the radiation coming from the filaments because the substrate temperature must be kept reasonably low to obtain high quality material. Thus, using thick catalytic filaments is useful to avoid their premature breakage but constitutes a limiting factor for increasing the deposition rate of high quality μc-Si:H. This chapter exposes a discussion about the possibility of finding scaling laws that allow the deposition of high quality μc-Si:H with HWCVD over large area, with high homogeneity and at high deposition rate.

Our approach to increase r_d is somewhat different: We assume that there exists an optimal value of the product $p \cdot d_{f-s}$ for the deposition of high quality μc-Si:H as in the case of a-Si:H deposition [82]. The basis for this assumption are exposed in section 4.2. If p is increased and d_{f-s} is proportionally decreased, the optimal value of $p \cdot d_{f-s}$ can be kept constant what would allow increasing the deposition rate of high quality μc-Si:H. We must then use thin filaments (with a diameter of 0.1-0.2 mm) to reduce the amount of heat radiated on the substrate. In this way, we can use relatively high filament temperatures, around 1850°C, and use a dense filament net that assures high homogeneity of the film over the whole substrate for small d_{f-s} (around 15-20 mm). We must notice that the problem of filament breakage is not really a limiting issue because, as we have shown in the previous chapters, the *effective filament lifetime* does not depend on the filament radius r_0 and, furthermore, there exists the possibility of implementing an automatic filament replacement mechanism (like, for instance, those depicted in Figs.3.12 and 3.13).

In section 4.2 we will deal with the reaction-diffusion equations that govern the deposition of Si in HWCVD when pure SiH_4 is used as precursor gas. We will also discuss the possible existence of a scaling law for r_d if the value of $p \cdot d_{f-s}$ is

kept constant. In section 4.3 we will expose a diffusion model that predicts the thickness uniformity of a film deposited using any given filament net configuration and d_{f-s}. The accuracy of the proposed model will be tested by measuring the thickness profile of a-Si:H and μc-Si:H samples deposited using a catalytic filament net that covers an area of 20 cm $\times$ 20 cm. The obtained thickness inhomogeneities, in the central 10 cm $\times$ 10 cm substrate area, are lower than 2.5% if a proper d_{f-s} is used. Furthermore, we will show that there exists a *large area limit*, which is only dependant on geometrical parameters, that allows studying the behaviour of any arbitrary larger HWCVD reactor making use of a relative small prototype like ours. In section 4.4 we will examine in more detail the deposition conditions which keep invariant the involved reaction-diffusion equations in the more general case, compatible with μc-Si:H deposition, wherein a mixture of H_2 and SiH_4 is used as precursor gas. Under such conditions, we will experimentally test the stated scaling law for r_d and characterize the deposited material by means of Raman spectroscopy.

4.2 Basic chemistry in HWCVD for Si deposition using SiH_4 as precursor gas

The deposition of Si films with HWCVD technique by using pure SiH_4 as precursor gas involves a very rich chemistry [41]. The primary reaction deals with the generation of Si and H radicals at the filament surface:

$$SiH_4 \xrightarrow{\xi_{SiH_4}} Si + 4H \ , \tag{4.1}$$

where ξ_{SiH_4} is the dissociation probability of SiH_4 at the filament surface. These primary Si radicals diffuse away from the filament surface and react with silane molecules generating new species. For a given silane partial pressure ($p = p_{SiH_4}$), if the distance between the filament and the substrate d_{f-s} is too short, the generated Si radicals will directly deposit on the substrate. On the other hand, if d_{f-s} is too long, large radicals will be generated by secondary radical-radical reactions. Both situations usually lead to the deposition of very low quality material. It is

then clear that the generation rates of the different chemical species involved in the growth of the film depend on the value of the product $p \cdot d_{f-s}$. In the case of high quality a-Si:H deposition, it has been reported an optimal value of $p \cdot d_{f-s}$=4 Pa·cm [82]. W. Zheng and A. Gallagher [63] showed that, among the secondary radicals generated, the dominant specie involved in the deposition of high quality a-Si:H is the disilyne molecule (Si_2H_2). The secondary reaction responsible for the generation of Si_2H_2 reads

$$Si + SiH_4 \longrightarrow Si_2H_2 + H_2 \, . \tag{4.2}$$

The SiH_3 radicals, generated by the reaction

$$H + SiH_4 \longrightarrow SiH_3 + H_2 \, , \tag{4.3}$$

are supposed to have a beneficial influence in the growth of a-Si:H films. However, SiH_3 appears to play a minor role in HWCVD for a-Si:H deposition although it is not yet quantitatively understood [63]. On the other hand, the incorporation of primary Si radicals or larger secondary radicals like Si_3H_n into the film is highly detrimental for the quality of the deposited material and the contribution of these species is practically null in the deposition conditions compatible with high quality a-Si:H [63].

Alternatively, Martin *et al.* [71] found that high quality epitaxial Si layers could be deposited using a $p \cdot d_{f-s}$ product similar to that for a-Si:H deposition and that, in this regime, the dominant specie responsible for the growth of the film was again Si_2H_2. Of course, for the deposition of epitaxial Si, much higher substrate temperatures are required (above 620°C). The aforementioned works used SiH_4 diluted with He [82] or pure SiH_4 [63, 71] as precursor gases.

4.2.1 The reaction-diffusion equations and their invariance for a fixed $p \cdot d_{f-s}$ product

In a HWCVD deposition process, the spatial distribution of the concentration of the different species is driven by diffusion and depends on the rate of the chemical

reactions that transform the radicals into each other. Assuming that there exists a stationary solution of the problem, the set of reaction-diffusion equations that describes the system is

$$D_i \Delta_x n_i + \sum_{j \neq l}^{N} n_j \kappa_{j,l} n_l = 0 \,, \tag{4.4}$$

the solution of which allows determining the concentration n_i of the different N chemical species involved in the deposition process. It has been assumed that all chemical reactions relevant for the deposition process have a first order dependence with n_j and n_l. D_i is the diffusion coefficient of each chemical specie and $\kappa_{j,l}$ is the rate of the chemical reaction between the species j and l. In the case of high quality a-Si:H deposition, we have already mentioned that Si_2H_2 is the dominant specie involved in the film growth. Hence, the most important reaction-diffusion equations involved in the growth of high quality a-Si:H are

$$\begin{aligned} D_{Si_2H_2} \Delta_x n_{Si_2H_2} + n_{Si} \kappa_{Si,SiH_4} n_{SiH_4} &= 0 \\ D_{Si} \Delta_x n_{Si} - n_{Si} \kappa_{Si,SiH_4} n_{SiH_4} &= 0 \,, \end{aligned} \tag{4.5}$$

where the opposite signs of the second term refer, respectively, to the creation of Si_2H_2 and the destruction of Si for the reaction between Si and SiH_4. We can see in Eqs. 4.5 that the generation of Si radicals at the filaments surface determines the creation of Si_2H_2 given by the reaction 4.2. Assuming that the diffusion coefficients of Si and Si_2H_2 are approximately the same ($D_{Si} \approx D_{Si_2H_2} \approx D$), from the sum of Eqs. 4.5 one obtains

$$D \Delta_x (n_{tot}) = 0 \,, \tag{4.6}$$

where $n_{tot} = n_{Si} + n_{Si_2H_2}$. In the following section 4.3, we will see that when the term of radicals generation at the filaments surface is included in Eq. 4.6, it takes the form of the Poisson's equation. The numerical solution of this equation will be used to compute the expected thickness uniformity of a deposited film for any

given filament net configuration and filament to substrate distance. By now, let us go back to the general case stated by the set of Eqs. 4.4 and see that it can be reduced to a dimensionless form by applying an adequate variable change like

$$\tilde{D} = D \cdot n_{tot},\ \tilde{n}_i = \frac{n_i}{n_{tot}},\ \tilde{x} = \frac{x}{\lambda_3}\,, \tag{4.7}$$

where n_{tot} is now the total concentration of all chemical species and λ_3 is a characteristic length of the HWCVD reactor. In our case, λ_3 can be associated to d_{f-s}. Under the variables change of Eq. 4.7, the set of Eqs. 4.4 takes the form

$$\tilde{D}_i \Delta_{\tilde{x}} \tilde{n}_i + \tilde{\mathbb{k}} \sum_{j \neq l}^{N} \tilde{n}_j \kappa_{j,l} \tilde{n}_l = 0\,, \tag{4.8}$$

and becomes invariable for a constant value of $\tilde{\mathbb{k}}{=}\lambda_3 \cdot n_{tot}$. This means that two different configurations of a HWCVD reactor ($\tilde{\mathbb{k}}{=}\lambda_3 \cdot n_{tot}$ and $\tilde{\mathbb{k}}'{=}\lambda_3' \cdot n_{tot}'$) may lead to the same spatial distribution of the different chemical species if $\tilde{\mathbb{k}} = \tilde{\mathbb{k}}'$ is maintained. Hence, both configurations should lead to the deposition of identical material. Let us call p the total pressure of the reactor and assume that the gas temperature T is equal for both configurations. If one takes the ideal gas law $p = n_{tot} kT$ and takes $\lambda_3 = d_{f-s}$ as the characteristic length of the reactor, it can be seen that keeping $\tilde{\mathbb{k}} = \tilde{\mathbb{k}}'$ invariable is equivalent to the following condition:

$$\tilde{\mathbb{k}} = \tilde{\mathbb{k}}' \Leftrightarrow \mathbb{k} = p' \cdot d_{f-s}' = p \cdot d_{f-s} = \text{constant}\,. \tag{4.9}$$

For simplicity, from now on, we will make use of the parameter $\mathbb{k} = p \cdot d_{f-s}$. If we assume that the deposition rate is proportional to the total radicals flux reaching the substrate $\vec{J}$

$$\vec{J} = \frac{1}{d_{f-s}} \sum_{i}^{N} \tilde{D}_i \vec{\nabla}_{\tilde{x}} \tilde{n}_i\,, \tag{4.10}$$

we can conclude that the deposition rate will scale as follows

$$r'_d = \frac{d_{f-s}}{d'_{f-s}} r_d \,. \tag{4.11}$$

Nevertheless, we must notice that in order to preserve the material quality at higher r_d, keeping $\mathbb{k}$ constant is a necessary but, unfortunately, insufficient condition. As we will see in section 4.4, the necessary conditions to preserve the material quality are more strict than simply keeping constant the $p \cdot d_{f-s}$ product.

4.3 Film thickness uniformity in HWCVD

Even if r_d can be increased following Eq. 4.11, the chosen reactor configuration (including the number of filaments N, the filaments length L_{fil}, the filaments spatial distribution and d_{f-s}) must also assure that the deposited layer homogeneity will be satisfactory. This is particularly important in the case of μc-Si:H as the quality of the material is very sensitive to layer inhomogeneities. In this section, we will expose a model for the calculation of the thickness profile of a deposited layer with any given reactor configuration. This model will be applied to the case of N parallel filaments located at a distance d_{f-s} from the substrate. The computed simulation will be compared with experimental results for the case of either a-Si:H and μc-Si:H deposition.

4.3.1 Model for the film thickness uniformity in HWCVD

The following model assumes that the film thickness $d(\vec{x})$ in the coordinate $\vec{x} = (x, y, z)$ of the substrate is proportional to the total flux of radicals $\vec{J}(\vec{x})$ reaching this point during the stationary regime of the deposition process. $\vec{J}(\vec{x}) = -D\vec{\nabla}n(\vec{x})$ is a diffusion flux, being D the diffusion coefficient and $n(\vec{x})$ the total concentration of radicals involved in the film growth[1]. Introducing the term of radicals generation at the filaments surface in Eq. 4.6, the stationary diffusion that governs the species involved in the growth of the film takes the form of the Poisson's equation

[1] Note that the previous notation n_{tot} is, from now on, substituted by $n(\vec{x})$, eliminating the subscript for writing commodity reasons

$$D\Delta_x n(\vec{x}) = \varrho(\vec{x}) \qquad \text{for } \vec{x} \in \mathcal{S}\,, \tag{4.12}$$

where $\varrho(\vec{x}) = \partial n(\vec{x})/\partial t$ is the rate of radicals generation at the filament surface. The domain of definition $\mathcal{S}$ is considered to be a parallelepiped with one of its faces, $\delta\mathcal{S}$, occupied by the substrate. Eq. 4.12 is subject to Milne boundary conditions [83]

$$\hat{s} \cdot \vec{\nabla} n(\vec{x}) = \frac{1}{\lambda_4} n(\vec{x}) \qquad \text{for } \vec{x} \in \delta\mathcal{S}\,, \tag{4.13}$$

where $\hat{s}$ is the unitary vector normal to the substrate plane and λ_4=$2\lambda_f(2\text{-}\varphi_s)/3\varphi_s$ is a characteristic length scale of the problem wherein λ_f and φ_s are respectively, the mean free path and the sticking coefficient of the radicals.

4.3.2 The case of N identical, equidistant and parallel finite filaments

Let us consider a filament net, centered at $\vec{x}$=0, of N parallel filaments ($M = N-1$) of length L_{fil} lying in the $x-y$ plane and oriented along the y axis. Each filament generates radicals at a rate per unit length $\varrho(\vec{x}) = \Gamma$. The filaments are separated a distance d_{f-f} from each other and the gap between the substrate and the filament net is d_{f-s}. It may be clarifying to mention that solving Eq. 4.12 is now analogous to the electrostatic problem of calculating the electric potential originated by N parallel, finite linear distributions of electric charge. In our case, $n(\vec{x})$, $\vec{J}(\vec{x})$, D and Γ play the role of, respectively, the electric potential $U(\vec{x})$, the electric displacement field $\vec{D}(\vec{x})$, the medium permittivity ε and the linear charge density λ_q. Using the superposition principle, one finds that the solution of Eq. 4.12 for the trivial boundary condition $n(\vec{x})$=0 for $|\,\vec{x}\,| \to \infty$ is given by

$$n_0(\vec{x}) = \frac{\Gamma}{4\pi D} \sum_{i=0}^{M} ln\left(\frac{f_+(\vec{x}) + (y + L_{fil}/2)}{f_-(\vec{x}) + (y - L_{fil}/2)}\right)\,, \tag{4.14}$$

with

$$f_{\pm}(\vec{x}) = \sqrt{(x + d_{f-f}(i - M/2))^2 + z^2 + (y \pm L_{fil}/2)^2}\,,$$

and the corresponding radical flux $\vec{J}_0(\vec{x}) = -D\vec{\nabla}n_0(\vec{x})$ is given by

$$\begin{aligned}
\vec{J}_0(\vec{x}) &= -\frac{\Gamma}{4\pi D}\sum_{i=0}^{M}\left[\frac{1}{f_+(\vec{x})}\begin{pmatrix} x + d_{f-f}(i - M/2) \\ y + L_{fil}/2 \\ z \end{pmatrix} + \vec{I}_y\right]\cdot \\
&\cdot \quad \frac{1}{f_+(\vec{x}) + (y + L_{fil}/2)} - \left[\frac{1}{f_-(\vec{x})}\begin{pmatrix} x + d_{f-f}(i - M/2) \\ y - L_{fil}/2 \\ z \end{pmatrix} + \vec{I}_y\right]\cdot \\
&\cdot \quad \frac{1}{f_+(\vec{x}) + (y - L_{fil}/2)}\,,
\end{aligned} \tag{4.15}$$

where $\vec{I}_y$=(0,1,0). It is interesting to note that if $L_{fil} \to \infty$ the radicals concentration $n_0(\vec{x})$ diverges logarithmically whereas the radicals flux $\vec{J}_0(\vec{x})$ stays bounded. The Milne boundary conditions (Eq. 4.13), which are formally Robin type conditions, can be replaced by Dirichlet type boundary conditions, *i.e.* $n(\vec{x}) = 0$ at a distance λ_4 behind the boundary $\delta\mathcal{S}$. This approximation is valid as long as λ_4 is small compared to other length scales of the domain $\mathcal{S}$. The solution of Eq. 4.12 for these Dirichlet boundary conditions can be estimated using the images method [84]. Since the domain $\mathcal{S}$ is a parallelepiped defined by $\vec{a}$=($l_x = Nd_{f-f}$, $l_y = L_{fil}$, $l_z = 2d_{f-s}$), consecutive reflections between the walls (mirrors) will generate an infinite denumerable set of images. Taking advantage of the inversion centre of symmetry of $n_0(\vec{x})$, the solution of $n(\vec{x})$ can be written in the simplified form

$$n(\vec{x}) = \sum_{\vec{m}\in\mathcal{Z}^3}(-1)^{\vec{m}\cdot\vec{I}}n_0\left(\vec{x} + \vec{m}\cdot(\vec{a} + 2\lambda_4\vec{I})\vec{m}\right)\,, \tag{4.16}$$

where $\vec{I}$ is the identity vector (1,1,1), $\mathcal{Z}$ is the set of integer numbers and $\vec{m} \in \mathcal{Z}^3$ defines the location of all images included in the summation. In the same way, the corresponding radicals flux reads

$$\vec{J}(\vec{x}) = \sum_{\vec{m}\in\mathcal{Z}^3} (-1)^{\vec{m}\cdot\vec{I}} \vec{J}_0 \left(\vec{x} + \vec{m}\cdot(\vec{a} + 2\lambda_4\vec{I})\vec{m}\right) . \tag{4.17}$$

Let us now calculate the value of the radicals flux $\vec{J}(\vec{x})$ for an infinite net, wherein $N \to \infty$ and $L_{fil} \to \infty$. The result $\vec{J}(\vec{x}) = \Gamma\vec{x}/2\pi \mid \vec{x} \mid^2$ for a single infinite filament is straightforwardly obtained by applying Gauss' theorem. Applying the superposition principle, one obtains, for the whole filament net, the radicals flux perpendicular to the substrate plane J_z

$$J_z = lim_{M\to\infty} \sum_{i=0}^{M} \frac{\Gamma}{2\pi d_{f-s}} \cdot \frac{1}{1 + \left(\frac{d_{f-f}}{d_{f-s}}\right)^2 \left(i - \frac{M}{2}\right)^2} . \tag{4.18}$$

If the ratio (d_{f-f}/d_{f-s}) becomes very small, the summation over index i in Eq. 4.18 can be replaced by an integral over the variable x $\left(\sum_i \to \int dx\right)$. Evaluating the integral in the interval $(-\infty,\ \infty)$ one gets the result

$$J_z = \frac{\Gamma}{2d_{f-f}} , \tag{4.19}$$

which constitutes what we call *the infinite area limit*. In order to see how the radicals flux J_z generated by a finite filament net approaches the *infinite area limit* $\Gamma/2d_{f-f}$, Eq. 4.17 was solved for different number of filaments N and ratios d_{f-s}/d_{f-f} fixing $l_x = l_y = L_{fil} = Nd_{f-f}$. The infinite summation of Eq. 4.17 has been estimated following the procedure shown in Appendix E. Fig.4.1 shows the results for λ_4=$d_{f-f}/4$.

The horizontal dashed line at $J_z(N)$=$0.95\Gamma/2d_{f-f}$ in Fig.4.1 shows what we will consider from now on, *the large area limit*. For a given d_{f-s}, the filament net configurations (N, d_{f-f}, L_{fil}) leading to values of J_z above the large area limit are "seen" by the central point of the substrate as if they were practically an infinite filament net. This means that a further increment of N or L_{fil} would not substantially modify the radicals flux reaching the centre of the substrate. The vertical dashed line in Fig. 4.1 at N=12 shows the maximum number of filaments that our HWCVD deposition system can hold. Hence, we can see that the maximal filament to substrate distance for which the system is working beyond the large

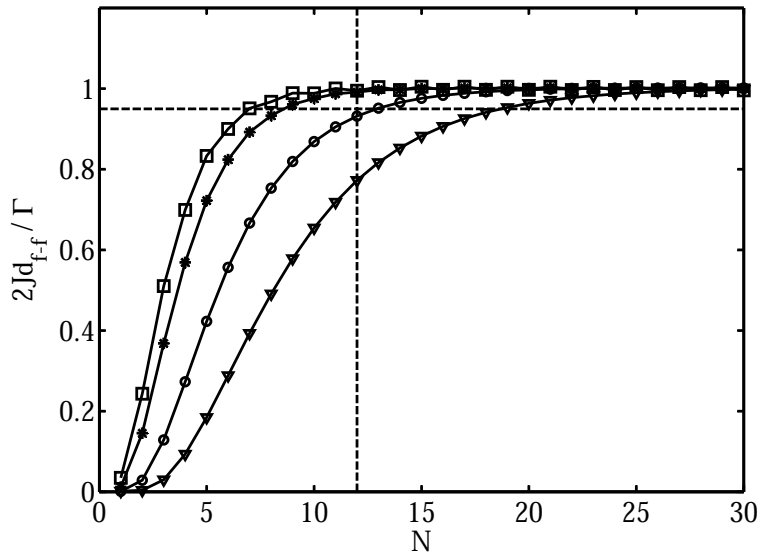

Figure 4.1: Radicals flux $J_z(N)$ as a function of N at the central point of the substrate calculated from the solution of Eq. 4.17 for λ_4=$d_{f-f}/4$ and normalized to the infinite area limit $\Gamma/2d_{f-f}$. The different plots correspond to: $d_{f-s} = 3d_{f-f}$ ($\triangledown$), $d_{f-s} = 2d_{f-f}$ ($\circ$), $d_{f-s} = 1.25d_{f-f}$ ($*$), $d_{f-s} = d_{f-f}$ ($\square$).

area limit is $d_{f-s} = 2d_{f-f}$. This result will be important for the experimental verification of the possible existence of a scaling law for r_d (see section 4.4).

4.3.3 Experimental Details

To check the validity of the diffusion model presented in section 4.3.1, the thickness profile, $d(\vec{x})$, measurements of a-Si:H and μc-Si:H thin films deposited over a glass substrate of 20 cm $\times$ 20 cm have been performed. The description of our single chamber HWCVD reactor is given in Appendix A. The catalytic net was formed by 12 filaments of 0.15 mm diameter with a filament to filament distance d_{f-f}=16 mm. The filaments length was L_{fil}=20 cm. For all the depositions, a base pressure of 10^{-4} Pa was considered low enough taking into account the aim of this study. A constant DC voltage (22 V) power source was used to heat the filaments by Joule effect. Regarding μc-Si:H films, the deposition conditions were T_s=275°C, T_{fil} ≈1850°C, Φ_{SiH_4}=12 sccm, Φ_{H_2}=188 sccm, p=10 Pa. Three different filament to substrate distances were used (d_{f-s}=10 mm, 15 mm and 20 mm). The de-

position time was in all cases 900 s. In the case of a-Si:H films, the deposition conditions were T_s=275°C, T_{fil} ≈1850°C, Φ_{SiH_4}= 60 sccm, Φ_{H_2}=140 sccm, p= 10 Pa, with two different filament to substrate distances (d_{f-s}= 15 mm and 20 mm). The deposition time was in all cases 180 s. According to the simulations plotted in Fig.4.1, our deposition system was always working beyond the large area limit.

The thickness profile of all the deposited films was calculated by means of optical transmission measurement mappings which were carried out with a home made experimental set-up. An $x-y$ table was used to scan the samples over an area of 170 mm x 170 mm with 1 mm step between measurements, while an Ocean Optics USB2000 spectrophotometer was used, via optical fiber, to collect the transmission signal. The light source covered a wavelength range from 400 nm to 1000 nm. The experimental set up was controlled and the data were analysed with homemade software. The well known Swanepoel envelope method [85] was used to determine the thickness profile of the deposited films. However, for each scan it was necessary one thickness measurement with profilometer to fix the interference order.

The so called *Raman crystallinity factor* (χ_c) of the material was evaluated by Raman spectroscopy measurements (Micro Raman T64000 Jobin Yvon, λ_{laser}= 532 nm, $\mathcal{P}_{laser}$=4.3 mW). The Raman shift spectrum is deconvoluted into three Gaussian peaks: two peaks at 520 cm^{-1} and 500 cm^{-1}, assigned to the crystalline fraction, and another one at 480 cm^{-1} related with the amorphous phase. χ_c is defined by the peak intensity relation $\chi_c=(I_{520}+I_{500})/(I_{520}+I_{500}+I_{480})$ and gives a semi-quantitative measure of the crystalline volume fraction, from χ_c=0 (fully amorphous material) to χ_c=1 (completely crystalline material) [86–89].

4.3.4 Results and discussion

Fig. 4.2 shows the computed thickness profile $d(\vec{x})$, obtained from the solution of Eq. 4.17 and assuming that $d(\vec{x}) \propto \vec{J}(\vec{x}) \cdot \hat{s}$, for the described filament net configuration (N=12, d_{f-f}=16 mm, L_{fil}=20 cm) and three different d_{f-s}=10 mm, 15 mm and 20 mm. The thickness profile $d(\vec{x})$ mappings of three μc-Si:H samples (χ_c ≈0.3-0.6), deposited for each different d_{f-s} are also shown in Fig. 4.2. The thickness profile predicted by the model matches with great accuracy with the experimental measurements (deviations are less than 1%). Regarding the deposited

a-Si:H films (χ_c=0), the experimental measurements of $d(\vec{x})$ for each tested d_{f-s} (15 mm and 20 mm) showed that the obtained thickness uniformity was, in both cases, very similar to that obtained for their corresponding μc-Si:H sample [35]. Hence, the assumptions made in the proposed model seem to be valid for either a-Si:H and μc-Si:H deposition.

Let us now discuss the results obtained for d_{f-s}=20 mm. This is the case, among the three different tested d_{f-s}, for which the measured thickness profile shows the lowest variations ($< 2.5\%$) over the central 10 cm $\times$ 10 cm area of the deposited film. This is in fact the area of interest that should be covered by the substrate because, outside this central area, the thickness uniformity is rapidly lost due to boundary effects. This results in a deposition frame of about 5 cm width that can be considered "lost". From additional simulation results, it was found that the optimal filament to substrate distance that guarantees the maximum homogeneity over the central area was d_{f-s}=18 mm. This optimal d_{f-s} also guarantees that the boundary layer effect affects the smallest possible portion of the deposition area, thus minimizing the width of the "lost" frame. Nevertheless, the expected homogeneity results for d_{f-s}=18 mm, do not substantially differ from those obtained for d_{f-s}=20 mm. The small differences at the central area of 10 cm $\times$ 10 cm between the experimentally measured thickness profile and the simulation are probably due to inhomogeneities of the substrate temperature and/or to differences in each individual filament temperature, which may have their origin in contact resistance variations. In the latter case, the scaling up to longer filaments, considering the minor contribution of the contact resistance, should improve the experimental homogeneity. Regarding the scalability towards larger deposition areas, additional simulations performed with the model show that for large area deposition (>1 m^2), as long as d_{f-f} and d_{f-s} are maintained, a further increment of the number of filaments N and/or their length L_{fil} does not have a significant influence, neither in the thickness uniformity achieved in the central deposition area (which is correspondingly scaled up) nor in the width of the "lost" frame. These results are consistent with the fact that our deposition system is working beyond the large area limit. As a final remark, it is worthwhile to mention that the deposition rates r_d of the deposited a-Si:H and μc-Si:H layers were, respectively, larger than 4.5 nm/s and 1 nm/s [90].

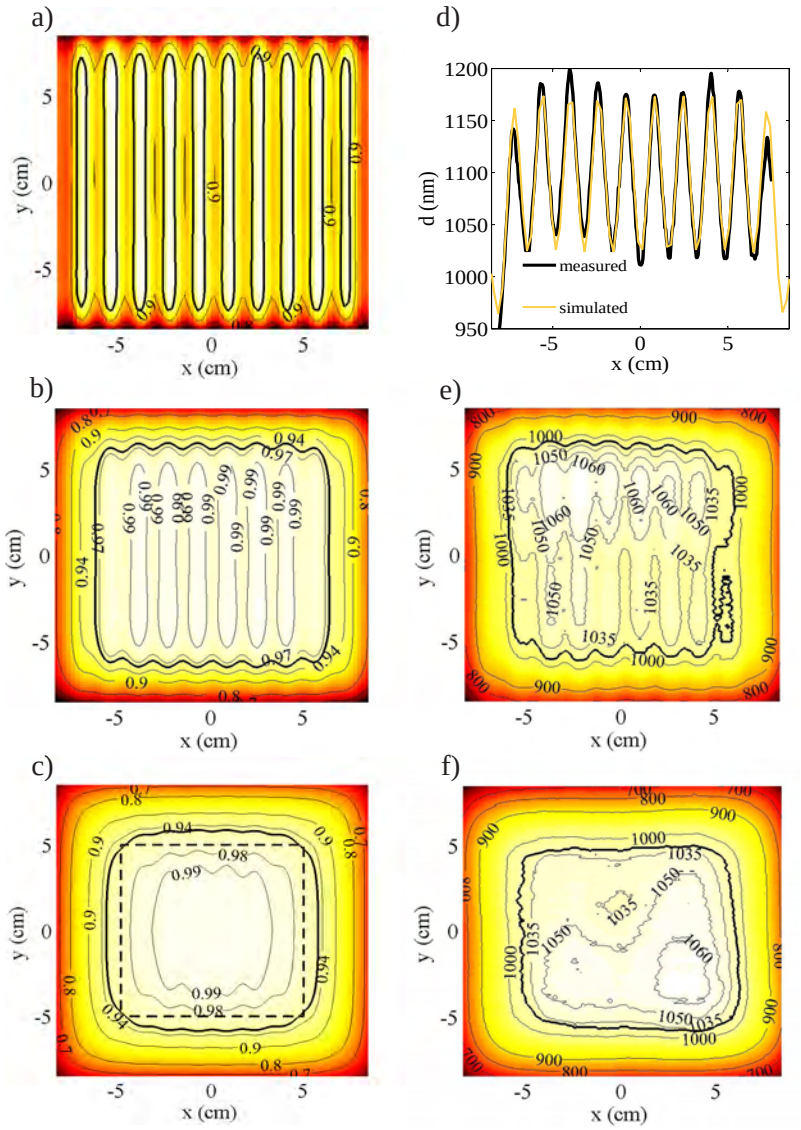

Figure 4.2: Left panel: Simulation results of the normalised thickness profile $d(\vec{x})$ for d_{f-s}=10 mm (a), d_{f-s}=15 mm (b) and d_{f-s}=20 mm (c). Right panel: Measured $d(\vec{x})$ mappings, in nm, of deposited μc-Si:H samples for d_{f-s}=15 mm (e) and d_{f-s}=20 mm (f). A linear profile is plotted for the case d_{f-s}=10 mm (d). All figures represent an area of 170 mm x 170 mm. The thick continuous lines delimit the area where thickness variations are lower than $\pm$2.5%.

4.3.5 Conclusions

We have shown the existence of a large area limit that allows studying, using a relatively small catalytic filament net (covering an area of 20 cm $\times$ 20 cm in our

case), the behaviour of any arbitrary larger HWCVD reactor. This large area limit only depends on geometrical factors like the filament to substrate distance d_{f-s} and the used filament net configuration (N, d_{f-f}, L_{fil}). It is important to notice that such a large area limit does not exist in PECVD reactors due to the plasma standing waves effect. If the filament net configuration and d_{f-s} are conveniently chosen, it can be achieved a very high thickness uniformity of the a-Si:H or μc-Si:H deposited films over an area of 10 cm × 10 cm. The thickness variations inside this area are lower than ±2.5%. Only a small frame of the deposition area is lost due to boundary effects. The experimental results of the thickness profile for a given filament net configuration can be predicted by the proposed diffusion model with great accuracy.

4.4 Scaling laws for the high rate deposition of μc-Si:H

The current interest in finding the way of depositing high quality μc-Si:H films at high r_d has already been stated several times in this thesis. In the introduction of this chapter, we have exposed that the strategy of increasing the deposition pressure p may be a good attempt to achieve this goal. This possibility has already been explored by S. Klein [27]. However, contrary to this study, Klein used the same filament to substrate distance for all depositions. Since increasing p entails a shift of the deposited material towards amorphous growth, lower silane concentrations were applied to grow μc-Si:H films at higher p. Therefore, the increase of the r_d derived from the increase of p was partly compensated by the usage of lower silane concentrations. Klein showed that r_d follows a power law like $r_d \propto p^{\alpha}$ with α <0.5 for those depositions resulting in μc-Si:H samples with similar crystallinity. This moderate increase in r_d and the fact that the μc-Si:H material obtained at high p was of very low quality made him discard this strategy. In this study, this strategy was taken up again considering the scaling law for r_d stated by Eq. 4.11 under the condition of keeping $\mathbb{k} = p \cdot d_{f-s}$ constant. Hence, an increase of p must be followed by a proportional decrease in d_{f-s}. However, keeping constant the parameter $\mathbb{k}$ in the set of Eqs. 4.8 does not guarantee that the material quality will be preserved. To preserve the material quality in the high r_d regime, the

species reaching the substrate and their relative concentrations should be maintained. Thus, an additional requirement must be fulfilled: The primary radicals generation terms, not included in Eqs. 4.8, should be increased in such a way that the relative concentrations of all the involved species do not change. The details concerning the gas-phase and surface chemical reactions involved in the growth of the film introduce are very complex. This makes it really difficult to build a fundamental model which successfully explains the growth mechanisms of μc-Si:H. The easiest way to deal with this problem is by using a phenomenological approach. In this section, we will present a phenomenological model that shows how the incoming flows of the precursor gases (Φ_{SiH_4} and Φ_{H_2}) and d_{f-s} must be scaled in order to preserve the μc-Si:H material quality at higher r_d. We will also show the results of a preliminary experimental study conceived for the validation of the scaling law for r_d (Eq. 4.11) under convenient deposition conditions derived from the proposed model.

4.4.1 A phenomenological approach to the growth mechanism of μc-Si:H

In the deposition process of μc-Si:H films with HWCVD, the reactor is supplied with a mixture of SiH_4 and H_2 as precursor gases. The SiH_4 and H_2 molecules are catalytically decomposed into primary radicals (Si and H) by the catalytic filaments according to the following reactions

$$SiH_4 \xrightarrow{\xi_{SiH_4}} Si + 4H \qquad \text{and} \qquad H_2 \xrightarrow{\xi_{H_2}} 2H \,, \tag{4.20}$$

where ξ_{SiH_4} and ξ_{H_2} are the dissociation probabilities of SiH_4 and H_2 respectively. The primary radical flows Φ_{Si} and Φ_H generated at the filaments surface are proportional to the residual partial pressures of silane, p_{SiH_4}, and hydrogen, p_{H_2} and read

$$\begin{aligned} \Phi_{Si} &= A_{cat} \mid \vec{J}_{Si} \mid = \beta_{SiH_4} \cdot p_{SiH_4} \\ \Phi_H &= A_{cat} \mid \vec{J}_H \mid = 4\beta_{SiH_4} \cdot p_{SiH_4} + 2\beta_{H_2} \cdot p_{H_2} \,, \end{aligned} \tag{4.21}$$

where $\vec{J}_{Si}$ and $\vec{J}_H$ are the corresponding radical fluxes, $A_{cat} = N2\pi r_0 L_{fil}$ is the total catalytic area of the filament net and

$$\beta_{SiH_4} = \xi_{SiH_4} \frac{A_{cat}\bar{\nu}_{SiH_4}}{4kT} \qquad \text{and} \qquad \beta_{H_2} = \xi_{H_2} \frac{A_{cat}\bar{\nu}_{H_2}}{4kT} \,, \tag{4.22}$$

are two proportionality coefficients which depend on the dissociation probabilities ξ_{SiH_4}, ξ_{H_2} and on the collision rate, $A_{cat}\bar{\nu}_i/4kT$, of the silane and hydrogen molecules with the filaments net. The parameters $\bar{\nu}_{SiH_4}$ and $\bar{\nu}_{H_2}$ refer, respectively, to the mean thermal velocities of the silane and hydrogen molecules, T is the gas mixture temperature and k is the Boltzmann's constant.

In order to keep invariable the reaction diffusion equations (4.8) that govern the deposition process, the fluxes of generated radicals $\vec{J}_{Si}$ and $\vec{J}_H$ must coherently scale with all the other fluxes of the rest of chemical species involved, *i.e.* according to Eq. 4.10. This means that the partial pressures p_{SiH_4} and p_{H_2} must individually scale as

$$\frac{p'_{SiH_4}}{p_{SiH_4}} = \frac{p'_{H_2}}{p_{H_2}} = \frac{d_{f-s}}{d'_{f-s}} \,. \tag{4.23}$$

Unfortunately, the partial pressures p_{SiH_4} and p_{H_2} are not simply given by $p_{SiH_4} = p{\cdot}\Phi_{SiH_4}/\Phi_{tot}$ (*idem* for p_{H_2}). The situation is more complicated since p_{SiH_4} and p_{H_2} will vary once the catalytic filaments are switched on. Fortunately, it is possible to relate p_{SiH_4} and p_{H_2} with the incoming flows Φ_{SiH_4} and Φ_{H_2} without having to solve the corresponding reaction-diffusion equations: Introducing the conductance of the pumping evacuation system for the two gases, C_{SiH_4} and C_{H_2} we can deduce the following relation between the incoming flows and the residual partial pressures (see Appendix F for details)

$$\begin{pmatrix} C_{H_2} \cdot p_{H_2} \\ C_{SiH_4} \cdot p_{SiH_4} \end{pmatrix} = \bar{\Psi} \cdot \begin{pmatrix} \Phi_{H_2} \\ \Phi_{SiH_4} \end{pmatrix} \,, \tag{4.24}$$

with

$$\bar{\Psi} = \frac{1}{1 - 2\alpha_{H_2} + \alpha_{SiH_4}} \begin{pmatrix} (1 + \alpha_{SiH_4}) & 2\alpha_{SiH_4} \\ -\alpha_{H_2} & (1 - \alpha_{H_2}) \end{pmatrix} , \tag{4.25}$$

and

$$\alpha_{SiH_4} = \frac{\beta_{SiH_4}(2\alpha_{Si} + 4\alpha_H)}{C_{SiH_4}} \qquad \text{and} \qquad \alpha_{H_2} = \frac{2\beta_{H_2}\alpha_H}{C_{H_2}} , \tag{4.26}$$

where α_{Si} and α_H are two dimensionless coefficients: α_{Si} expresses in a phenomenological manner the average number of Si atoms per silane molecule that are deposited as a consequence of the primary reaction Eq. 4.20 and secondary reactions like Eq. 4.2 wherein Si radicals participate. On the other hand, α_H does the same for the secondary reactions like 4.3 and the etching processes of hydrogenated silicon wherein H radicals participate. From Eq. 4.24 we see that, once the filaments are switched on, since $\alpha_{SiH_4} \neq 0$ and $\alpha_{H_2} \neq 0$, the concentration of silane decreases whereas the hydrogen concentration increases. If the conditions of Eq. 4.23 are satisfied, we have that $\alpha'_{Si} = \alpha_{Si}$ and $\alpha'_H = \alpha_H$. Probably, the easiest way to guarantee that the conditions of Eq. 4.23 are satisfied, is varying the incoming flows of silane and hydrogen as follows

$$\frac{\Phi'_{SiH_4}}{\Phi_{SiH_4}} = \frac{\Phi'_{H_2}}{\Phi_{H_2}} = \frac{d_{f-s}}{d'_{f-s}} , \tag{4.27}$$

maintaining the conductances C_{SiH_4} and C_{H_2} invariable. These are the conditions we have chosen to experimentally check the validity of the scaling law for r_d stated in Eq. 4.11.

4.4.2 Experimental Details

The filament net configuration chosen for the following experiments is the same as that described in section 4.3.3 (N=12, d_{f-f}=16 mm, L_{fil}=20 cm). Two deposition series were carried out using different filament to substrate distances (d_{f-s}=32 mm and d'_{f-s}=16 mm) which assure that the system is, in both cases, working beyond the large area limit. Four samples were deposited in each series. The same values

Table 4.1: Deposition conditions of the two series carried out for the experimental validation of the scaling law for r_d.

d_{f-s} [mm]	t [min]	Φ_{SiH_4} [sccm]	Φ_{H_2} [sccm]	SC [%]	p [Pa]
32	16	10.5	0	100	0.4
32	16	10.5	158.5	6.2	5.0
32	16	13.5	155	8.0	5.1
32	16	18	150.5	10.7	5.3
d'_{f-s} [mm]	t' [min]	Φ'_{SiH_4} [sccm]	Φ'_{H_2} [sccm]	SC' [%]	p' [Pa]
16	8	21	0	100	0.9
16	8	21	317	6.2	9.8
16	8	27	310	8.0	10.2
16	8	36	301	10.7	10.4

of silane concentration, $SC = \Phi_{SiH_4}/(\Phi_{SiH_4} + \Phi_{H_2})$, ranging from 100% to 6.2%, were used in both series ($SC = SC'$). A constant DC voltage (22 V) power source was used to heat the filaments by Joule effect. The filaments temperature was, for all the depositions, $T_{fil} \approx$1850°C. The base pressure was always lower than 10^{-4} Pa. The deposition conditions used in the two different series are summarized in Table 4.1. The Raman crystallinity factor of the samples has been evaluated following the same procedure explained in section 4.3.3.

For those samples with equal SC in both series, we can see in Table 4.1 that $\Phi'_{SiH_4} = 2\Phi_{SiH_4}$ and $\Phi'_{H_2} = 2\Phi_{H_2}$ according to the conditions of Eq. 4.27. Therefore, following Eq. 4.11, it is expected that the relation between the corresponding deposition rates will be $r'_d = 2r_d$. If the material quality is preserved, these samples should present a similar Raman crystallinity factor $\chi_c = \chi'_c$. It is known that the thickness of a μc-Si:H layer has a great influence on the promotion of the film crystallinity [91]. Hence, to make a proper comparison of χ_c between two different films, they must have a similar thickness. For this reason, the total deposition times t for the two series were chosen to be t=16 min and t'=$t/2$=8 min. The thickness of the deposited films was measured at the central point of the substrate using a mechanical stylus profiler (Veeco/Sloan, Dektak 3030).

After each deposition, the whole set of used filaments was replaced by a new one. Furthermore, the deposition chamber was cleaned after each deposition.

Thus, every deposition took place using a set of new filaments and a cleaned deposition chamber. Prior to every deposition, the new filaments were subject to a pre-deposition annealing treatment for 30 min in vacuum. In this way, it is assured that the stage of silicide (W_5Si_3) precipitation at the W filaments is not initiated during the film deposition process. In this way, it can be assured that measured deposition rates are not influenced by the degradation process of the filaments.

4.4.3 Results and discussion

The deposition rates r_d and r'_d, obtained from the two deposition series that were carried out, are plotted in Fig. 4.3 as a function of SC. In order to appreciate better the magnitude of the increase of the deposition rate, the ratio between r_d and r'_d has been plotted in Fig. 4.4.

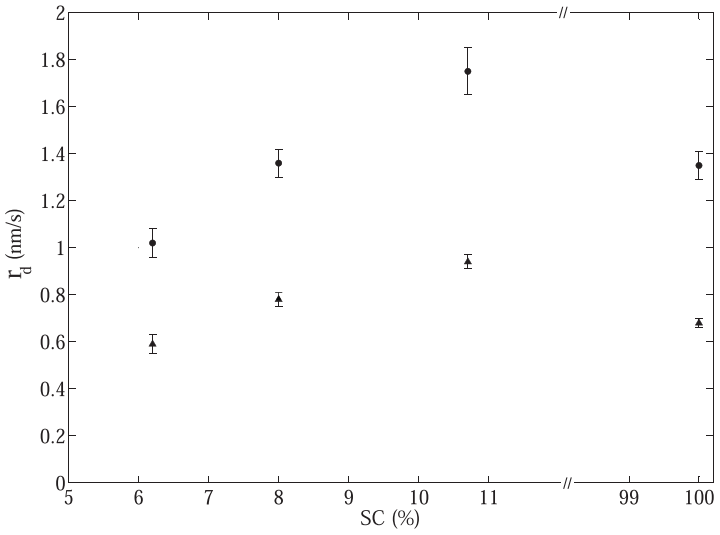

Figure 4.3: Deposition rate as a function of silane concentration, $r_d(SC)$ and $r'_d(SC)$, for two deposition series with d_{f-s}=32 mm (▲) and d'_{f-s}=16 mm (●)

According to the scaling law stated by Eq. 4.11, the ratio between the deposition rates obtained from both series should take a constant value $r'_d/r_d = 2$ independently of the silane concentration. The experimental results are very close

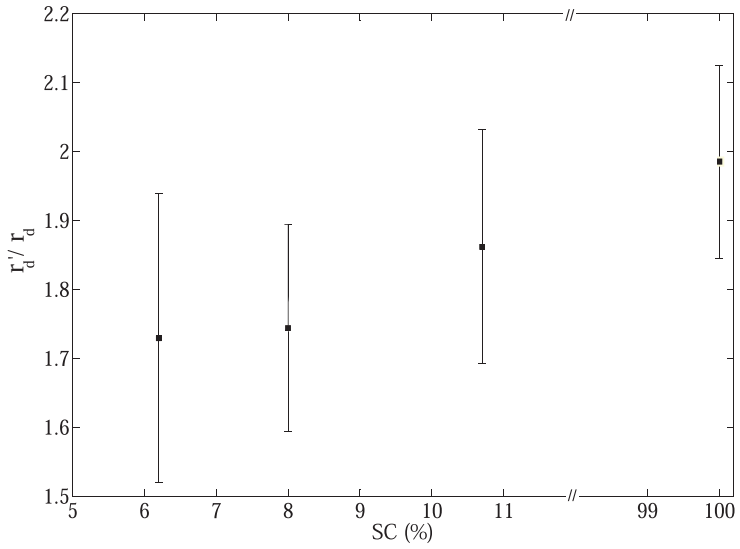

Figure 4.4: Ratio between r_d and r'_d as a function of silane concentration.

to this value. There are, however, slight deviations (<15%) from this theoretical value, specially in the case of low SC. On the other hand, when only pure silane is used as precursor gas (SC=100%), the experimental value of r'_d/r_d=2 matches very well with the prediction. If the same material is expected to be deposited when the system is scaled up towards higher r_d, the crystalline fraction of the samples deposited in both series, with the same value of SC, should be maintained. Fig. 4.5 shows the measured Raman crystallinity factors χ_c and χ'_c of the samples obtained from both deposition series as a function of SC.

The transition from a-Si:H to μc-Si:H is located at similar silane concentrations in the range $SC \approx$ 8.5-10.5 % for the two deposition series with d_{f-s}=32 mm and d'_{f-s}=16 mm. Of course, the material deposited without hydrogen dilution (SC=100%) is fully amorphous (χ_c=0) for both series. Even though the trends of $\chi_c(SC)$ and $\chi'_c(SC)$ are very similar, the corresponding μc-Si:H samples of both series, for the same SC, show different crystalline fractions.

According to these results, one could deduce that the dilution of SiH_4 with H_2 introduces slight deviations to the scaling law stated by Eq. 4.11. However, it is premature to stablish this conclusion. Up to now, we are not in conditions of affirming if the observed deviations are due to the difficulty of keeping constant $\alpha_{Si} = \alpha'_{Si}$, $\alpha_H = \alpha'_H$, $C_{SiH_4} = C'_{SiH_4}$ and $C_{H_2} = C'_{H_2}$ or if they constitute a real

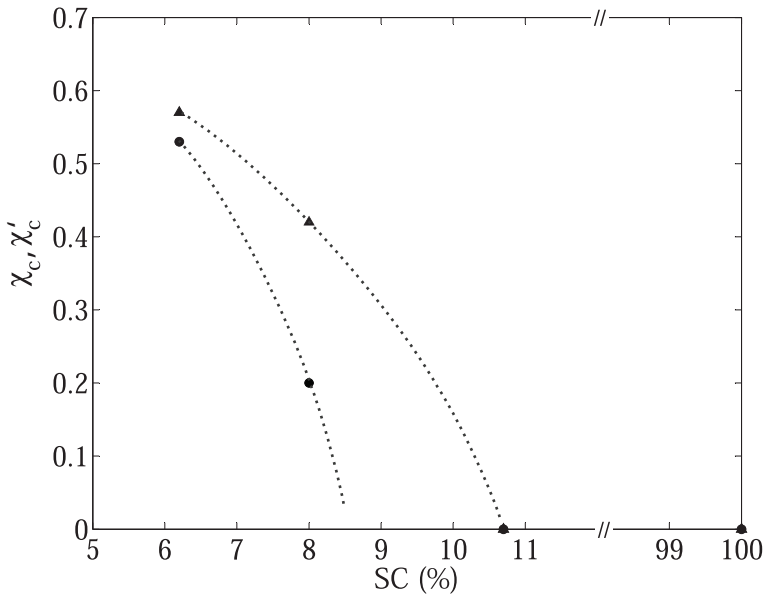

Figure 4.5: Raman crystallinity factor as a function of silane concentration for two deposition series with d_{f-s}=32 mm (▲) and d'_{f-s}=16 mm (●). The dashed lines are guides to the eye.

deviation from the scaling law for r_d exposed in this chapter.

4.4.4 Conclusions

We have exposed the possible existence of a scaling law which could allow the increase of r_d while preserving the quality of the deposited μc-Si:H layers. The scalability of the system towards higher r_d has been tested using two different filament to substrate distances and proportionally increasing the incoming flows of silane and hydrogen. We have shown the way to scale r_d, not only keeping $\mathbb{k} = p \cdot d_{f-s}$ constant but also proportionally scaling the silane and hydrogen partial pressures: $\frac{p'_{SiH_4}}{p_{SiH_4}} = \frac{p'_{H_2}}{p_{H_2}} = \frac{d_{f-s}}{d'_{f-s}}$. It has been shown that one possibility to satisfy this condition consists in varying the incoming silane and hydrogen flows as follows: $\frac{\Phi'_{SiH_4}}{\Phi_{SiH_4}} = \frac{\Phi'_{H_2}}{\Phi_{H_2}} = \frac{d_{f-s}}{d'_{f-s}}$ and maintaining the pumping conductances invariable. The obtained experimental results regarding the scaling of r_d are quite close to the expected ratio r'_d/r_d, showing an excellent agreement in the case of a-Si:H deposition using only pure SiH_4 as precursor gas. The obtained experimental

results are encouraging to explore more deeply the possibility of depositing high quality μc-Si:H material at high r_d >1 nm/s. A wider study, addressed to the confirmation of this possibility, is exposed in the following chapter.

Chapter 5

Microcrystalline Silicon Deposition at High Rate

5.1 Introduction

As it has been pointed out in Chapter 1, HWCVD is a promising alternative to the standard PECVD technique for the deposition of μc-Si:H as it has the potential to deposit μc-Si:H layers at high deposition rate (r_d) [30, 31, 90] and can be easily scaled up to large areas (>1 m^2) without any loss in the film homogeneity [33–35]. However, at present the standard r_d for high quality μc-Si:H layers in HWCVD is below 0.5 nm/s [27, 36, 37], still far from the requirements needed by the thin film solar cells industry (r_d >1 nm/s) for the economically profitable production of micromorph (a-Si:H/μc-Si:H) solar cells.

In this work, we used an appropriate hot wire configuration for depositing highly uniform (inhomogeneities lower than 2.5%) intrinsic μc-Si:H layers at high r_d ≈2 nm/s over an area of 10 cm × 10 cm. The filaments configuration has been designed following the strategy introduced in Chapter 4 to reach high r_d and homogeneity while being easily scalable to larger areas. The optimisation of the intrinsic μc-Si:H layer is usually carried out by integrating it as the active layer in a reference solar cell and then measuring the solar cell performance. Unfortunately, we were unable to follow this strategy because the lack of a load-lock chamber in our HWCVD reactor does not allow to deposit the stack of layers necessary to

obtain a solar cell due to the strong cross contamination induced by the filaments between the n- or the p-doped layer and the intrinsic active layer in the case of nip or pin cell structures respectively. Even though, it is possible to optimise the intrinsic μc-Si:H layer by means of an alternative indirect method: Recently, the Fourier Transform Infrared spectroscopy (FTIR) analysis has been proven as an efficient tool for the optimization of μc-Si:H layers grown with PECVD at r_d=2 nm/s [92]: The monitoring in time of the IR spectra of the samples permits to observe the progression of the post-deposition oxidation processes affecting them. This progression is evidenced by the increment with time of the 950-1200 cm^{-1} Si-O-Si stretching modes (SMs) and the less prominent 2250 cm^{-1} O_ySiH_x stretching mode (SM) contributions. In [92] Smets et al. demonstrated that the presence/absence of the narrow high stretching modes (NHSMs) located at 2083 cm^{-1} and 2103 cm^{-1}, related to the existence of hydrogen platelets on the crystalline grain boundaries surface, is correlated with the instability/stability of the material against post-deposition oxidation. This seems to indicate that the progressive oxidation of μc-Si:H samples is due to the replacement of the hydrogen located in the grain boundaries by oxygen. Hence, the suppression or the minimization of the NHSMs is an indicator of the material quality enhancement. Best μc-Si:H solar cell efficiencies are obtained when the intrinsic μc-Si:H active layers do not show any NHSMs contribution in their FTIR signature. Such μc-Si:H layers do not reveal any further post-deposition oxidation signal (SiO_x peak at 950-1200 cm^{-1}). Indeed, the μc-Si:H solar cells performance is deteriorated if the oxygen concentration exceeds certain critical values [93]. In particular, oxygen impurities cause an increase in the dark conductivity and charge density of the intrinsic μc-Si:H layers [94–96] leading to an undesired n-doping effect by introducing donor states [97]. Moreover, oxygen impurities cause structural changes in the μc-Si:H material which increase the defects density (creating additional dangling bonds or donor states) that can be detected by means of Electron Spin Resonance (ESR) measurements [97–99]. Oxygen impurities also shift the μc-Si:H deposition regime towards a more amorphous growth [96]. In order to reduce the oxygen concentration in the deposited μc-Si:H layers to an acceptable level ($1{\cdot}10^{19}$ cm^{-3} [93]) for depositing high quality material, a gas purifier (oxygen filter) has to be installed in the precursor gas supply lines.

We have used the strategy proposed by Smets et al. [92], based on the moni-

toring of the FTIR signature of the samples, for the optimization of the μc-Si:H material obtained with our HWCVD reactor. However, the study exposed in this chapter must be considered only as a preliminary optimisation process of the deposited μc-Si:H films because the material quality achievable with our current deposition system is seriously limited by the lack of a gas purifier in our precursor gas supply lines. Another limiting factor is that the gas lines of our precursor gas supply system are assembled using Swagelok fittings instead of the usual ultra-high vacuum VCR fittings. These limitations will be overcome with the installation in the clean room of the UB of a HWCVD prototype system with a load-lock chamber, oxygen filter and high quality gas supply systems.

We will show the results regarding the optoelectronic properties and stability against post-deposition oxidation of the optimised μc-Si:H layers deposited at $r_d \approx$2 nm/s. To achieve such high deposition rates we used a hot wire configuration with the minimal filament to substrate distance d_{f-s} needed to assure a high homogeneity of the film while working beyond the large area limit. In this way, according to the HWCVD scaling laws exposed in the previous chapter, the optimal deposition conditions should be found for higher values of pressure p than usual, thus leading to higher deposition rates. The pressure ($p \approx$3-5 Pa) and the filament to substrate distance (d_{f-s}=70 mm) used by Klein et. al. [27] to obtain high quality μc-Si:H at $r_d \approx$0.2 nm/s were used as a reference for the scaling of the $p \cdot d_{f-s}$ product in our hot wire configuration. In our experiments we fixed d_{f-s}=18 mm. We would then expect to obtain optimal μc-Si:H layers for pressures around p=10-20 Pa. Moreover, if high filament temperatures around 1850°C are used, the deposition rate can be further increased. We must then use thin filaments (0.175 mm diameter) to limit the radiated power onto the substrate and maintain the substrate temperature T_s reasonably low. This strategy may give the possibility to obtain high quality μc-Si:H layers at higher r_d. The optimised μc-Si:H layer shows excellent optoelectronic properties which have been measured by standard electrical measurement procedures. On the other hand, the optimised material shows a reasonable stability against post-deposition oxidation, though it still has to be further improved.

As a remark, the following study has been included as the final Chapter of this thesis with the purpose of giving a more comprehensive and straight-forward lecture to the reader. However, the work concerning the optimisation of the μc-Si:H

material is chronologically precedent to the studies exposed in the previous chapters. On one side, even if the ideas regarding the HWCVD scaling laws exposed in Chapter 4 had already been embraced, they where still far from being mature. In particular, we must notice that no attention was paid in proportionally increasing the silane and hydrogen flows used by Klein et. al. [27]. On the other side, the findings on the degradation of tungsten filaments described in Chapter 2 were still to be discovered. In particular, we can not assure that the catalytic performance of the used filaments was kept intact in all deposition runs, specially in the case of the last samples deposited using the same set of filaments. This latter fact may explain the scattering of the data obtained from the deposition rate, photosensitivity and Raman crystallinity measurements shown in section 5.3. Taking all this into consideration, the following study must be understood as a preliminary work for the optimisation of the μc-Si:H material deposited at high r_d.

5.2 Experimental details

The experiments have been carried out in our single chamber HWCVD reactor (see Appendix A). We used a filament net configuration which consists of 12 parallel W filaments of 20 cm length and separated a distance $d_{f\text{-}f}$=16 mm from each other. The filament to substrate distance was fixed to $d_{f\text{-}s}$=18 mm. As we have shown in the previous chapter, this hot wire configuration assures inhomogeneities of the film thickness lower than $\pm$2.5% over an area of 10 cm $\times$ 10 cm. The developed prototype implements simple cavity protection devices (see details in Chapter 3, section 3.3) to protect the cold ends of the filaments from silicidation. The prototype also implements tension adjustment mechanisms which maintain the geometry of the filaments in spite of the effects of thermal expansion. The radiated power onto the glass substrate (Corning 1737) was limited to approximately 0.84 W/cm^2 by using thin tungsten 0.175 mm diameter wires, heated up to a temperature T_{fil} $\approx$1850°C. The lowest stationary substrate temperature T_s was found to be about T_s=255°C measured by using a thermocouple in contact with the substrate. Such low T_s is reached without any kind of substrate cooling. Instead, the part of the heat radiation coming from the filaments that is transmitted through the substrate is avoided to be reflected back thus keeping T_s relatively low. Some samples were deposited at a higher T_s=340°C. In this case, a stainless steel back

plate was placed onto the substrate in order to reflect back the outcoming heat radiation. The optimization of the μc-Si:H material was done by depositing different series of material varying the silane concentration $SC = \Phi_{SiH_4}/\ (\Phi_{SiH_4}+\Phi_{H_2})$ from 5% to 14% with a total gas flow $\Phi_{tot}=\Phi_{SiH_4}+\Phi_{H_2}$=300 sccm. The deposition pressure p varied from 10 Pa to 20 Pa. A piece of single side polished crystalline silicon wafer was attached to the Corning 1737 glass substrate to perform FTIR spectroscopy measurements of the obtained samples. All the depositions have been carried out with a silane flow high enough to avoid working in the silane depletion regime (∼60% of SiH_4 utilisation). The base pressure was in all cases lower than 10^{-4} Pa. To reach such base pressure, the lack of a load lock chamber obliged us to degas the reactor chamber during several hours with a lamp heating system before each deposition run. The deposited films throughput was highly limited by this latter fact. In addition, the 12 used filaments had to be replaced once every 4 deposition runs thus making the optimisation process largely time consuming. It is also important to point out that the precursor gas supply system uses Swagelok fittings to seal the gas lines instead of the usual ultra-high vacuum compatible VCR fittings. No gas purifier is installed in the precursor gas lines.

The obtained samples were characterized by Raman spectroscopy (Micro Raman T64000 Jobin Yvon, λ_{laser}= 532 nm, $\mathcal{P}_{laser}$=4.3 mW). The crystallinity of the material close to the a-Si:H/μc-Si:H transition (defined as the point where the crystalline peak at 520 cm^{-1} disappears in the Raman spectra) was identified by evaluating the Raman crystallinity factor (χ_c) of the samples following the same procedure explained in Chapter 4, section 4.3.3. The stability against post-deposition oxidation of the samples was monitored by means of FTIR spectroscopy. The FTIR transmission measurements were carried out using a Bomen DA3 Fourier transform infrared spectrometer at 1 cm^{-1} wavelength resolution. The thickness of the samples was measured with a mechanical stylus profiler (Veeco/Sloan, Dektak 3030). The samples were electrically characterized by dark conductivity σ_d, activation energy E_a^σ and photo-conductivity σ_{ph} (∼1.5 AM illumination at 25°C) measurements. Aluminum coplanar contacts were deposited on the samples to carry out the measurements. These electrical measurements were performed in a vacuum chamber after annealing the samples with three increasing and decreasing temperature ramps between 30°C and 120°C during 4 hours.

5.3 Results

Fig.5.1 shows the effect of p and T_s on the Raman crystallinity factor of the deposited material. It can be seen that for a given silane concentration SC, χ_c decreases if p is increased or if T_s is decreased. Hence, the a-Si:H/μc-Si:H transition is shifted towards higher values of SC if p is increased or if T_s is decreased. Such trends of χ_c varying p and T_s are typically observed for μc-Si:H films deposited with either HWCVD [27] or PECVD [100, 101].

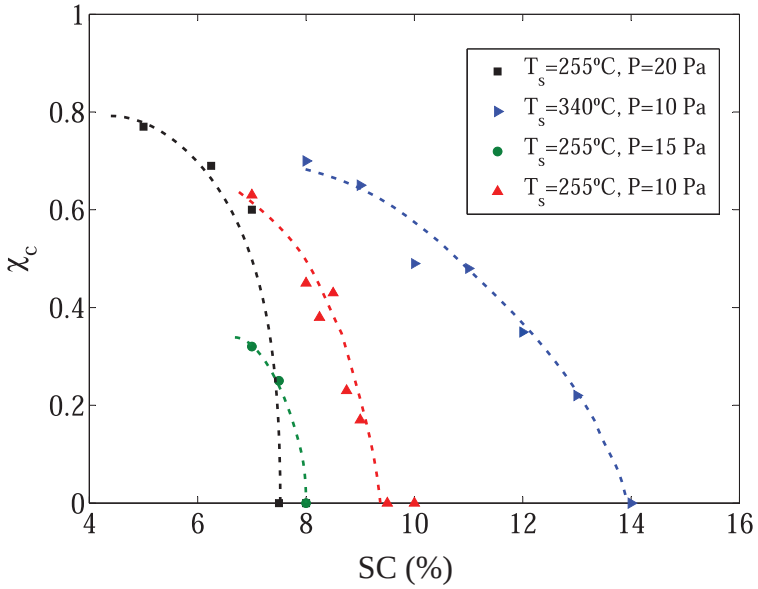

Figure 5.1: Raman crystallinity factor as a function of silane concentration for different substrate temperatures T_s and pressures p. Lines are guides to the eye.

The deposition rate r_d of the samples is plotted in Fig.5.2 as a function of χ_c. The figure shows that for a fixed χ_c, an increment of the substrate temperature T_s or the deposition pressure p generally leads to higher deposition rates. The deposition rates vary from 1.4 nm/s for highly crystalline samples up to 2.6 nm/s for purely amorphous material.

For those samples grown at T_s=255°C and p=10 Pa, the dark conductivity ranges from σ_d=10^{-10} S/cm for low crystalline samples ($\chi_c \approx$0) to σ_d=10^{-6} S/cm for highly crystalline samples ($\chi_c >$0.7) whereas the photo-conductivity shows little changes with χ_c and ranges from σ_{ph}=10^{-6} S/cm to σ_{ph}=10^{-5} S/cm. As a result,

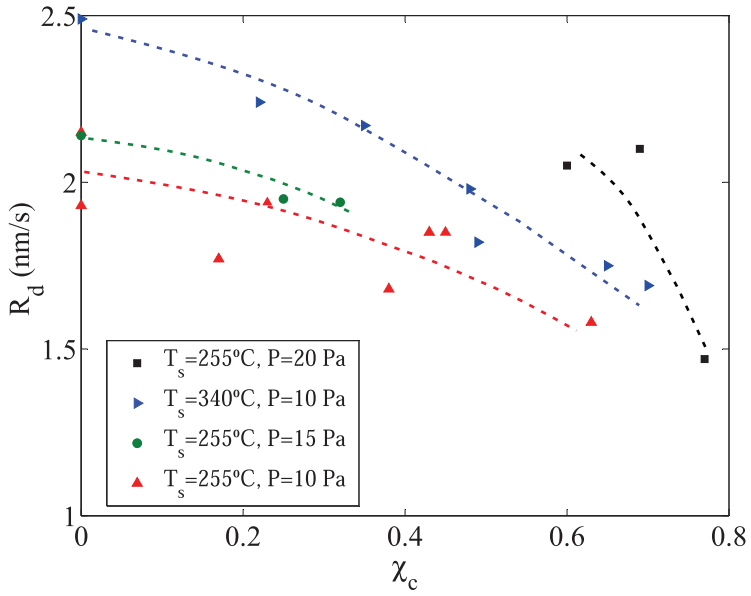

Figure 5.2: Deposition rate against the Raman crystallinity factor for different substrate temperatures T_s and pressures p. Lines are guides to the eye.

the photo-sensitivity S, defined as the ratio between σ_{ph} and σ_d, varies from nearly S=10^6 for χ_c ≈0 to S=10^2 for χ_c ≈0.7 (see Fig.5.3). These results are similar to those obtained for state of the art μc-Si:H samples grown at standard deposition rates [19,100]. Although S is not an appropriate parameter to be used as reference for material optimization, it is generally accepted that μc-Si:H films with χ_c ≈0.5 and a photo-sensitivity around S=10^3 are suitable for solar cell applications [19]. If T_s is increased from 255°C to 340°C, for χ_c >0, the obtained material exhibits higher σ_d and a lower σ_{ph}, resulting in a decrease in S of more than one order of magnitude. Such results indicate that this material grown at higher T_s has a much lower quality and its poor electric performance is probably linked to a higher defects density introduced by a large concentration of oxygen impurities.

Instead of using the photo-sensitivity as a reference parameter, the μc-Si:H material optimization has been performed following the FTIR hydride stretching modes (SMs) monitoring method proposed by Smets et al [92]. The monitoring in time of the IR spectra of the films permits to observe the progression of the post-deposition oxidation processes affecting the samples. This progression is evidenced by the increment in time of the 950-1200 cm^{-1} Si-O-Si SMs and the less prominent

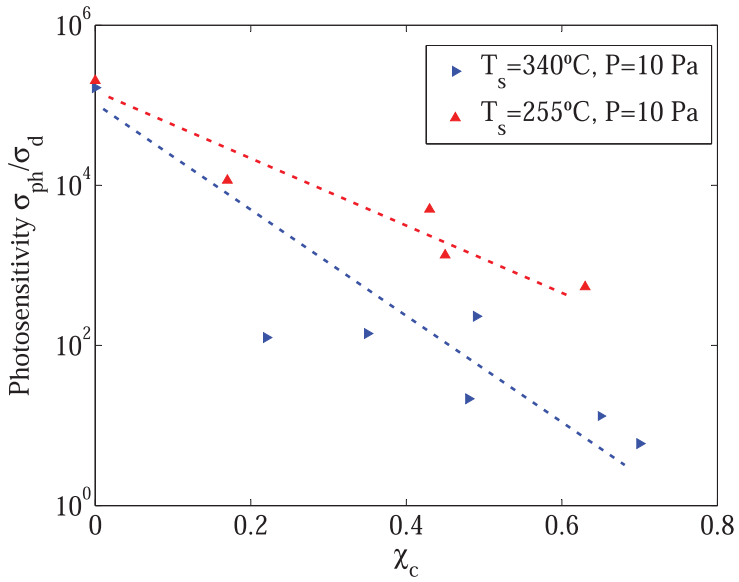

Figure 5.3: photo-sensitivity against the Raman crystallinity factor for different substrate temperatures T_s and pressures p. Lines are guides to the eye. Lines are guides to the eye.

2250 cm^{-1} O_ySiH_x SM contributions, which is related to the presence of the narrow high stretching modes (NHSMs) located at 2083 cm^{-1} and 2103 cm^{-1}.

Fig.5.4 shows the FTIR spectra of a μc-Si:H sample close to the a-Si:H/μc-Si:H transition (χ_c=0.25-0.60) for each of the four deposition series. FTIR measurements were carried out for each sample, as deposited and after 12 days of air exposure. The spectra depict the dihydride bending modes (=SiH_2) at 840-890 cm^{-1}, the 950-1200 cm^{-1} Si-O-Si SMs, the hydride Si–H_x SMs at 1850-2200 cm^{-1} and the O_ySiH_x SM at 2250 cm^{-1}. For all the samples, the contribution of the Si-O-Si SMs and O_ySiH_x SM is increasing with time. Validating the correlation reported by Smets et al. [92], it can be seen that the NHSMs at 2083 cm^{-1} and 2103 cm^{-1} were also present in all the spectra. However, it is clear that for the samples deposited at p=10 Pa and T_s=255°C, the post-deposition oxidation is considerably lower than for the others. Not only the increment of the Si-O-Si SMs and O_ySiHx SM is much more moderate, but also the contribution of the NHSMs is much lower.

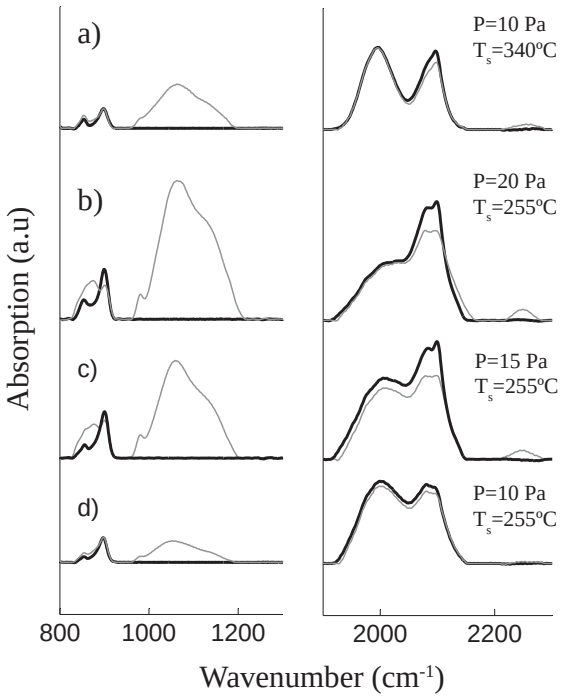

Figure 5.4: Depiction of the Si–O–Si SMs and the hydride SMs for μc-Si:H material close to the a-Si:H/μc-Si:H transition for the four different deposition series. The thicker lines correspond to as deposited material and the thinner ones to the same samples after 12 days of exposure to ambient air.

5.4 Discussion

According to [27], the good performance of μc-Si:H solar cells is restricted to a range of mid crystallinity (χ_c ≈0.3-0.6) of the active layers. Within such crystallinity range, the average r_d of the μc-Si:H layers shown in Fig.5.2 is about 2±0.3 nm/s for all the deposition series. This deposition rate is approximately an order of magnitude higher than those currently reached (≈0.2-0.5 nm/s) with industrial large area deposition PECVD equipment [5]. The measured photo-sensitivity reaches optimal values for solar cell applications (around 10^3) for those samples with intermediate crystallinity grown at p=10 Pa and T_s= 255°C. Even though it is not completely suppressed, the FTIR signature of the deposited samples shows a considerable reduction of their post-deposition oxidation signal. The FTIR hy-

Table 5.1: Crystallinity and optoelectronic properties of the current optimised μc-Si:H layer grown at 2 nm/s (2000 nm of layer thicknes).

	μc-Si:H (p=10 Pa, T_s=255°C)
χ_c	0.25
σ_d	$<2{\cdot}10^{-8}$ S/cm
σ_{ph}	$>1{\cdot}10^{-5}$ S/cm
S	$\approx 10^3$
E_a^σ	0.60 eV

dride and oxygen related SMs signals evolution of these samples is similar to that of μc-Si:H material obtained with PECVD in the HPD-VHF regime ($r_d \approx$2 nm/s) which, when integrated as the active layer in PIN solar cells, leads to intermediate 4.5% conversion efficiencies [92]. The characteristics of our current optimised μc-Si:H material for a layer thickness of 2000 nm are summarised in Table 5.1.

We must notice that, to be considered a high quality material, the optimal μc-Si:H active layer should present a slightly larger crystalline volume fraction and not show any signal of post-deposition oxidation while maintaining similar values of the optoelectronic properties σ_d, σ_{ph} and E_a^σ. Nevertheless, we should take into account that the presented results were obtained from a preliminary work for the material optimisation. In fact, these first results are quite encouraging, specially if we consider the limitations of our current deposition system: the precursor gas supply lines are sealed with Swagelok fittings and they do not have any gas purifier installed. These two circumstances suppose serious limitations for the reduction of oxygen contamination of the deposited samples during their optimisation process. Moreover, the lack of a load-lock chamber in our HWCVD reactor does not only make the production of solar cells impossible but also seriously limits the layer deposition throughput, thus making the whole optimisation process largely time consuming. This means that the expected optimal deposition parameters range has only been roughly scanned. Regarding this, it is known that, in the case of using PECVD, the deposition parameters window that allows obtaining high quality μc-Si:H at high deposition rates becomes very narrow [91, 92]. Taking all this into account, we consider that the quality of our current optimised μc-Si:H material grown at high r_d can hardly be enhanced unless the aforementioned limitations are remedied. We hope that the installation in the clean room of the UB of a HWCVD

system with a load-lock chamber, oxygen filter and high quality gas supply systems will open the possibility of optimising further the μc-Si:H layers grown at $r_d \geq$2 nm/s and testing its performance directly in solar cell devices. Finally, we must also notice that a further refinement of the optimal deposition parameters range should be done considering a proper scaling of the silane and hydrogen flows as discussed in Chapter 4, following Eq. 4.27.

5.5 Conclusions

In this work, we have used the following filaments arrangement for the deposition of μc-Si:H material: 12 parallel filaments of 0.175 mm diameter, 20 cm length and separated a distance $d_{f\text{-}f}$=16 mm from each other. A short filament to substrate distance (d_{f-s}=18 mm) was fixed in order to be sure that the deposition system was working beyond the large area limit. The deposition of different series of μc-Si:H with intermediate Raman crystallinity factor ($\chi_c \approx$0.3-0.6) led to an average deposition rate of about 2$\pm$0.3 nm/s for a wide range of deposition conditions (p=10-20 Pa, T_s=255-340°C). These r_d values are very interesting given that the current standard deposition rates achieved with large area industrial PECVD deposition systems are much smaller 0.2-0.5 nm/s [5]. The material quality has been indirectly evaluated by monitoring the progression of the post-deposition oxidation processes affecting the samples by means of FTIR spectroscopy. The IR spectrum signature of the preliminary optimised μc-Si:H material shows that when such short d_{f-s}=18 mm are used (instead of the usual $d_{f-s} \approx$50-80 mm), the best μc-Si:H material is obtained for a working pressure $p \approx$10 Pa (instead of the usual $p \approx$1-5 Pa), resulting in samples with a considerably reduced post-deposition oxidation. This result supports our initial assumption that keeping constant the product $\Bbbk = p \cdot d_{f-s}$ is a condition that must be satisfied in order to preserve the quality of the deposited μc-Si:H material. At present, we know that keeping $\Bbbk$ constant is a necessary but, unfortunately, insufficient condition. Indeed, a further refinement of the deposition parameters, using a proper scaling of the silane and hydrogen flows, is needed to proof the existence of a parameter window for depositing thick stable μc-Si:H films at high deposition rate.

Chapter 6

Conclusions

Regarding the filaments degradation issue:

- In the silicidation process of tungsten filaments at high temperature ($T_{fil} \approx$ 1850°C), three different stages have been identified: The initial Si atoms dissolution in W stage; the W_5Si_3 precipitation stage wherein a W_5Si_3 outer corona is formed, and, finally, the WSi_2 precipitation stage wherein the previously formed W_5Si_3 outer corona is progressively transformed into WSi_2.

- We have also shown that when the initial Si atoms dissolution stage ends, the catalytic performance decay of the filaments is initiated, resulting in a decrease of the deposition rate of about 35%.

- If it is desired to control and keep the deposition conditions constant during a HWCVD process, the *effective filaments lifetime* is determined by the duration of the Si atoms dissolution stage (*i.e.* the time delay t_0).

- We have proposed an electric model that allows identifying which is the current stage of the silicidation process of a filament at real time by simply monitoring the slope of its electric resistance.

- A diffusion model for the evaluation of t_0 has also been exposed. The results show that in most practical situations, for filament diameters of several tens or hundreds of microns, t_0 is independent of the filament radius.

- According to the experimental results, the time delay t_0 is of the order of few hours. Hence, in order to guarantee large operating times without maintenance interruptions of an eventual industrial HWCVD reactor for depositing Si based materials, an automatic filament replacement system should be implemented.

Regarding the protection of the filaments cold ends against silicidation:

- The protection devices based on the utilisation of a "chemically inert" thermal contact body are seriously limited by the deposition of Si over the thermal contact. Given that, this strategy for the protection of the cold ends of the filaments was discarded.

- A self-cleaning cavity device has been developed to protect the filament cold ends. This new device slows down the silicidation at the cold ends to a rate even lower than that at the central region of the filament, thus virtually solving the problem of the filament cold ends degradation.

Regarding the automatic replacement of the used filaments:

- We have developed an automatic filament replacement mechanism that allows replacing a used portion of filament by another clean portion of filament, without breaking vacuum. The apparatus is conceived in a modular way, based on the usage of tension adjustment mechanism moduli which act independently over each filament.

- The utilisation of said tension adjustment mechanism makes it possible to replace the used portions of the different filaments in parallel, keeping them tense in all operating situations and using only one or, maximum, two motors.

- The system is easily scalable to large deposition areas as it can be arranged for any arbitrary number of filaments without increasing the number of motors involved.

- The results obtained from the validation tests prove that the developed filament replacement mechanism, in combination with the use of effective cold

end protection devices, such as the self cleaning cavity, guarantees the repeatability and stability of a HWCVD deposition process for silicon based materials.

Regarding the scalability of the HWCVD technique towards large area and the thickness uniformity of the deposited films:

- We have shown the existence of a large area limit that allows studying, using a relatively small catalytic filament net (covering an area of 20 cm × 20 cm in our case), the behaviour of any arbitrary larger HWCVD reactor.
- If the filament net configuration and d_{f-s} are conveniently chosen, a very high thickness uniformity of the a-Si:H or μc-Si:H deposited films can be achieved over an area of 10 cm × 10 cm. The thickness variations inside this area are lower than ±2.5%.
- The experimental results of the deposited films thickness profile can be predicted, with great accuracy, by using the proposed radicals diffusion model.

Regarding the scaling laws for the high rate deposition of μc-Si:H:

- We have exposed the possible existence of a scaling law which could allow the increase of r_d by proportionally increasing the deposition pressure but preserving the quality of the deposited μc-Si:H layers.
- We have shown the way to scale r_d, not only keeping $\Bbbk = p \cdot d_{f-s}$ constant but also scaling proportionally the silane and hydrogen partial pressures: $\frac{p'_{SiH_4}}{p_{SiH_4}} = \frac{p'_{H_2}}{p_{H_2}} = \frac{d_{f-s}}{d'_{f-s}}$.
- It has been shown that one possibility to satisfy this condition consists in varying the incoming silane and hydrogen flows as follows: $\frac{\Phi'_{SiH_4}}{\Phi_{SiH_4}} = \frac{\Phi'_{H_2}}{\Phi_{H_2}} = \frac{d_{f-s}}{d'_{f-s}}$ and maintaining the pumping conductances invariable.

Regarding the optimisation of μc-Si:H deposited at high r_d:

- The deposition of different series of μc-Si:H with intermediate Raman crystallinity factor ($\chi_c \approx$0.3-0.6) led to an average deposition rate of about 2$\pm$0.3 nm/s for a wide range of deposition conditions (p=10-20 Pa, T_s=255-340°C).

- The IR spectrum signature of the preliminary optimised μc-Si:H material shows that when a short filament to substrate distance is used (d_{f-s} was 18 mm instead of the usual $d_{f-s} \approx$50-80 mm), the best μc-Si:H material is obtained for a working pressure $p \approx$10 Pa (instead of the usual $p \approx$1-5 Pa), resulting in samples with a considerably reduced post-deposition oxidation.

- The obtained results support our initial assumption that keeping constant the product $\Bbbk = p \cdot d_{f-s}$ is a condition that must be satisfied in order to preserve the quality of the deposited μc-Si:H material.

- A further refinement of the deposition parameters, using a proper scaling of the silane and hydrogen flows, is needed to proof the existence of a parameter window for depositing thick stable μc-Si:H films at high deposition rate.

Appendix A

Description of our HWCVD deposition equipment

All filament silicidation tests and layer depositions carried out in the framework of this thesis were performed using our custom single chamber HWCVD reactor. The dimensions of the chamber are 40 cm $\times$ 40 cm $\times$ 40 cm, what gives a volume of 64 litres. The system is not equipped with a load lock chamber. This means that when a new substrate is loaded, the vacuum must be broken and the deposition chamber is exposed to ambient atmosphere. The precursor gases are fed into the deposition chamber through a gas inlet. The incoming precursor gas flows are controlled using mass flow regulators (1-100 sccm for SiH_4 and 2-300 sccm for H_2). The gas pressure inside the deposition chamber is measured with a capacitive and penning vacuum gauges. The residual gases are evacuated through a pumping system formed by a turbomolecular pump a roots pump and a rotatory vane pump. A dry compressing scroll pump is used to generate the rough vacuum in the deposition chamber. Fig. A.1 shows a picture of our HWCVD deposition system.

We must notice that the precursor gas supply system uses Swagelok fittings to seal the gas lines instead of the usual ultra-high vacuum compatible VCR fittings. No gas purifier is installed in the precursor gas lines. The ultimate achievable base pressure of the deposition chamber is around $1{\cdot}10^{-5}$ Pa. To reach such base pressure, the lack of a load lock chamber obliges us to degas the reactor chamber during several hours with a lamp heating (around 250 W) system. On the other hand, despite these inconveniences, the system offers a great versatility for being

Figure A.1: Photograph of the HWCVD deposition system used in the framework of this thesis.

used in many deposition purposes. The deposition chamber includes a large number of vacuum feed-throughs which allow: The electrical connections necessary to supply the filaments or the lamps heating system with electric power; the use of thermocouples for the temperature measurement of the substrate and/or any mechanical element present in the deposition chamber; and the utilisation of a water serpentine, if necessary, for the cooling of said mechanical elements. The deposition chamber also includes rotatory feed-throughs which allow transferring motion to any movable elements either manually or via a controlled motor.

Fig. A.2 shows different filaments arrangements used in our HWCVD reactor for carrying out some of the experiments described this thesis work. The arrangement shown in picture (a) corresponds to those filament silicidation tests carried out for the study exposed in Chapter 2, section 2.2. Picture (b) shows the arrangement that has been used to study the filaments silicidation process influence on the deposition rate (see Chapter 2, section 2.3, Fig. 2.19). The 12 filaments arrangement shown in picture (c) has been used to deposit a-Si:H and μc-Si:H layers, over a substrate area of 20 cm $\times$ 20 cm, for the thickness uniformity study exposed in Chapter 4, section 4.3. This same filaments arrangement has also been

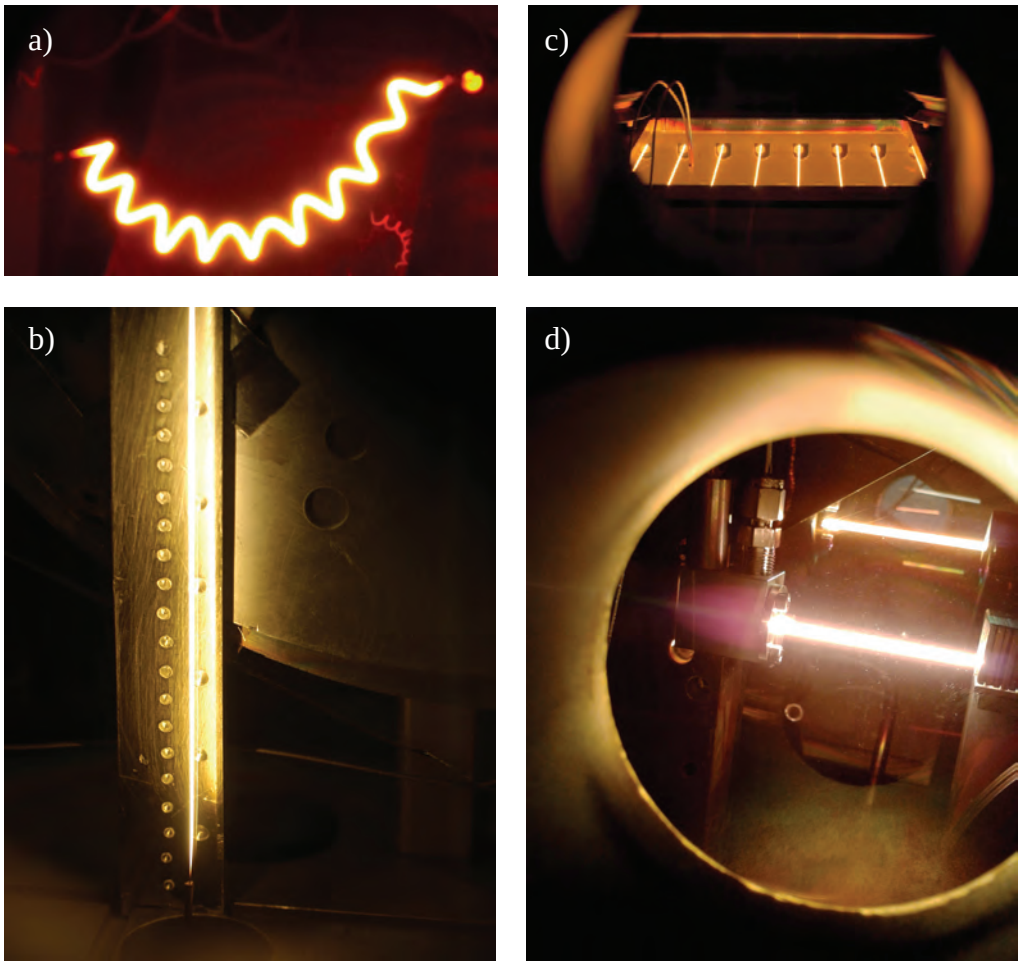

Figure A.2: Photograph of the HWCVD deposition system used in the framework of this thesis: a filament silicidation test (a), an experiment for the study of the filament silicidation process influence in r_d (b), filament arrangement (N=12) for the deposition of a-Si:H and/or μc-Si:H layers over a substrate area of 10 cm $\times$ 10 cm (c), experimental set-up for the validation of the automatic filament replacement mechanism using a self cleaning cavity protection device (d).

used for all the depositions carried out for the optimisation of μc-Si:H material grown at high r_d over a substrate area of 10 cm $\times$ 10 cm (see Chapter 5). Finally, picture (d) shows the filament arrangement used for the validation tests of the automatic filament replacement mechanism proposed in Chapter 3, section 3.5 implementing, at the same time, a self cleaning cavity protection device like that

proposed in Chapter 3, section 3.4.

Regardless which filament arrangement was used, the temperature, T_{fil}, of the catalytic filaments has been calculated in all cases from their electric resistance measurement. Once the filament length and radius are known, the calculation of the filament electric resistivity is straightforward if the applied electric voltage and current are measured. However, due to the presence of colder portions of filament close to the electric contacts, the filament length value used to evaluate T_{fil} must be shorter than the physical one. Taking the quadratic temperature dependence of tungsten electric resistivity [102], from the estimation of the filaments electric resistivity we can obtain an approximate value of T_{fil}.

In this work we have used tungsten filaments with different radii. To be sure to keep the same T_{fil} in all experiments, the electric current, I, applied to heat the filaments by Joule effect, was scaled using the following equation

$$\frac{I'}{I} = \left(\frac{r'_0}{r_0}\right)^{3/2} , \tag{A.1}$$

which can be directly deduced from the Stefan-Boltzmann law.

Appendix B

Si diffusion in a W filament

The exposed diffusion model stands for the initial stage of Si atoms dissolution in the W filament during a deposition process using silane as precursor gas. Let us call c_0 the concentration of Si atoms at the filament surface for which the chemical equilibrium would be reached if there was not any precipitation of silicides. If we consider the Si-W system to be an ideal solid solution, Raoult's law states that in the chemical equilibrium, the Si vapour pressure of the solution must equal the Si gas pressure of the environment $p_{Si} = \xi_{SiH_4} p_{SiH_4}$. Then,

$$\xi_{SiH_4} p_{SiH_4} = p^*_{Si} c_0 \,, \tag{B.1}$$

where p_{SiH_4} is the silane gas partial pressure (2 Pa in our experiments), ξ_{SiH_4} is the dissociation probability of silane molecules and p^*_{Si} is the vapour pressure of Si at $T = T_{fil}$. At temperatures in the range of T_{fil} ≈1850°C, p^*_{Si} ≈1 Pa [62] and ξ_{SiH_4} takes a value around 0.4 [64]. Introducing these values in Eq. B.1 one finds that, in any case, c_0 is much larger than the solubility limit of Si in W ($c_0 \gg c_{lim}$). Given that, the flux of Si atoms diffusing into the W filament, J^{in}_{Si}, can be considered to be practically constant:

$$J^{in}_{Si} \approx \alpha c_0 \,, \tag{B.2}$$

where α is a constant of proportionality. The diffusion equation of the problem

reads

$$\frac{\partial c(r,t)}{\partial t} - D\nabla^2 c(r,t) = 0\,, \tag{B.3}$$

where $c(r,t)$ is the Si concentration and D is the diffusion coefficient of Si in W. The solution of this equation applied to the case of a cylinder of radius r_0, under the boundary condition $J_{Si}^{in} \approx \alpha c_0$ and with the initial condition $c(r, t=0) = 0\ \forall r$, can be found in [65] (section 5.3.5) and takes the form

$$c(r,t) = \frac{\alpha c_0 r_0}{D}\left\{\frac{2Dt}{r_0^2} + \frac{r^2}{2r_0^2} - \frac{1}{4} - \sum_{n=1}^{\infty} exp\left(-D\beta_n^2 \frac{t}{r_0^2}\right)\cdot \frac{\mathcal{J}_0\left(\beta_n \frac{r}{r_0}\right)}{\beta_n^2 \mathcal{J}_0(\beta_n)}\right\}, \tag{B.4}$$

where $\mathcal{J}_0$ is the Bessel function of the first kind and β_n are the roots of $\mathcal{J}_1(r_0\beta_n)=0$. According to [58], the diffusion coefficient of Si in W is in the range of $D=10^{-11}$-10^{-12} cm^2/s. In most practical situations, we may then apply the limit $Dt \ll r_0^2$ which gives

$$\begin{aligned} c(r,t) = \frac{\alpha c_0}{D}\Bigg\{ & 2\left(\frac{Dr_0 t}{r}\right)^{1/2} ierfc\left(\frac{r_0 - r}{2\sqrt{Dt}}\right) + \\ & + \frac{Dt(r_0 + 3r)}{2r_0^{1/2} r^{3/2}} i^2 erfc\left(\frac{r_0 - r}{2\sqrt{Dt}}\right)\Bigg\}, \end{aligned} \tag{B.5}$$

where

$$\begin{aligned} ierfc(x) &= \frac{1}{\sqrt{\pi}} e^{-x^2} - x\, erfc(x) \\ i^2 erfc(x) &= \frac{1}{4}(erfc(x) - 2x\, ierfc(x))\,, \end{aligned}$$

and

$$\begin{aligned} erfc(x) &= 1 - erf(x) \\ erf(x) &= \frac{2}{\sqrt{\pi}} \int_0^x e^{-s^2} ds \,, \end{aligned}$$

where $erf(x)$ is the error function. For $r{=}r_0$, one obtains

$$c(r,t) = \frac{\alpha c_0}{D} \left\{ \frac{2}{\sqrt{\pi}} \sqrt{Dt} + \frac{Dt}{2r_0} \right\} . \tag{B.6}$$

We can now impose in Eq. B.6 that the Si concentration at the filament surface reaches the solubility limit c_{lim} at $t = t_0$, $c(r_0, t = t_0){=}c_{lim}$. Then, we get

$$\frac{Dt_0}{2r_0} + 2\sqrt{\frac{Dt_0}{\pi}} - \frac{c_{lim} D}{\alpha c_0} = 0 \,, \tag{B.7}$$

and with some algebra one finds

$$t_0 = \frac{2r_0^2}{\pi D} \left\{ \sqrt{1 + \frac{\lambda_1}{r_0}} - 1 \right\}^2 , \tag{B.8}$$

where

$$\lambda_1 = \pi D c_{lim} / \alpha c_0 \tag{B.9}$$

is a characteristic length scale of the problem. If we now apply the limit $r_0 \gg \lambda_1$ in Eq. B.8, we finally see that

$$t_0 = \frac{c_{lim}^2 D \pi}{\alpha^2 c_0^2} \,. \tag{B.10}$$

The limit $r_0 \gg \lambda_1$ holds in most practical situations. One can estimate the value of λ_1: Mixing Eqs. B.7 and B.9 one gets

$$\lambda_1 = \pi \left(\frac{Dt_0}{2r_0} + 2\sqrt{\frac{Dt_0}{\pi}} \right) , \tag{B.11}$$

and taking $D \approx 10^{-11}$ cm^2/s and the experimental values of $t_0 \approx$60 min with r_0=62.5 μm (this work) or $t_0 \approx$180 min [51] with r_0=250 μm (under different deposition conditions and probably using tungsten filaments from another provider than ours) one can estimate λ_1 to be in the range of few microns in both cases.

Appendix C

Electric model of a silicidated filament

According to the proposed electric model of a silicidated filament, three different zones can be distinguished. Let us discuss the case regarding the first two stages of the filament central portion silicidation process (Si atoms dissolution in W and W_5Si_3 precipitation). Then, the contribution of zone III to R_{fil} will be given by the parallel association of the remaining pure W filament core and the formed W_5Si_3 outer corona. We must notice that the fraction of W atoms reacted into W_5Si_3 is zero for $t < t_0$ ($FR_{W_5Si_3}(t < t_0) = 0$). Fig C.1 depicts schematically the three considered zones (I, II and III) for a silicidated filament.

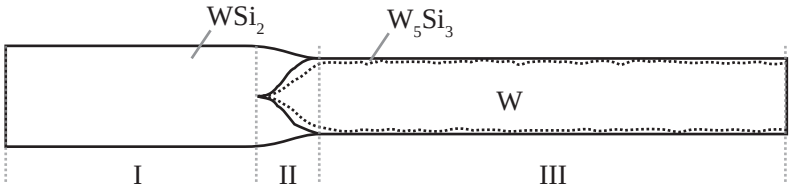

Figure C.1: Schematic view of the different resistances considered in a W filament during its degradation process at $t > t_0$.

The time dependence of the filament electric resistance $R_{fil}(t)$ is given by

$$R_{fil}(t) = 2C + 2R'_I vt + R'_{III}\left(L_{fil} - 2vt\right) , \tag{C.1}$$

where the first term $2C$ is a constant introduced by the contribution of the two transition zones II and the electric contact resistances, L_{fil} is the total filament length and v is the expansion velocity of the WSi_2 fronts. R'_I and R'_{III} are, respectively, the electric resistance per unit length of zone I and zone III. On one hand, R'_I reads

$$R'_I = \frac{\rho_{WSi_2}}{\pi r_{ext,I}^2}\,, \tag{C.2}$$

where ρ_{WSi_2} is the resistivity of the WSi_2 silicide phase and $r_{ext,I}$ is the external radius of a filament portion that is exclusively composed of WSi_2 (FR_{WSi_2}=1). On the other hand, R'_{III} is given by the parallel association of the remaining pure tungsten filament core and the outer corona formed by W_5Si_3. In this case, the fraction of W atoms that have reacted, $FR_{W_5Si_3}$, takes a value between 0 and 1. Then, R'_{III} reads

$$R'_{III} = \left(\frac{\pi (r_{int,III})^2}{\rho_W} + \frac{\pi ((r_{ext,III})^2 - (r_{int,III})^2)}{\rho_{W_5Si_3}} \right)^{-1}\,, \tag{C.3}$$

where $\rho_{W_5Si_3}$ and ρ_W are the resistivity of the W_5Si_3 silicide phase and of pure W respectively, $r_{ext,III}$ is the external radius of the portion of filament comprised in zone III and $r_{int,III}$ is the inner radius at which the W_5Si_3/W interface is located. Generally speaking, the external radius of a W filament which is gradually converted into WSi_x increases as a function of the fraction of W atoms that have reacted into WSi_x, FR_{WSi_x}, as follows

$$r_{ext} = r_0 \sqrt{(\gamma_{WSi_x} - 1) FR_{WSi_x} + 1}\,, \tag{C.4}$$

where r_0 is the initial radius of the tungsten filament and γ_{WSi_x} is the volumetric ratio between the WSi_x silicide phase and pure W which reads

$$\gamma_{WSi_x} = \frac{M_{WSi_x} \rho_W}{M_W \rho_{WSi_x}}\,, \tag{C.5}$$

where M_{WSi_x} and M_W are the molar mass of the WSi_x silicide phase and of pure tungsten respectively. To evaluate $\gamma_{W_5Si_3}$ a factor 1/5 must be introduced as 5 moles of initial pure W are needed to produce 1 mole of W_5Si_3. The volumetric ratio γ_{WSi_x} takes the following values for each silicide phase:

$$\begin{aligned} \gamma_{W_5Si_3} &= 1.72 \\ \gamma_{WSi_2} &= 2.70\,. \end{aligned}$$

Regarding zone III, the inner radius $r_{int,III}$ at which the W_5Si_3/W interface is located is given by

$$r_{int,III} = r_0\sqrt{1 - FR_{W_5Si_3}}\,. \tag{C.6}$$

Given that in our experiments the electric current I is fixed, the local dissipation of power only depends on the local status of the silicidation process. For any point x of the filament, we are able to evaluate the local temperature T by finding the solution of the equality between the local power (per unit length) dissipated by Joule effect and the local radiated power (per unit length):

$$I^2R'_x = e_x\sigma 2\pi r_{ext,x}T^4\,, \tag{C.7}$$

where R'_x is the local electric resistance per unit length, e_x is the local emissivity, $r_{ext,x}$ is the local external radius and σ is the Stefan-Boltzmann constant. For any point x wherein no silicides have yet precipitated, e_x is that of pure W, e_W. Otherwise, the local emissivity will be that of the corresponding precipitated silicide phase (e_{WSi_2} or $e_{W_5Si_3}$). One may now evaluate, for any point located in zone I or in zone III, the local temperature T as a function of FR_{WSi_x}. To do so, we must take into account that the emissivity and the resistivity of W, W_5Si_3 and WSi_2 are temperature dependant. The temperature dependences of e_W and ρ_W are taken from [103] and [102] respectively. The temperature dependence of e_{WSi_2} and $e_{W_5Si_3}$ in the range of T >1750°C are obtained by extrapolation of the data reported in [51] as values are only given for temperatures up to 1600°C and 1700°C respectively. Also, as there is only available data up to 1000°C and 1200°C

for ρ_{WSi_2} and $\rho_{W_5Si_3}$ respectively, the corresponding temperature dependences at higher temperatures were obtained by extrapolation of the data reported by Nava et al. [104] and Gelain et al. [105]:

$$\begin{aligned}
\rho_W(T) &= a_W + b_W T + c_W T^2 \\
\rho_{W_5Si_3}(T) &= a_{W_5Si_3} + b_{W_5Si_3} T \\
\rho_{WSi_2}(T) &= a_{WSi_2} + b_{WSi_2} T \\
e_W(T) &= a'_W + b'_W T + c'_W T^2 \\
e_{W_5Si_3}(T) &= a'_{W_5Si_3} + b'_{W_5Si_3} T \\
e_{WSi_2}(T) &= a'_{WSi_2} + b'_{WSi_2} T \, .
\end{aligned}$$

The values of the above coefficients, given in S.I. units ($[a_i] = \Omega$·m, $[b_i] = \Omega$·m/K, $[c_i] = \Omega$·m/K^2, $[a'_i]$= dimensionless, $[b'_i]$ =1/K and $[c'_i]$ =1/K^2), are: a_W=2.74·10^{-8}, b_W=2.61·10^{-10}, c_W=2.04·10^{-14}, $a_{W_5Si_3}$=102.63·10^{-8}, $b_{W_5Si_3}$=1.60·10^{-10}, a_{WSi_2}=-23.40·10^{-8}, b_{WSi_2}=1.15·10^{-10}, a'_W=-2.69·10^{-2}, b'_W=1.82·10^{-4}, c'_W=-2.19·10^{-8}, $a'_{W_5Si_3}$=-4.81·10^{-2}, $b'_{W_5Si_3}$=1.91·10^{-4}, a'_{WSi_2}=7.23·10^{-2} and b'_{WSi_2}=1.60·10^{-4}.

Once that the temperature of a filament portion has been calculated for a certain value of FR_{WSi_x} (see Fig. 2.14, the evaluation of R'_x is straightforward (see Fig 2.15). According to our calculations, R'_I takes a constant value R'_{WSi_2}=57± 3 Ω/m as zone I is considered a region wherein FR_{WSi_2}=1 is fixed. Regarding the portion of filament comprised in zone III, R'_{III} takes a constant value R'_W=52±3 Ω/m for $t < t_0$ as $FR_{W_5Si_3}(t < t_0)$=0. The values of R'_{WSi_2} and R'_W are obtained from the data points plotted in Fig. 2.15. We must now evaluate the time dependence of R'_{III} for $t > t_0$. As a first approximation, we will assume that R'_{III} follows a linear dependence with $FR_{W_5Si_3}$ (see red line in Fig. 2.15) like

$$R'_{III} = A_1 + B_1 \cdot FR_{W_5Si_3} \, , \tag{C.8}$$

and that, for $t > t_0$, the dependence of $FR_{W_5Si_3}$ with time is also linear

$$FR_{W_5Si_3}(t > t_0) = A_2 + B_2 \cdot t \, . \tag{C.9}$$

In consequence,

$$R'_{III(t>t_0)} = A + B \cdot t \,, \tag{C.10}$$

where A=A_1 + B_1A_2 and B=B_1B_2. From the linear fittings of the experimental data of $R'_{III}(FR_{W_5Si_3})$ and $FR_{W_5Si_3}(t > t_0)$ one obtains: A_1=45± 2 Ω/m, B_1=20± 1 Ω/m, A_2=0.025± 0.025, B_2=0.009± 0.002 min^{-1}, A=45±2 Ω/m and B=0.19±0.05 Ω/m·min. Since we know that the experimental value of v is (4.0±0.3) $\cdot 10^{-4}$ m/min, we may now evaluate the time derivative of $R_{fil}(t)$ for $t < t_0$ which reads

$$\frac{dR_{fil}}{dt}(t < t_0) = 2v(R'_{WSi_2} - R'_W) \,, \tag{C.11}$$

and takes a value $dR_{fil}/dt(t < t_0)$=0.005±0.005 Ω/min. Finally, the time derivative of $R_{fil}(t)$for $t < t_0$ reads

$$\frac{dR_{fil}}{dt}(t > t_0) = 2R'_{WSi_2}v - 2Av + BL_{fil} \,, \tag{C.12}$$

and takes a value $dR_{fil}/dt(t > t_0)$=0.065±0.020 Ω/min. Although the considered linear dependences may constitute a rough approximation, we consider that the errors committed are tolerable. In fact, the quadratic terms are only relevant for large times, that is to say for values of $FR_{W_5Si_3}$ pretty close to unity.

Appendix D

Temperature of the filament cold end

In a real situation, the filament needs two electrical contacts to be supplied with current. In these two points, the filament is also in thermal contact with the system. The electrical contacts usually are at a temperature T_0 much lower than T_{fil}. Hence, heat conduction losses in these regions must be taken into account. Fourier's law states that the heat flux $\vec{q}$ from the filament to the thermal contact is given by

$$\vec{q} = -k_w \vec{\nabla} T \,, \tag{D.1}$$

where k_w is the thermal conductivity of tungsten. In steady state conditions, the continuity equation states that for an infinitesimal unit length dx, the divergence of the energy flow equals the dissipated power (per unit length) by Joule effect, P_J, minus the irradiation power losses P_I

$$A_{fil} \vec{\nabla} \cdot \vec{q} = P_J - P_I \,, \tag{D.2}$$

which, for a one dimensional problem, can also be read as

$$A_{fil}(\mid q(x) - q(x - dx) \mid) = (P_J - P_I) dx \,, \tag{D.3}$$

where $A_{fil} = \pi r_0^2$ is the filament cross section area, being r_0 the filament radius. Then, it follows the diffusion equation

$$\frac{d^2T}{d^2x} = c_1\,T(x)^4 - c_2\,T(x)^2 - c_3\,T(x) - c_4\,, \tag{D.4}$$

with

$$\begin{aligned} c_1 &= 2\,e_w\sigma/(k_w\,r_0) \\ c_2 &= I^2\,a/(k_w\pi^2\,r_0^4) \\ c_3 &= I^2\,b/(k_w\pi^2\,r_0^4) \\ c_4 &= I^2\,c/(k_w\pi^2\,r_0^4)\,, \end{aligned}$$

where I is the electric current, e_w and k_w are, respectively, the emissivity and thermal conductivity of pure tungsten, r_0 is the tungsten filament radius and a, b and c are, respectively, the quadratic, linear and constant coefficients of the second order dependence of tungsten resistivity with temperature [102]. The above expressions for the coefficients c_1, c_2, c_3 and c_4 of Eq. D.4 are only valid for $x \geq L_c$. For $0 \leq x \leq L_c$, the filament is covered by the ceramic thin tube and these coefficients must be recalculated. The ceramic thin tube surrounding the filament has the undesirable effect of enlarging the radius of the radiating body ($r_{out} > r_0$) and also of increasing the thermal conductivity to $k_w r_0^2 + k_c(r_{out}^2 - r_{in}^2) > k_w r_0^2$. r_{in} and r_{out} are, respectively, the internal and the external radius of the ceramic thin tube, while k_c is the thermal conductivity of Al_2O_3. The coefficients c_1, c_2, c_3, and c_4 of Eq. D.4 for $0 \leq x \leq L_c$ are then given by

$$\begin{aligned} c_1 &= 2e_c\sigma r_{out}/\left[k_w r_0^2 + k_c(r_{out}^2 - r_{in}^2)\right] \\ c_2 &= I^2\,a/\left[k_w\,\pi^2\,r_0^4 + k_c\,\pi^2\,r_0^2(r_{out}^2 - r_{in}^2)\right] \\ c_3 &= I^2\,b/\left[k_w\,\pi^2\,r_0^4 + k_c\,\pi^2\,r_0^2(r_{out}^2 - r_{in}^2)\right] \\ c_4 &= I^2\,c/\left[k_w\,\pi^2\,r_0^4 + k_c\,\pi^2\,r_0^2(r_{out}^2 - r_{in}^2)\right]\,, \end{aligned}$$

where e_c is now the emissivity of Al_2O_3. Furthermore, regarding the temperature and heat flow functions, the following continuity conditions must be imposed at $x = L_c$

$$T(L_{c-}) = T(L_{c+}) \tag{D.5}$$

$$\left[k_w r_0^2 + k_c(r_{out}^2 - r_{in}^2)\right] \frac{dT(L_{c-})}{dx} = k_w r_0^2 \frac{dT(L_{c+})}{dx} \,. \tag{D.6}$$

Let us now consider the effect of enclosing the thin ceramic tube in a hollow body acting as a furnace. A percentage of the power radiated by the ceramic thin tube will be reflected back from the inner furnace walls and partially reabsorbed by the thin ceramic tube. Let us call P_J the local power (per unit length) dissipated by the tungsten filament and P_I and P_A the irradiated and the absorbed local power (per unit length) by the ceramic thin tube. Then, the necessary P_J to heat the ceramic thin tube at a particular temperature is

$$P_J = P_I - P_A \,. \tag{D.7}$$

The absorbed local power P_A is a function of P_I, i.e. $P_A(P_I)$. Being $\mathcal{R}$ the reflectance of the inner furnace walls, only a small part of the irradiated power that is reflected back equivalent to $e_c \mathcal{R} P_I$ is absorbed by the ceramic thin tube. The unabsorbed power, $(1-e_c)\mathcal{R} P_I$, bounces back towards the furnace inner walls and the process starts again. The total power absorbed by the ceramic thin tube is obtained by summing the contributions of all multiple reflections

$$\begin{aligned} P_A &= e_c \mathcal{R} P_I + e_c \mathcal{R}^2 (1 - e_c) P_I + e_c \mathcal{R}^3 (1 - e_c)^2 P_I \ldots \\ &= \sum_{i=1}^{\infty} e_c \mathcal{R}^i (1 - e_c)^{i-1} P_I \,. \end{aligned} \tag{D.8}$$

When the sum $P_I - P_A$ is evaluated, it comes out that $P_J = (1-\mathcal{R})/[1-\mathcal{R}(1-e_c)]P_I$. This corresponds to renormalising the ceramic thin tube emissivity as follows

$$e'_c = e_c \frac{(1-\mathcal{R})}{1-\mathcal{R}(1-e_c)} \,. \tag{D.9}$$

If the furnace is fabricated with the same material as the ceramic thin tube, then $\mathcal{R} = 1 - e_c$. The partial solutions of Eq. D.4, for $0 \leq x \leq L_c$ and $x \geq L_c$, have been numerically computed and glued at the point $x = L_c$. The results for different filament diameters and dimensions of the corresponding thin ceramic tube cover are plotted in Fig. 3.3.

Appendix E

Estimation of J_z using the images method

We consider a filament net composed of N identical, equidistant and parallel finite filaments (N=30 and $d_{f-s} = 1.25 d_{f-f}$). The general solution of the total radicals flux (see section 4.3.2), which reads

$$\vec{J}(\vec{x}) = \sum_{\vec{m} \in \mathcal{Z}^3} (-1)^{\vec{m} \cdot \vec{I}} \vec{J}_0 \left(\vec{x} + \vec{m} \cdot (\vec{a} + 2\lambda_4 \vec{I}) \vec{m} \right) , \tag{E.1}$$

has been solved using a finite set of images ($\vec{m} \in \{-Q, ..., Q\}^3$) and fixing λ_4=0 to obtain the value of $J_z(Q)$ as a function of Q. Q sets the limits of the set of integer numbers $\mathcal{Z}$ that determines the number of images considered in the calculations. Fig. E.1 shows how the solution of $J_z(Q)$ at the central point of the substrate, $\vec{x}_c$=(0,0,d_{f-s}), oscillates (continuous line in Fig. E.1) around the asymptotic value $lim_{Q \to \infty} J_z(Q)$.

The asymptotic value of $J_z(Q)$ can be estimated averaging the values of the two envelopes of $J_z(Q)$ (dashed lines). The deviations of these average values (open triangles in Fig. E.1) are less than 0.1%. Hence, the infinite summation of Eq. E.1 can be estimated using a relatively small finite number of images. It can be seen from Fig. E.1 that the asymptotic value of $J_z(Q)$ at the centre of the substrate is, with great accuracy, $lim_{Q \to \infty} J_z(Q) \approx \Gamma / 2 d_{f-f}$. This means that the radicals flux at the central point of the substrate practically behaves as if the considered

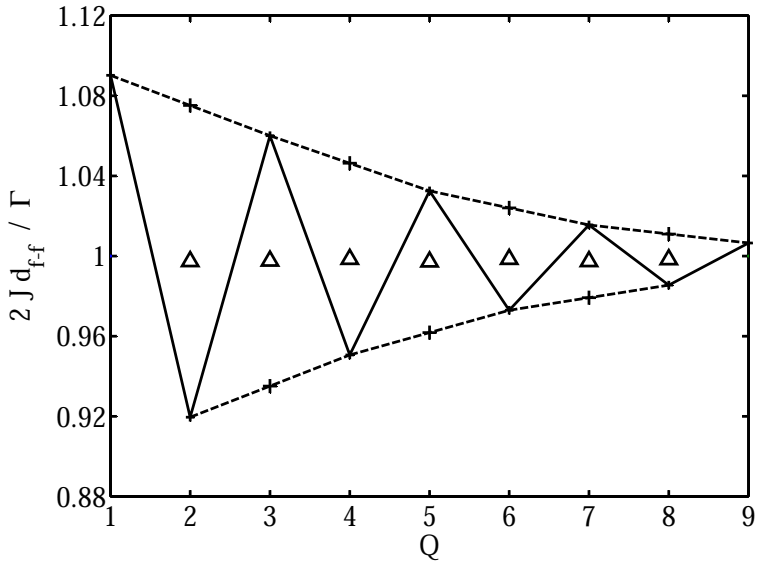

Figure E.1: Radicals flux $J_z(Q)$ as a function of Q, at the central point of the substrate, calculated from the solution of Eq. 4.17 for λ_4=0 and normalized to the infinite area limit $\Gamma/2d_{f-f}$. The considered filament net is formed by 30 filaments with $d_{f-s} = 1.25d_{f-f}$. The continuous line gives the oscillating solution of $J_z(Q)$. The dashed lines connecting the crosses show the two envelopes of $J_z(Q)$. Open triangles represent the average values of the two envelopes.

filament net was indeed infinite.

Appendix F

SiH_4 and H_2 partial pressures in μc-Si:H deposition

In the deposition process of μc-Si:H films with HWCVD, the reactor is supplied with a mixture of SiH_4 and H_2 as precursor gases. The SiH_4 and H_2 molecules are catalytically decomposed into primary radicals (Si and H) by the catalytic filaments according to the following reactions

$$SiH_4 \xrightarrow{\xi_{SiH_4}} Si + 4H \qquad \text{and} \qquad H_2 \xrightarrow{\xi_{H_2}} 2H\ , \tag{F.1}$$

where ξ_{SiH_4} and ξ_{H_2} are the dissociation probabilities of SiH_4 and H_2 respectively. The primary radical flows Φ_{SiH_4} and Φ_{H_2} generated at the filaments surface are proportional to the residual partial pressures p_{SiH_4} and p_{H_2} and read

$$\Phi_{Si} = A_{cat} \mid \vec{J}_{Si} \mid = \beta_{SiH_4} \cdot p_{SiH_4} \tag{F.2}$$

$$\Phi_{H} = A_{cat} \mid \vec{J}_{H} \mid = 4\beta_{SiH_4} \cdot p_{SiH_4} + 2\beta_{H_2} \cdot p_{H_2}\ , \tag{F.3}$$

where $\vec{J}_{Si}$ and $\vec{J}_{H}$ are the corresponding radical fluxes, $A_{cat} = N2\pi r_0 L_{fil}$ is the total catalytic area of the filament net and

$$\beta_{SiH_4} = \xi_{SiH_4} \frac{A_{cat}\bar{\nu}_{SiH_4}}{4kT} \qquad \text{and} \qquad \beta_{H_2} = \xi_{H_2} \frac{A_{cat}\bar{\nu}_{H_2}}{4kT} \,, \tag{F.4}$$

are two proportionality coefficients which depend on the dissociation probabilities ξ_{SiH_4}, ξ_{H_2} and on the collision rate, $A_{cat}\bar{\nu}/4kT$, of the silane and hydrogen molecules with the filaments net. The parameters $\bar{\nu}_{SiH_4}$ and $\bar{\nu}_{H_2}$ refer to the mean thermal velocities of the silane and hydrogen molecules, T is the gas mixture temperature and k is the Boltzmann's constant. We saw in section 4.2 that the most relevant secondary reaction for the growth of high quality a-Si:H [63] and epitaxial Si [71] is the reaction between Si and SiH_4, responsible for the generation of Si_2H_2 radicals (Eq. 4.2). It is presumable that Si_2H_2 radicals will also play an important role in the case of μc-Si:H deposition. Furthermore, given that large amounts of H radicals are generated during μc-Si:H deposition, the secondary reaction between H and SiH_4 (Eq. 4.3, which generates SiH_3 radicals, is expected to play an important role. On the other hand, hydrogenated silicon can be etched by the action of atomic hydrogen like, for instance, in the following reaction

$$H + Si - SiH_3 \longrightarrow SiH_4 + Si \,. \tag{F.5}$$

This kind of etching reactions may also have a considerable influence in the film growth. Even though the role of SiH_3 in the growth mechanism of μc-Si:H in HWCVD is not clear, its influence could be similar as that in the context of PECVD deposition [68, 106]. Let us now introduce two dimensionless coefficients: α_{Si} expresses in a phenomenological manner the average number of Si atoms per silane molecule that are deposited as a consequence of the primary reaction (Eq. 4.20) and the secondary reactions, like Eq. 4.2, wherein Si radicals participate. Likewise, α_H does the same for the secondary reactions, like Eq. 4.3, and the etching reactions, like Eq. F.5 wherein H radicals participate. We can now write the flow of Si atoms contributing to the growth of the film, Φ_{Si}^{dep}, in the following manner

$$\Phi_{Si}^{dep} = 2\alpha_{Si}\Phi_{Si} + \alpha_H\Phi_H \,, \tag{F.6}$$

where the coefficients α_{Si} and α_H depend on the geometry of the system, the substrate temperature T_s and the residual partial pressure p_{SiH_4}. However, if the system scales according to the set of Eqs. 4.8, they will only depend on the constant value of the product $p \cdot d_{f-s}$ and T_s, that is to say $\alpha_{Si}(\Bbbk, T_s)$ and $\alpha_H(\Bbbk, T_s)$. Since the quantity of hydrogen incorporated into the deposited film is negligible in comparison with the amount of H generated during the deposition process, it is a good approximation to consider that for each Si atom deposited, the equivalent of two hydrogen molecules are evacuated through the pumping system. Thus, the evacuated silane $\Phi^{out}_{SiH_4}$ and hydrogen $\Phi^{out}_{H_2}$ flows are related to the incoming flows Φ_{SiH_4} and Φ_{H_2} as follows

$$\Phi^{out}_{SiH_4} = \Phi_{SiH_4} - \Phi^{dep}_{Si} \tag{F.7}$$

$$\Phi^{out}_{H_2} = \Phi_{H_2} + 2 \cdot \Phi^{dep}_{Si} \, . \tag{F.8}$$

On the other hand, $\Phi^{out}_{SiH_4}$ and $\Phi^{out}_{H_2}$ can alternatively be written as

$$\Phi^{out}_{SiH_4} = C_{SiH_4} \cdot p_{SiH_4} \tag{F.9}$$

$$\Phi^{out}_{H_2} = C_{H_2} \cdot p_{H_2} \, , \tag{F.10}$$

where C_{SiH_4} and C_{H_2} are, respectively, the conductance of the pumping evacuation system for silane and hydrogen. The relation between the incoming flows and the residual partial pressures is deduced from the equalities between Eqs. F.7 and F.9. After some algebra, one finds

$$\begin{pmatrix} C_{H_2} \cdot p_{H_2} \\ C_{SiH_4} \cdot p_{SiH_4} \end{pmatrix} = \bar{\Psi} \cdot \begin{pmatrix} \Phi_{H_2} \\ \Phi_{SiH_4} \end{pmatrix} \, , \tag{F.11}$$

with

$$\bar{\Psi} = \frac{1}{1 - 2\alpha_{H_2} + \alpha_{SiH_4}} \begin{pmatrix} (1 + \alpha_{SiH_4}) 2\alpha_{SiH_4} \\ -\alpha_{H_2}(1 - \alpha_{H_2}) \end{pmatrix} , \tag{F.12}$$

and

$$\alpha_{SiH_4} = \frac{\beta_{SiH_4}(2\alpha_{Si} + 4\alpha_H)}{C_{SiH_4}} \qquad \text{and} \qquad \alpha_{H_2} = \frac{2\beta_{H_2}\alpha_H}{C_{H_2}} . \tag{F.13}$$

List of Figures

List of Tables

List of Symbols

Latin alphabet

A_{cat} ..... Catalytic area of the filament net

A_i ..... Area occupied by compound i

A_{fil} ..... Filament cross section area

$\vec{a}$ ..... Position vector of $\mathcal{S}$

C_i ..... Conductance for the chemical specie i (pumping system)

$a - Si : H$ ..... Amorphous hydrogenated silicon

c ..... Concentration of Si in the filament (solid solution)

c_0 ..... Concentration of Si at the filament surface in chemical equilibrium

c_{lim} ..... Solubility limit of Si in W

D ..... Diffusion coefficient

d ..... Thickness

d_{f-s} ..... Filament to substrate distance

d_{SiH_4} ..... Silane molecular diameter

E_a^i ..... Activation energy of reaction i

E_a^σ ..... Activation energy of electric conductivity

e_i ..... Emissivity of material i

e_c ..... Emissivity of the ceramic cover

FR_i ..... Fraction of W atoms reacted into compound i

I ..... Electric current

$\vec{I}$ ..... Identity vector

$\mathcal{J}_0$ ..... Bessel function of the first kind

$\vec{J}_i$ ..... Flux of chemical specie i

$\vec{J}(\vec{x})$ ..... Total flux of radicals at $\vec{x}$

$\vec{J}_z$ ..... Flux of radicals perpendicular to the substrate

k ..... Boltzmann constant

k_i ..... Thermal conductivity of compound i

k_c ..... Thermal conductivity of the ceramic cover

L_c ..... Ceramic cover length

L_{cav} ..... Cavity length

L_{fil} ..... Filament length

l_x, l_y, l_z ..... Dimensions of a parallelepiped domain $\boldsymbol{S}$

M_i ..... Molar mass of compound i

$\vec{m}$ ..... Images position vector (images method)

N ..... Number of filaments

$n(\vec{x})$ ..... Total concentration of radicals at $\vec{x}$

n_i ..... Concentration of chemical specie i (gas phase)

$\mathcal{P}_{laser}$ ..... Laser power

P_A ..... Absorbed power per unit length

P_I ..... Irradiated power per unit length

P_J ..... Power per unit length dissipated by Joule effect

p ..... Total deposition pressure

p_i ..... Partial pressure of chemical specie i

p_i^* ..... Vapour pressure of chemical specie i

Q ..... Limits of the set of integer numbers used in the images method

$\vec{q}$ ..... Heat flux

$\mathcal{R}$ ..... Reflectance

r_d ..... Deposition rate

R_{fil} ..... Filament electric resistance

R'_x ..... Electric resistance per unit length

r ..... Radial coordinate

r_0 ..... Filament radius (initial)

r_{cav} ..... Cavity inner radius

$r_{ext,I(II,III)}$ ..... External filament radius at zone I, II or III

$r_{int,III}$ ..... W/W_5Si_3 interface radius at zone III

r_{in} ..... Ceramic cover inner radius

r_{out} ..... Ceramic cover external radius

$\mathcal{S}$ ..... Domain of definition

S ..... Photosensitivity

SC ..... Silane concentration

T ..... Temperature

T_{fil} ..... Filament temperature

T_s ..... Substrate temperature

t ..... Accumulated deposition time

t_0 ..... Time delay

v ..... Silicide fronts propagation velocity

x, y, z ..... Cartesian coordinates

$\vec{x}$ ..... Position vector

$\mathcal{Z}$ ..... Set of integer numbers

Greek alphabet

$\alpha_{Si,H}$ ..... Phenomenological coefficients of Si deposition

β_n ..... Roots of $\mathcal{J}_0$

η ..... Energy conversion efficiency

γ_i ..... Volumetric ratio between W and compound i

κ_{dis} ..... Dissociation rate of silane in the cavity axis

$\kappa_{j,l}$ ..... Rate of chemical reaction between species j and l

$\lambda_{1,2,3...}$ ..... Characteristic length scale

λ_f ..... Mean free path

λ_{laser} ..... Laser wavelength

$\mu c - Si : H$ ..... Microcrystalline hydrogenated silicon

$\bar{\nu}_i$ ..... Mean thermal speed of chemical specie i

ξ_{des} ..... Desorption probability of Si at the filaments surface

ξ_i ..... Catalytic dissociation probability of chemical specie i

ρ_i ..... Resistivity of compound i

ϱ ..... Radicals generation rate at the filament surface

σ ..... Stefan-Boltzmann constant

σ_d ..... Electric dark conductivity

σ_{ph} ..... Electric photo-conductivity

φ_s ..... Sticking coefficient of radicals

χ_c ..... Raman crystallinity factor

Γ ..... Radicals generation rate at the filament surface per unit length

Φ_i ..... Flow of chemical specie i

Other

$\mathbb{k}$ ..... Constant parameter in the scaling law for R_d

Note 1: Upper indices have been frequently used to specify the direction or kind of fluxes $\vec{J}_i$ and flows Φ_i.

List of Acronyms

EDX ..... Energy Dispersive X-ray spectroscopy

FTIR ..... Fourier Transform InfraRed spectroscopy

HWCVD ..... Hot Wire Chemical Vapour Deposition

NHSMs ..... Narrow High Stretching Modes

PECVD ..... Plasma Enhanced Chemical Vapour Deposition

SEM ..... Scanning Electron Microscopy

SM(s) ..... Stretching Mode(s)

Curriculum Vitae

Personal Data

Name:	**Oriol Nos Aguilà**
Date of Birth:	Oct. 16, 1979 (Barcelona, Catalunya)
Nationality:	Spain
Cell Phone:	(0034) 646 284 534
e-mail:	oriol.nos@gmail.com

Academic Background

2005	**Physics Degree**: University of Barcelona (UB).
2007	**Master's Degree in Physics Engineering** (UB): Development of $Cu/Al_2O_3/NiCr$ thin film resistors. In collaboration with JBC Industrias SA.
2008-2012	**Physics Ph.D.** (Solar Energy Group, UB): Fundamental studies and technological development of the Hot-Wire Chemical Vapour Deposition (HWCVD) technique. Catalytic filament degradation studies. Deposition of intrinsic and doped amorphous and microcrystalline silicon thin films: Optical, electrical and structural characterisation.
2010-2012	**Associate Professor** (UB): Basics on Electromagnetism and Optics, Laboratory of Electromagnetism, Fundamentals of Laboratory. Electrical, thermal, optical and magnetic properties of materials for engineers.

Professional Background

2005-2007	**Research Assistant at Fundació Bosch i Gimpera**: Thermal characterisation and optimisation of cartridges in soldering systems for JBC Industrias SA.
2007-2009	**Research Assistant at ALSTOM Ecotecnia (now ALSTOM Wind)**: Optimisation and large area scaling up of microcrystalline silicon thin films deposited with HWCVD.

Experimental Skills

- Vacuum Technology: Working experience with Ultra-High Vacuum thin film deposition equipment (PECVD, HWCVD, Thermal Evaporation PVD and RF Sputtering PVD) in Clean Room environment.
- Optical and Structural Characterisation: Raman, FTIR, UV/VIS/NIR Spectrophotometer, SEM, EDS, SIMS, AFM and PDS.
- Electrical Characterisation: Photo- and dark-conductivity, activation energies and Hall effect measurements (carrier density, mobility...), solar cells characterisation.

Computational Skills

- Programming: MATLAB, Basics on LabVIEW and ANSYS.
- Technical Engineering Design: SolidWorks.
- Other: LaTeX, Microsoft Office (Excel, Powerpoint...), Adobe Creative Suite (Illustrator, Photoshop).

Language Skills

- Catalan: Native language.
- Spanish: Native language.
- English: Fluent.
- Portuguese: Conversant.
- French: Basic.

References

- From the Solar Energy Group, UB:
  Dr. Joan Bertomeu, *Group Leader*. E-mail: jbertomeu@ub.edu
- From JBC Industrias SA and ALSTOM Wind:
  Dr. David Soler, *Project Manager*. E-mail: david.soler@power.alstom.com

List of Publications

Published

1 O. Nos, P. A. Frigeri and J. Bertomeu
Hot wire configuration for depositing device grade nano-crystalline silicon at high deposition rate,
Thin Solid Films 519 (14), 4531-4534 (2011).

2 F. Kail, J. Farjas, P. Roura, C. Secouard, O. Nos, J. Bertomeu and P. Roca i Cabarrocas
The configurational energy gap between amorphous and crystalline silicon,
Physica Status Solidi Rapid Research Letters 5 (10-11), 361-363 (2011).

3 F. Kail, J. Farjas, P. Roura, C. Secouard, O. Nos, J. Bertomeu, F. Alzina and P. Roca i Cabarrocas
Relaxation and derelaxation of pure and hydrogenated amorphous silicon during thermal annealing experiments,
Applied Physics Letters 97 (3), 031918 (2010).

4 A. Antony, P. Carreras, T. Keitzl, R. Roldán, O. Nos, P. A. Frigeri, J. M. Asensi and J. Bertomeu
Influence of RF power on the properties of sputtered ZnO:Al thin films,
Physica Status Solidi A 207 (7), 1577-1580 (2010).

5 M. Colina, C. Molpeceres, M. Holgado, J. Gandia, O. Nos and J.L. Ocaña
Study of the refractive index change in a-Si:H thin films patterned by 532 nm laser radiation for photovoltaic applications,
Thin Solid Films 518 (18), 5331-5339 (2010).

6 P.A. Frigeri, O. Nos, J.D. Calvo, P. Carreras, R. Roldan, A. Antony, J.M. Asensi and J. Bertomeu
Uniformity study of amorphous and microcrystalline silicon thin films deposited on 10 cm x 10 cm glass substrate using hot wire CVD technique,
Physica Status Solidi C 7 (3-4), 588-591 (2010).

7 P. Carreras, A. Antony, R. Roldán, O. Nos, P. A. Frigeri, J. M. Asensi, and J. Bertomeu
Transparent conducting thin films by co-sputtering of ZnO-ITO targets,
Physica Status Solidi C 7 (3-4), 953-956 (2010).

8 P.A. Frigeri, O. Nos, S. Bengoechea, C. Frevert, J.M. Asensi, and J. Bertomeu
Hot wire chemical vapor deposition: limits and opportunities of protecting the tungsten catalyzer from silicide with a cavity,
Thin Solid Films 517 (12), 3427-3430 (2009).

9 C. Molpeceres, S. Lauzurica, J.J. García-Ballesteros, M. Morales, G. Guadaño, J.L. Ocaña, S. Fernández, J.J. Gandía, F. Villar, O. Nos, J. Bertomeu
Selective ablation of photovoltaic materials with UV laser sources for monolithic interconnection of devices based on a-Si:H,
Materials Science and Engineering B 159 (60), 18-22 (2009).

10 P.A. Frigeri, O. Nos, S. Bengoechea, C. Frevert, M. Stella, A. Antony, J.M. Asensi, and J. Bertomeu
Photovoltaic grade microcrystalline milicon deposited on plastic substrate by hot wire CVD,
23rd European Photovoltaic Solar Energy Conference, Valencia 3AV.2.20, 2408-2410 (2008).

To be published/In preparation

1 O. Nos, P. A. Frigeri, and J. Bertomeu
Technological solution for the automatic replacement of the catalytic filaments in HWCVD,
To be published in Thin Solid Films (2012).

2 P. A. Frigeri, O. Nos, and J. Bertomeu
Degradation of thin tungsten filaments at high temperature in HWCVD: key points to handle the automatic replacement of the filaments,
To be published in Thin Solid Films (2012).

3 O. Nos, P. A. Frigeri, and J. Bertomeu
Monitoring of the silicidation process of thin tungsten filaments at high temperature in HWCVD,
In preparation.

4 P. A. Frigeri, O. Nos and J. Bertomeu
Scaling laws of microcrystalline silicon deposition in Hot Wire CVD,
In preparation.

Patent Applications

1 P.A. Frigeri, O. Nos, and J. Bertomeu
Aparato y método para depósito químico en fase vapor con hilo caliente,
(2011) ES Patent No. P201132101. Madrid. OEPM Office.

2 O. Nos, P.A. Frigeri and J. Bertomeu
Hot Wire Chemical Vapour Deposition Technology for Thin Film Photovoltaic Industry,
Finalist project in the technology assessment contest *Valortec* (2011 Edition), organized by ACC1Ó (Generalitat de Catalunya)

Agraïments

(Acknowledgements/Catalan)

Tot allò que val la pena a la vida és quelcom que succeeix o es desenvolupa en companyia. La realització d'aquest tesi doctoral no n'és cap excepció . És per tant, el moment de recordar la gent que em va ajudar a recórrer aquest camí. Recordo molt bé el dia que em va trucar la Carol López per a dir-me que seria una bona idea presentar-nos a una oferta de feina que havia publicat el departament de Física Aplicada i Òptica de la UB pocs dies abans. Val a dir que, en aquell moment, cap dels dos podia pensar que ens acabarien oferint treballar plegats. Tot i que més tard els nostres camins van divergir, aquesta tesi doctoral comença a escriure's arrel d'aquella trucada de la Carol.

De seguida que vaig arribar a la sala per a l'entrevista, em vaig sentir còmode. Davant meu seien els professors Jordi Andreu, Cèsar Ferrater i Joan Bertomeu. Ells em van donar la oportunitat de començar en el mon de la recerca, treballant en un petit projecte per a una empresa catalana. Va ser en David Soler, amb un tracte proper i amable, qui em va guiar en les meves primeres passes com a investigador. Aquesta feina em va servir per a realitzar el projecte de màster sota la direcció d'en Jordi Andreu. Dos anys més tard, vaig acceptar amb il· lusió el suggeriment d'en Jordi per a continuar treballant al departament, tot realitzant una tesi doctoral en el marc d'un nou projecte d'àmbit nacional. En David Soler, que treballava a la empresa coordinadora del projecte, em va brindar la oportunitat de signar un nou contracte. D'aquesta manera estava gairebé garantit un finançament estable durant prop de tres anys, la qual cosa em va permetre treballar sense neguit tot aquest temps. Val a dir que, durant tota la meva etapa com

a doctorand, en Joan Bertomeu ha fet tot el possible per a que jo podés gaudir d'una font d'ingressos de forma ininterrompuda. Tanmateix, sempre ha trobat la via per a que jo podés assistir als congressos i cursos als quals volia inscriure'm. Sé molt bé que no ha estat una tasca senzilla i li estic molt agraït per tot el que ha fet per mi. Una vegada ha arribat el moment d'escriure aquesta tesi, les correccions periòdiques d'en Joan i en Paolo Frigeri han estat sempre acurades i precises. En Paolo Frigeri va arribar al grup poc abans de que jo comencés la tesi doctoral. Ell ha estat la persona amb qui he treballat colze a colze durant els darrers cinc anys. En Paolo no ha estat només el meu director de tesi. Ha estat també mestre, company i amic. M'ha brindat les seves idees com si fossin meves, guiant-me tant en els aspectes teòrics com en les tasques de laboratori amb una dedicació absoluta. Poc a poc, m'ha donat la confiança que em mancava per a anar assolint cada vegada més quotes d' autonomia. Hem rigut i hem plorat. Ens hem enfadat i ens hem perdonat. Hem viscut fracassos i hem assaborit èxits plegats. Penso que hem après molt l'un de l'altre. Sumant-ho tot, no puc menys que dir que ha estat un privilegi i una sort tenir en Paolo al meu costat. Grazie mille per tutto!

Encara em falta gent. No em puc oblidar d'en Manel, en Xavi i en Sunyol del taller mecànic de la universitat. Ens han ajudat molt. En Manel em dirà: Bfff! Ja veus! és la nostra feina. Com que no vull treure-li la oportunitat de dir-ho, m'avanço. Moltes gràcies nois! També vull estendre la meva gratitud a tots aquells tècnics que m'han ajudat en la meva feina, especialment als membres de les unitats de caracterització SEM, RAMAN i FTIR del SCT i el Servei de Làmina Prima de Geologia.

Vull recordar també tota aquella gent que, encara que no hagi tingut un impacte directe sobre el desenvolupament de la tesi, sí que hi ha contribuït de forma indirecte. Em refereixo a tos aquells becaris, secretaris i professors del departament amb qui he mantingut debats, dissertacions i xerrades de passadís. Gent que no ha dubtat en donar-me consell o un cop de mà quan ho he necessitat. Molt important ha estat el "nucli dur" de becaris del departament amb qui he compartit tants bons moments a la hora del cafè o del dinar: Arnau, Carol, Eric, Jofre, Luigi, Marta, Paz...

D'altra banda, fora de l'àmbit acadèmic, tinc la sort de tenir al meu costat a moltes persones que m'ajuden a tirar endavant. En primer lloc, la meva família i especialment els meus pares, Jaume i Montserrat, que m'ho han donat tot sense esperar mai res a canvi, sovint privant-se d'allò que jo sí he pogut gaudir gràcies als seus sacrificis. Tinc també la gran sort de tenir un bon sac d' amics i amigues. Deixeu-me només esmentar aquelles persones que han (sobre)viscut amb mi sota el mateix sostre i que sento sempre tant a prop meu: Judith, Àlex, Sophie, Jordi, Aúrea, Carol, Alberto, Àngela....i en Gerard i l'Anabel, sempre atents i encantadors (gràcies per dissenyar la portada!). M'estic allargant massa i no vull córrer el risc de deixar-me cap nom. A més, vosaltres, els que falteu, ja sabeu qui sou (o sigui que si estàs llegint això no et facis el ofès perquè queda clar que hi estàs inclòs). Moltes gràcies a tots per ser-hi! Finalment, no sé com puc agrair a la Bárbara, amb qui he compartit el dia a dia durant els darrers set anys, la immensa font d'ajuda i suport que ha estat i és per a mi. Més important encara, ella m'ajuda una miqueta cada dia a ser, i voler ser, millor persona.

Moltes gràcies a tots!

Bibliography

[1] A. J. Waldau, Pv status report 2011, *Tech. rep.*, European Commission, DG Joint Research Centre (2011).

[2] A. J. Waldau, *International Journal of Photoenergy* **2012**, 1 (2012).

[3] H. Keppner, J. Meier, P. Torres, D. Fischer, A. Shah, *Applied Physics A: Materials Science and Processing* **69**, 169 (1999).

[4] M. A. Green, K. Emery, Y. Hishikawa, W. Warta, E. D. Dunlop, *Progress in Photovoltaics: Research and Applications* **20**, 606 (2012).

[5] D. Richard, *Photon International* **11**, 166 (2011).

[6] C. Niikura, M. Kondo, A. Matsuda, *Journal of Non-Crystalline Solids* **338-340**, 42 (2004).

[7] M. Kondo, *Solar Energy Materials and Solar Cells* **78**, 543 (2003).

[8] U. Kroll, *et al.*, *Solar Energy Materials and Solar Cells* **48**, 343 (1997).

[9] T. Matsui, A. Matsuda, M. Kondo, *Solar Energy Materials and Solar Cells* **90**, 3199 (2006).

[10] Y. Sobajima, S. Nakano, T. Toyama, H. Okamoto, *Japanese Journal of Applied Physics* **46**, L199 (2007).

[11] Y. Sobajima, *et al.*, *Solar Energy Materials and Solar Cells* **93**, 980 (2009).

[12] G. Parascandolo, G. Bugnon, A. Feltrin, C. Ballif, *Progress in Photovoltaics: Research and Applications* **18**, 257 (2010).

[13] M. A. Lieberman, J. P. Booth, P. Chabert, J. M. Rax, M. M. Turner, *Plasma Sources Science and Technology* **11**, 283 (2002).

[14] L. Sansonnens, *et al.*, *Plasma Sources Science and Technology* **6**, 170 (1997).

[15] B. Strahm, C. Hollenstein, A. A. Howling, *Progress in Photovoltaics: Research and Applications* **16**, 687 (2008).

[16] B. Rech, T. Repmann, S. Wieder, M. Ruske, U. Stephan, *Thin Solid Films* **502**, 300 (2006).

[17] L. Li, Y. Li, J. A. A. Selvan, A. E. Delahoy, R. A. Levy, *Journal of Non-Crystalline Solids* **347**, 106 (2004).

[18] B. Rech, *et al.*, *Thin Solid Films* **427**, 157 (2003).

[19] A. Shah, *et al.*, *Thin-Film Silicon Solar Cells* (EPFL press, Laussane, 2010).

[20] K. Kawamura, *et al.*, *Thin solid films* **506-507**, 22 (2006).

[21] H. Takatsuka, *et al.*, *21st European Photovoltaic Solar Energy Conference, Dresden* p. 1531 (2006).

[22] S. Osono, M. Kitazoe, H. Tsuboi, S. Asari, K. Saito, *Thin Solid Films* **501**, 61 (2006).

[23] A. V. Shah, *et al.*, *Solar Energy Materials and Solar Cells* **78**, 469 (2003).

[24] H.Matsumura, *Japanese Journal of Applied Physics* **25**, 949 (1986).

[25] B. Schroeder, *Thin Solid Films* **430**, 1 (2003).

[26] A. H. Mahan, *Solar Energy Materials and Solar Cells* **78**, 299 (2003).

[27] S. Klein, F. Finger, R. Carius, *Journal of Applied Physics* **98**, 024905 (2005).

[28] H. Matsumura, K. Ohdaira, *Thin Solid Films* **517**, 3420 (2009).

[29] R. E. I. Schropp, *Thin Solid Films* **517**, 3415 (2009).

[30] J. Cifre, *et al.*, *Applied Physics A: Materials Science and Processing* **59**, 645 (1994).

[31] R. E. I. Schropp, Y. Xu, E. Iwaniczko, G. A. Zaharias, A. H. Mahan, *Material Research Society Symposium Proceedings* **715**, p. A26 (3.1) (2002).

[32] S. K. Y. Mai and, *et al.*, *Journal of Non-Crystalline Solids* **352**, 1859 (2006).

[33] K. Ishibashi, *et al.*, *Thin Solid Films* **430**, 58 (2003).

[34] A. Ledermann, U. Weber, C. Mukherjee, B. Schroeder, *Thin Solid Films* **395**, 61 (2001).

[35] P. A. Frigeri, *et al.*, *Physica Status Solidi C* **7**, 588 (2010).

[36] H. Li, C. H. M. van der Werf, A. Borreman, J. K. Rath, R. E. I. Schropp, *Physica Status Solidi (RRL)* **2**, 157 (2008).

[37] H. Li, R. H. Franken, R. L. Stolk, *Journal of Non-Crystalline Solids* **354**, 2087 (2008).

[38] G. Ertl, *The Nobel Prizes 2007, Chemistry Nobel Lecture* (Nobel Foundation, Stockholm, 2008).

[39] H. L. Duan, S. F. Bent, *Thin Solid FIlms* **485**, 126 (2005).

[40] J. Doyle, R. Robertson, G. H. Lin, M. Z. He, A. Gallagher, *Journal of Applied Physics* **64**, 3215 (1988).

[41] K. Tonokura, K. Inoue, M. Koshi, *Journal of Non-Crystalline Solids* **299**, 25 (2002).

[42] R. Walsh, *Accounts of Chemical Research* **14**, 246 (1981).

[43] J. K. Holt, M. Swiatek, G. Goddwin, H. A. Atwater, *Journal of Applied Physics* **92**, 4803 (2002).

[44] A. H. Mahan, A. Mason, B. P. Nelson, A. Gallagher, *Materials Research Society Symposium Proceedings* **609**, A6.6 (2000).

[45] E. Iwanickzko, *et al.*, *Materials Research Society Symposium Proceedings* **762**, A7.8.1 (2003).

[46] C. H. M. van der Werf, *et al.*, *Thin Solid Films* **517**, 3431 (2009).

[47] N. Kniffler, A. Pflueger, D. Scheller, B. Schroeder, *Thin Solid Films* **517**, 3424 (2009).

[48] D. Hrunsky, M. Scheib, M. Mertz, B. Schroeder, *Thin Solid Films* **517**, 3370 (2009).

[49] D. Knoesen, C. Arendse, S. Halindintwali, T. Muller, *Thin Solid Films* **516**, 822 (2008).

[50] P. A. T. T. van Veenendaal, O. L. J. Gijzeman, J. K. Rath, R. E. I. Schropp, *Thin Solid Films* **395**, 194 (2001).

[51] K. Honda, K. Ohdaira, H. Matsumura, *Japanese Journal of Applied Physics* **47**, 3692 (2008).

[52] C. H. M. van der Werf, *et al.*, *Thin Solid Films* **430**, 46 (2003).

[53] J. K. Yoon, *et al.*, *Journal of Alloys and Compounds* **420**, 199 (2006).

[54] K. H. Lee, *et al.*, *Surface and Coatings Technology* **187**, 146 (2004).

[55] W. Pletschen, *et al.*, *Applied Surface Science* **38**, 259 (1989).

[56] P. J. Codella, F. Adar, Y. S. Liu, *Applied Physics Letters* **46**, 1076 (1985).

[57] O. Chaix-Pluchery, L. Abello, G. Lucazeau, B. Cheneviert, R. Madar, *Journal of Physics and Chemistry of Solids* **57**, 527 (1995).

[58] H. Jehn, G. Bar, E. Best, E. Koch, B. R. Gudrun, *Gmelin Handbook of Inorganic Chemistry*, vol. A 5b (Springer Berlin, 1993).

[59] S. V. N. Naidu, A. M. Sriramamurthy, P. R. Rao, *Journal of Alloy Phase Diagrams* **5**, 149 (1989).

[60] R. E. Reed-Hill, *Physical Metallurgy Principles* (PWS Publishing Company, Boston, 1994).

[61] J. D. Verhoeven, *Fundamentals of Physical Metallurgy* (John Wiley and Sons, 1975).

[62] T. Tomooka, Y. Shoji, T. Matsui, *Journal of the Mass Spectrometry Society of Japan* **47**, 49 (1999).

[63] W. Zheng, A. Gallagher, *Thin Solid Films* **516**, 929 (2008).

[64] N. Honda, A. Masuda, H. Matsumura, *Journal of Non-Crystalline Solids* **266-269**, 100 (2000).

[65] J. Crank, *The Mathematics of Diffusion* (Clarendon Press, Oxford, 1979).

[66] K. Uchida, A. Izumi, H. Matsumura, *Thin Solid Films* **395**, 75 (2001).

[67] H. Matsumura, *Thin Solid Films* **395**, 1 (2001).

[68] K. Ishibashi, *Thin Solid Films* **395**, 55 (2001).

[69] P. A. Frigeri, *et al.*, *Thin Solid Films* **517**, 3427 (2009).

[70] K. Honda, K. Ohdaira, H. Matsumura, *Thin Solid Films* **516**, 826 (2008).

[71] I. T. Martin, *et al.*, *Thin Solid Films* **519**, 4585 (2011).

[72] R. D. Present, *Kinetic Theory of Gases* (Mc Graw Hill, New York, 1958).

[73] L. Lees, *Journal of the Society for Industrial and Applied Mathematics* **13**, 278 (1965).

[74] S. Pantazis, D. Valougeorgis, *European Journal of Mechanics B/Fluids* **29**, 494 (2010).

[75] J. V. Sali, S. B. Patil, S. R. Jadkar, M. G. Takwale, *Thin Solid Films* **395**, 66 (2001).

[76] A. Izumi, H. Sato, S. Hashioka, M. Kudo, H. Matsumura, *Microelectronic Engineering* **51**, 495 (1998).

[77] H. Matsumura, H. Umemoto, A. Izumi, A. Masuda, *Thin Solid Films* **430**, 61 (2003).

[78] R. E. I. Schropp, *et al.*, *24th European Photovoltaic Solar Energy Conference, Hamburg* p. 2328 (2009).

[79] T. H. Kim, K. M. Lee, J. Hwang, W. S. Hong, *Current Applied Physics* **9**, e108 (2009).

[80] J. K. Rath, *et al.*, *Thin Solid Films* **430**, 67 (2003).

[81] S. Klein, F. Finger, R. Carius, J. Lossen, *Thin Solid Films* **501**, 43 (2005).

[82] E. C. Molenbroek, A. H. Mahan, E. J. Johnson, A. Gallagher, *Journal of Applied Physics* **79**, 7278 (1996).

[83] A. Gallagher, *Journal of Applied Physics* **60** (1986).

[84] A. Shah, *et al.*, *Classical Electrodynamics* (John Wiley and Sons, 1962).

[85] R. Swanepoel, *Journal of Physics E* **16**, 1259 (1983).

[86] E. Bustarret, E. Hachicha, M. A. Brunel, *Applied Physics Letters* **52**, 1675 (1998).

[87] L. Houben, *et al.*, *Philosophical Magazine A* **77**, 1447 (1998).

[88] C. Smit, *et al.*, *Journal of Applied Physics* **94**, 3582 (2003).

[89] E. Vallat-Sauvain, *et al.*, *Journal of Non-Crystalline Solids* **352**, 1200 (2006).

[90] O. Nos, P. A. Frigeri, J. Bertomeu, *Thin Solid Films* **519**, 4531 (2011).

[91] R. W. Collins, *et al.*, *Solar Energy Materials and Solar Cells* **78**, 143 (2003).

[92] A. H. M. Smets, T. Matsui, M. Kondo, *Journal of Applied Physics* **104**, 034508 (2008).

[93] T. Kilper, W. Beyer, G. Bräuer, T. Bronger, R. Carius, *Journal of Applied Physics* **105**, 074509 (2009).

[94] P. Torres, *et al.*, *Applied Physics Letters* **69**, 1373 (1996).

[95] S. Veprek, *et al.*, *Journal of Physics C* **16**, 6241 (1983).

[96] T. Kamei, T. Wada, *Journal of Applied Physics* **96**, 2087 (2004).

[97] T. Kamei, M. Kondo, A. Matsuda, *Japanese Journal of Applied Physics* **37**, L265 (1998).

[98] F. Finger, J. Müller, C. Malten, R. Carius, H. Wagner, *Journal of Non-Crystalline Solids* **266-269**, 511 (2000).

[99] M. Vanecek, *et al.*, *Journal of Non-Crystalline Solids* **266-269**, 519 (2000).

[100] O. Vetterl, *et al.*, *Journal of Non-Crystalline Solids* **299-302**, 772 (2002).

[101] G. Bugnon, A. Feltrin, F. Meillaud, J. Bailat, C. Ballif, *Journal of Applied Physics* **105**, 064507 (2009).

[102] T. W. Zerda, *Stefan Boltzmann Law* (Texas Christian University, 2001).

[103] E. Lassner, W. D. Schubert, *Tungsten* (Kluwer Academic. Plenum Publishers, New York, 1999).

[104] F. Nava, K. N. Tu, E. Mazzega, M. Michelini, G. Queirolo, *Journal of Applied Physics* **61**, 1085 (1987).

[105] C. Gelain, A. Cassuto, P. L. Goff, *Oxidation of Metals* **3**, 115 (1971).

[106] D. A. Doughty, J. R. Doyle, G. H. Lin, A. Gallagher, *Journal of Applied Physics* **67**, 6260 (1990).